FUNCTIONAL CHARACTERIZATION OF RNA EDITING AND ALTERNATIVE SPLICING IN THE CARBOXYL-TERMINUS OF CA$_V$1.3 CALCIUM CHANNEL

TAN BAO ZHEN

NATIONAL UNIVERSITY OF SINGAPORE

2011

FUNCTIONAL CHARACTERIZATION OF RNA EDITING AND ALTERNATIVE SPLICING IN THE CARBOXYL-TERMINUS OF CA$_V$1.3 CALCIUM CHANNEL

TAN BAO ZHEN

B. Sc. (Life Sci.) (Hons.), NUS

A THESIS SUBMITTED FOR THE DEGREE OF

DOCTOR OF PHILOSOPHY

NUS GRADUATE SCHOOL FOR INTEGRATIVE SCIENCES AND ENGINEERING

NATIONAL UNIVERSITY OF SINGAPORE

2011

ACKNOWLEDGMENTS

First and foremost, I would like to express my heartfelt gratitude to my supervisor, Assoc. Prof. Soong Tuck Wah, for overseeing my project and giving me his guidance as well as his expert advice. In the course of pursing my postgraduate degree, he has given me constant support and encouragement.

I would also like to thank all the members, past and present, of the Ion Channel and Transporter Laboratory for their support, encouragement and friendship. Of special mention are Ms Yu Dejie and Dr Gregory Tan Ming Yeong, who provided advice and assistance with the electrophysiological recordings presented here.

I express my sincere thanks to my examiners for making time and effort to examine this thesis.

I thank the following people for the invaluable gifts of molecular clones, knockout tissues and cDNA: Dr. Diane Lipscombe (Brown University, RI, USA) for $Ca_V1.3$ $\alpha1$ clone. Dr. Terry P. Snutch (University of British Columbia, Canada) for β_{2a} and $\alpha_2\delta$ clones. Dr. Miyoko Higuchi (University of Heidelberg, Germany) for ADAR2$^{-/-}$ knockout cDNA and tissues.

Thanks also go out to our collaborators: Dr. David T. Yue (John Hopkins University School of Medicine, MD, USA) and Dr. Manfred Raida (ETC, Singapore) for their invaluable advice.

Last but not least, I would like to thanks my parents, Tan Boon Heng and Alice Chua Cheng Yong. Without their support and understanding, this thesis could never have been completed successfully.

TABLE OF CONTENTS

Chapter 1 – Introduction

Chapter 2 – Physiological characterization RNA editing in Ca$_V$1.3 IQ motif

Chapter 3 – Mechanism of CNS-specific RNA editing in Ca$_V$1.3 IQ motif

Chapter 4 – Splicing of carboxyl-terminus of Ca$_V$1.3 channel

Chapter 5 – Conclusion and Future Studies

LIST OF PUBLICATIONS

1. Bao Zhen Tan, Hua Huang, Runyi Lam and Tuck Wah Soong. Dynamic regulation of RNA editing of ion channels and receptors in the mammalian nervous system. **Molecular Brain** 2009, 2:13

2. *Hua Huang, *Bao Zhen Tan, Yiru Shen, Jin Tao, Fengli Jiang, Ying Ying Sung, Choon Keow Ng, Manfred Raida, Georg Kohr, Miyoko Higuchi, Haidi Fatemi-Shariatpanahi, David T Yue and Tuck Wah Soong. RNA editing of the IQ domain in $Ca_V1.3$ channels modulates their Ca^{2+}-dependent inactivation. (*in submission*). (*Co-first author)

3. Bao Zhen Tan, Fengli Jiang, Ming Yong Tan, Dejie Yu, Hua Huang, Yiru Shen, and Tuck Wah Soong, Alternative splicing in C-terminus of $Ca_V1.3$ channels modulates gating properties. (*in submission*).

ABSTRACTS

1. Bao Zhen Tan, Hua Huang and Tuck Wah Soong. Characterization of RNA editing of the IQ domain in $Ca_V1.3$ channels in mice brain. **Association for Neuron and Disease 2010, Bristol, U.K. (*Abstr.* 20)** (Awarded second place for poster presentation).

SUMMARY

$Ca_V1.3$ is a member of the L-type family of voltage-gated calcium channels (LTCC) and is predominantly expressed in the brain, cochlear hair cells, sinoatrial node (SAN), and pancreatic β-islets. Low-voltage activation of $Ca_V1.3$ channels controls excitability in sensory cells and central neurons, as well as pace-making in the SAN. Intramolecular protein interactions in the carboxyl-terminus of $Ca_V1.3$ proteins modulate calmodulin binding, altering calcium-dependent inactivation (CDI). Post-transcriptional modification of pre-mRNA, which includes alternative splicing and RNA editing, is vital for the correct translation of the genome and customization of proteins for optimal performance in individual cells.

The IQ motif of $Ca_V1.3$ channel is edited by Adenosine Deaminases Acting on RNA (ADAR), changing adenosine to inosine at three loci and DNA sequencing analysis showed that guanosine is observed only in the cDNA of $Ca_V1.3$. DNA sequencing analysis of cDNA from $ADAR2^{-/-}$ knockout mouse demonstrated that ADAR2 is crucial for RNA editing of $Ca_V1.3$. Protein analysis of the $Ca_V1.3$ proteins showed that the edited peptides are expressed in the wild-type mouse brain. Immunocytochemistry analysis demonstrated similar surface localization profiles between the edited and wild-type $Ca_V1.3$ proteins in primary hippocampal neurons. In addition, RNA editing of the IQ motif in $Ca_V1.3$ is central nervous system (CNS)-specific and developmentally regulated.

To identify the mechanisms responsible for the CNS-specificity and developmental regulation, neuronal and insulinoma cell lines were examined and found to express only unedited $Ca_V1.3$ channels. Experimental manipulations of culture conditions demonstrated that glucose metabolism, neuronal differentiation,

availability of cofactor zinc, and transient ADAR2 overexpression were insufficient for promoting editing in $Ca_V1.3$, despite elevated ADAR2 activity and its nuclear localization. Full-length analysis of ADAR2 showed higher percent of splice isoform with exon 5a, associated with higher ADAR2 catalytic activity, in the rat brain. Co-expression studies of synthetic construct gIQECS and ADAR2 showed significant editing at two adenosine loci, demonstrating that secondary pre-mRNA structure of $Ca_V1.3$ is critical for site-selective editing and *cis*-acting elements in the cell lines or outside CNS could prevent ADAR2-mediated editing.

Using transcript-scanning method, we identified eight different splice variants in the C-terminus of $Ca_V1.3$ expressed in rat brain. Electrophysiological characterization of the splice variants demonstrated modulations to activation, inactivation, and recovery properties. A novel C-terminal modulator (CTM) in $Ca_V1.3$ is responsible for diminished CDI in the long variant $Ca_V1.3_{42}$, and a key residual change in the distal C-terminus of rat and human $Ca_V1.3$ is critical for this reduction. Correction of this cloning error in our rat clone was sufficient for recapitulating the reported biophysical properties. Skipping of exon 41 removed the IQ motif, abolished CDI completely and decreased current density significantly. Removal of 91 nucleotides in $Ca_V1.3_{43i}$ caused a frame-shift and CTM-deletion, resulting in robust CDI of similar intensity as the short variant $Ca_V1.3_{42a}$, hyperpolarized shift in activation, and faster recovery from inactivation. Skipping of exon 44 and use of alternative acceptor site at exon 48 resulted in two splice variants that retained both CTM and type I PDZ-binding motif ITTL. However, shortening of the C-termini dampened CDI, caused hyperpolarized shifts in activation, and increased recovery from inactivation. Finally, removal of ITTL motif in exon 42a, Δ41 and exon 43i splice variants did not affect its soma-dendritic localization or synaptic targeting.

LIST OF TABLES

LIST OF FIGURES

ABBREVIATIONS

a.a	amino acids
ADAR	adenosine deaminase acting on RNA
BLAST	basic local alignment search tool
bp	base pairs (nucleotide)
CaM	calmodulin
CDI	calcium-dependent inactivation
cDNA	complementary deoxyribonucleic acid
C-terminus	carboxyl-terminus
CTM	carboxyl terminal modulator
DA	dopaminergic
DCRD	distal conserved regulatory domain
DHP	dihydropyridine
DMEM	Dulbecco’s Modified Eagle Medium
DNA	deoxyribonucleic acid
DRBM	double-stranded ribonucleic acid binding motif
dsRNA	double-stranded ribonucleic acid
E.coli	*Escherichia coli*
ECS	editing-site complementary sequence
EDTA	ethylenediamine tetraacetic acid
EGTA	ethyleneglycol tetraacetic acid
FBS	foetal bovine serum
FRET	fluorescence resonance energy transfer
GBM	glioblastoma
GFP	green fluorescence protein
HEK	human embryonic kidney cell line
HPLC	high performance liquid chromatography
HEPES	*N*-2-hyroxyethylpiperazine-*N*’2-ethanesulponic acid
I_{Ba}	Ba^{2+} current

I_{Ca}	Ca^{2+} current
IPPK	inositol 1,3,4,5,6-pentakisphosphate 2-kinase
IP_5	inositol pentakisphosphate
IP_6	inositol hexakisphosphate
I-V	current-voltage
IHCs	inner hair cells
kb	kilo base pairs (nucleotide)
LTCC	L-type voltage-gated calcium channel
MAP2	microtubule-associated protein 2
MRM	multiple reaction monitoring
mRNA	messenger ribonucleic acid
MS	mass spectrometry
nt	nucleotides
N-terminus	amino terminus
PCR	polymerase chain reaction
PCRD	proximal conserved regulatory domain
pCREB	cAMP response element binding protein
PDZ	Post-synaptic density protein 95, Drosophila disc large tumour suppressor and zonula occludens-1 protein
SAN	sinoatrial node
SCN	suprachiasmatic nucleus
SNc	substantia nigra pars compacta
SSI	steady-state inactivation
UTR	untranslated region
VDF	voltage-dependent facilitation
VDI	voltage-dependent inactivation
VGCC	voltage-gated calcium channel
WT	wild-type

Chapter 1

Introduction

1.1 Voltage-gated calcium channels

Calcium channels are key molecular assemblies of the plasma membrane, generating electrical and chemical signals essential for coordinating cellular functions. These voltage-gated calcium channels (VGCCs) are activated by plasma membrane depolarisation beyond their threshold potential in an excitable cell. Opening of the channel pore allows an influx of calcium ions into the cytosol that coordinates a plethora of responses, namely neurotransmitter release, secretion, excitation-contraction coupling, gene expression regulation and calcium homeostasis (Catterall, 2000). These channels are composed of a central pore-forming α_1 subunit, a cytosolic β subunit, and an extracellular α_2 subunit that is linked via a disulphide bond to the membrane-anchoring δ subunit. Functional diversity of calcium channels are derived primarily from the repertoire of α_1 subunit isoforms and its post-transcriptional modification, as well as modulated by the various auxiliary subunits.

1.1.1 The α_1 subunit

The pore-forming α_1 subunit is encoded by one of ten genes identified in the human genome. These ten channels are further categorized into three families based on their inactivation kinetics, pharmacological sensitivities and tissue distribution, as well as sequence homology – Ca_V1 (L-type channels that are activated by a range of voltages), Ca_V2 (P/Q-, N-, and R-type high-voltage-activated channels), and Ca_V3 (T-type low-voltage-activated channels). Each isoform is preferentially expressed in various tissues, and contributes to a broad spectrum of physiological functions (Catterall, 2000; Catterall et al., 2005). L-type Ca_V1 channels play a critical role in calcium influx in the soma and dendrites of numerous mammalian central neurons, regulating gene expression, cell survival, excitation-transcription coupling, synaptic plasticity, and active amplification of synaptic signals (Christie et al., 1997; Deisseroth et al., 1998; Weisskopf et al., 1999; Marshall et al., 2003; Wang et al., 2010).

The α_1 subunit protein is composed of four homologous domains (I-IV), each consisting of six transmembrane α-helices (S1-S6) and a membrane-associated loop between S5 and S6. The S4 segment of each homologous domain serves as the voltage sensor for activation. The S5 and S6 segments and the re-entrant S5-S6 loop form the pore lining, and a glutamate residue in each domain faces the narrow external pore. The carboxyl side chains of these amino acids coordinate a pair of calcium ions in the pore and function as the ion-selectivity filter. The inner pore is lined by the S6 segments and forms the receptor sites for pore-blocking L-type Ca^{2+} channels antagonist drugs (Hofmann et al., 1999).

1.1.2 The β and $\alpha_2\delta$ subunits

Auxiliary subunits of calcium channels modulate the trafficking and the biophysical properties of the α_1 subunit. The β subunit aids in the trafficking of α_1 subunit to the plasma membrane, partly by its ability to mask an endoplasmic reticulum retention signal in the α_1 subunit (Bichet et al., 2000), as well as modulates the biophysical properties of the channel with characteristics specific to α_1-β combination (Sokolov et al., 2000). The β subunit is encoded by four distinct genes (β_1- β_4), and numerous splice variants are known (Helton and Horne, 2002). While all four genes are expressed in the brain, each β subunit shows differential expression in other tissues (Arikkath and Campbell, 2003).

Diversity of $\alpha_2\delta$ subunits arises from four distinct genes ($\alpha_2\delta$-1 - $\alpha_2\delta$-4) as well as alternative splicing of these subunits, which are differentially expressed in various tissues. Extensive glycosylation of the α_2 subunit is important for maintaining the stability of the interaction with α_1 and is a major determinant of the protein's ability to stimulate the current amplitude (Gurnett et al., 1996). The co-expression of $\alpha_2\delta$-1 allows an enhancement in membrane trafficking of α_1 subunit, associated with an increase in the number of ligand binding sites, current amplitude, faster activation and inactivation kinetics and a hyperpolarizing shift in voltage dependency of activation (Felix et al., 1997).

1.2 Ca$_V$1.3 channels

The L-type Ca$_V$1.3 channels, which are expressed together with Ca$_V$1.2 channels in many tissues, was initially thought to be high-voltage-activated and slowly activating, with high sensitivity to dihydropyridines (DHP) (Ertel et al., 2000). Due to the high overlapping of biophysical and pharmacological properties with Ca$_V$1.2 channels and its low expression in heterologous system, Ca$_V$1.3 channels were not considered unique until the generation of Ca$_V$1.3 knockout mice (Platzer et al., 2000; Zhang et al., 2002; Mangoni et al., 2003). Absence of a low-threshold activating calcium current in the sinoatrial node (SAN) cells of Ca$_V$1.3$^{-/-}$ knockout mice caused significant SAN dysfunction, characterized by sinus bradycardia, and the same absence in hair cells resulted in the loss of hearing. Neuronal Ca$_V$1.3 channels are mainly expressed in the soma-dendritic regions, forming clusters on the plasma membrane surface (Hell et al., 1993; Lipscombe et al., 2004; Zhang et al., 2006), and have been implicated in pace-making functions in neurons (Helton et al., 2005; Olson et al., 2005). The first human disease due to loss-of-function mutation in Ca$_V$1.3 was reported recently, known as SAN Dysfunction and Deafness (SANDD) syndrome (Baig et al., 2011). The insertion of a glycine residue in the alternatively spliced exon 8b, which is predominantly expressed in human inner hair cells (IHCs) and SAN pacemaker cells, affected the cytoplasmic end of inner pore lining S6 helix in domain 1and caused an abnormal voltage-dependent gating. Homozygous patients displayed cardiac and auditory phenotype that closely resembles the $Ca_V1.3^{-/-}$ knockout mice.

1.2.1 Unique biophysical properties and pharmacological properties

Electrophysiological and pharmacological characterization of recombinant $Ca_V1.3$ channels heterologously expressed in HEK 293 had uncovered several biophysical properties unique to this member of L-type Ca^{2+} channel family (Koschak et al., 2001; Safa et al., 2001; Xu and Lipscombe, 2001). $Ca_V1.3$ channels activate at about -55 mV, a voltage that is ~25 mV more hyperpolarized than $Ca_V1.2$ channels and the most negative amongst the L-type family. The negative activation threshold observed is independent of the tissue of origin and the auxiliary subunits co-expressed.

Unlike the $Ca_V1.2$ channels, $Ca_V1.3$ channels are significantly less sensitive to DHP antagonists such as nimodipine and isradipine (Koschak et al., 2001; Xu and Lipscombe, 2001). Sensitivity to DHP inhibition is voltage-dependent. Hence, the lower sensitivity of $Ca_V1.3$ becomes more significant at hyperpolarized membrane potentials and DHPs become especially ineffective at inhibiting $Ca_V1.3$ currents activated at foot of the current-voltage curve (Xu and Lipscombe, 2001).

$Ca_V1.3$ L-type channels open and close with fast kinetics relative to $Ca_V1.2$ channels, but comparable to $Ca_V2.2$ channels (Helton et al., 2005). The difference in activation kinetics observed could depend on cell-type, temperature, alterative splicing, and the presence of auxiliary subunits (Lipscombe et al., 2002; Liu et al., 2003b). Studies of DHP-sensitive component of L-type currents in hippocampal neurons appear as slowly activating (Mermelstein et al., 2000) due to incomplete and time-dependent DHP inhibition on $Ca_V1.3$ (due to its lower DHP sensitivity), as evidenced by the rapid opening of neuronal L-type channels studied directly without pharmacological inhibition (Liu et al., 2003b; Helton et al., 2005).

1.2.2 Tissue distribution, subcellular localization and physiological functions

Earlier works using RT-PCR, Western blot analysis and immunocytochemical studies demonstrated that $Ca_V1.3$ is co-expressed in many of the same tissues as $Ca_V1.2$, such as the SAN and heart atria, neurons, chromaffin cells, and pancreatic islets (Hell et al., 1993; Bohn et al., 2000; Xu et al., 2003). Although $Ca_V1.2$ and $Ca_V1.3$ are often found in the same general neuronal compartments – namely the neuronal cell bodies and proximal dendrites, as well as both the synaptic and extrasynaptic compartments, immunostaining analysis revealed a distinct difference in subcellular localization (Hell et al., 1993; Westenbroek et al., 1998; Zhang et al., 2006). $Ca_V1.3$ channels are generally distributed evenly in the cell surface membrane of cell bodies and proximal dendrites while $Ca_V1.2$ channels are predominant in the distal dendrites and tend to be concentrated in clusters. The soma-dendritic localization of $Ca_V1.3$ channels in hippocampal pyramidal neurons facilitates coupling of neuronal activity to gene-transcription. Ca^{2+} influx through $Ca_V1.3$ at low levels of stimulation activates cAMP response element binding protein (pCREB) neuronal nuclear transcription factors (Weick et al., 2003; Zhang et al., 2005), which acts in conjunction with nuclear translocation of pCREB co-activator TORC to promote transcription of multiple genes. The resultant changes in protein expression may mediate long-term potentiation (Deisseroth et al., 2003), such as in the amygdala and hence participate in the consolidation of fear memory (Gamelli et al., 2009).

Due to the negative activation range of $Ca_V1.3$ channels and the amount of Ca^{2+} ions entering during plateau, it has been implicated in signalling functions in pancreatic β-cells, neuroendocrine cells, photoreceptors, amacrine cells, and IHCs (Platzer et al., 2000; Safa et al., 2001; Liu et al., 2004; Sinnegger-Brauns et al., 2004). Due to the negative voltage range of about -60 and -40 in SAN cells, $Ca_V1.3$ channels could participate in diastolic depolarization functions and hence contribute to pace-making (Platzer et al., 2000; Koschak et al., 2001; Xu and Lipscombe, 2001). Similarly, neuronal $Ca_V1.3$ channels serve pacemaker function and shape neuronal firing (Helton et al., 2005; Olson et al., 2005). For instance, $Ca_V1.3$ currents were shown to feature prominently in the spontaneous action potentials and Ca^{2+} spikes in the suprachiasmatic nucleus (SCN) neurons that underlie circadian rhythms (Pennartz et al., 2002; Jackson et al., 2004). Upon depolarization or hyperpolarization above or below a critical voltage approximating $Ca_V1.3$ channels' activation threshold, the Ca^{2+} spikes became irregular or were completely abolished (Xu and Lipscombe, 2001), which is consistent with the spike-generating mechanisms involving sequential feedback between depolarization driven by low-threshold LTCC and hyperpolarization induced by Ca^{2+}-activated K^+ channels (Cloues and Sather, 2003). Modulations of $Ca_V1.3$ biophysical properties could thus affect the SCN spike frequency and the central biological clock underlying circadian rhythms.

The role of neuronal LTCCs in mood and anxiety behaviour is less clear, although a number of *in vivo* studies do suggest a role for $Ca_V1.3$ channels. In rodents, systemic application of high doses of DHPs induces anti-depressant and anxiolytic-like behaviours (Sinnegger-Brauns et al., 2004). In $Ca_V1.2DHP^{-/-}$ mice, application of DHP-channel activator BAYK8644 selectively promotes Ca^{2+} entry through $Ca_V1.3$ channels, inducing depression-like behaviour with neuronal activation of several brain regions involved in emotional processing. Recent studies using $Ca_V1.3^{-/-}$ knockout mice also suggest a role of these channels in affective behaviour, independent of its deaf phenotype (Busquet et al., 2010). These studies raise the possibility of selective modulation of $Ca_V1.3$ as a novel therapeutic concept for treatment of mood disorders.

1.2.3 The carboxyl terminal domain

Calcium influx through $Ca_V1.3$ channels is limited by calcium-dependent inactivation (CDI), a feedback mechanism that is both Ca^{2+}- and voltage-dependent. CDI develops in response to local or global elevations of intracellular Ca^{2+} sensed by channel-bound calmodulin (CaM) (Liang et al., 2003). The crucial determinants of CDI are located in the proximal third of the carboxyl terminus (C-terminus) of the high-voltage activated calcium channels, namely a consensus Ca^{2+}-binding motif (an EF hand) and an IQ-type CaM-binding motif. Alignment of the C-terminal sequences of the L-type $Ca_V1.3$ with $Ca_V1.2$ and $Ca_V1.4$ shows high conservation in the EF-hand and IQ motif (Figure 1.1).

Alternative splicing of the $Ca_V1.3$ in the C-terminus gives rise to two naturally occurring channel isoforms, with the shorter variant terminating shortly after the IQ motif, displaying a more negative window current, and faster inactivation due to enhanced CDI (Singh et al., 2008). Interestingly, $Ca_V1.4$ channels also undergo robust CDI in a CaM-dependent manner when the intrinsic gating modulator in its C-terminus was removed (Singh et al., 2006). This carboxyl terminal modulator (CTM) resides in the distal C-terminus downstream of the IQ motif, and contributes to the fine-tuning of $Ca_V1.4$ gating to prevent inactivation and thus support tonic neurotransmitter release in sensory cells. Studies by the same group identified a similar modulatory activity in $Ca_V1.3$, which was restricted to the last 116 amino acids (a.a.) in the C-terminus via truncation studies (Singh et al., 2008).

In dopaminergic (DA) neurons of the substantia nigra pars compacta (SNc), Ca^{2+} entry through LTCCs elevates cellular vulnerability to toxins used to generate animal models of Parkinson's disease (Chan et al., 2007). Expression of the shorter $Ca_V1.3_{42a}$ channels promotes Ca^{2+} entry in the DA neurons due to its more negative window current, while its faster CDI could limit Ca^{2+} entry during ensuing action potentials. Thus, the biophysical properties of $Ca_V1.3$ channels may be important in the DA neurons of SNc, which are susceptible to Ca^{2+} toxicity and neurodegeneration.

In $Ca_V1.2$, auto-inhibitory control was due to the binding interaction between a pair of exposed arginine residues in a proximal (PCRD) and negatively charged residues in α-helical motifs in a distal (DCRD) conserved region of C-terminus (Hulme et al., 2006). Fluorescence resonance energy transfer (FRET) and electrophysiological studies confirmed that the equivalent PCRD in human $Ca_V1.3$ was crucial to protein interaction with CTM-containing peptides and to confer modulation, while the two conserved negative charges in DCRD are essential for CTM-peptide binding to $Ca_V1.3$ (Singh et al., 2008). In the shorter splice variant $Ca_V1.3_{42a}$, the conserved PCRD downstream of the IQ motif as well as the CTM are missing.

Essentially, the $Ca_V1.3$-CTM and factors that modify its activity – namely alternative splicing, interaction with other proteins or post-translational modification, are crucial determinants of its electrical excitability and the subsequent physiological functions in excitable cells.

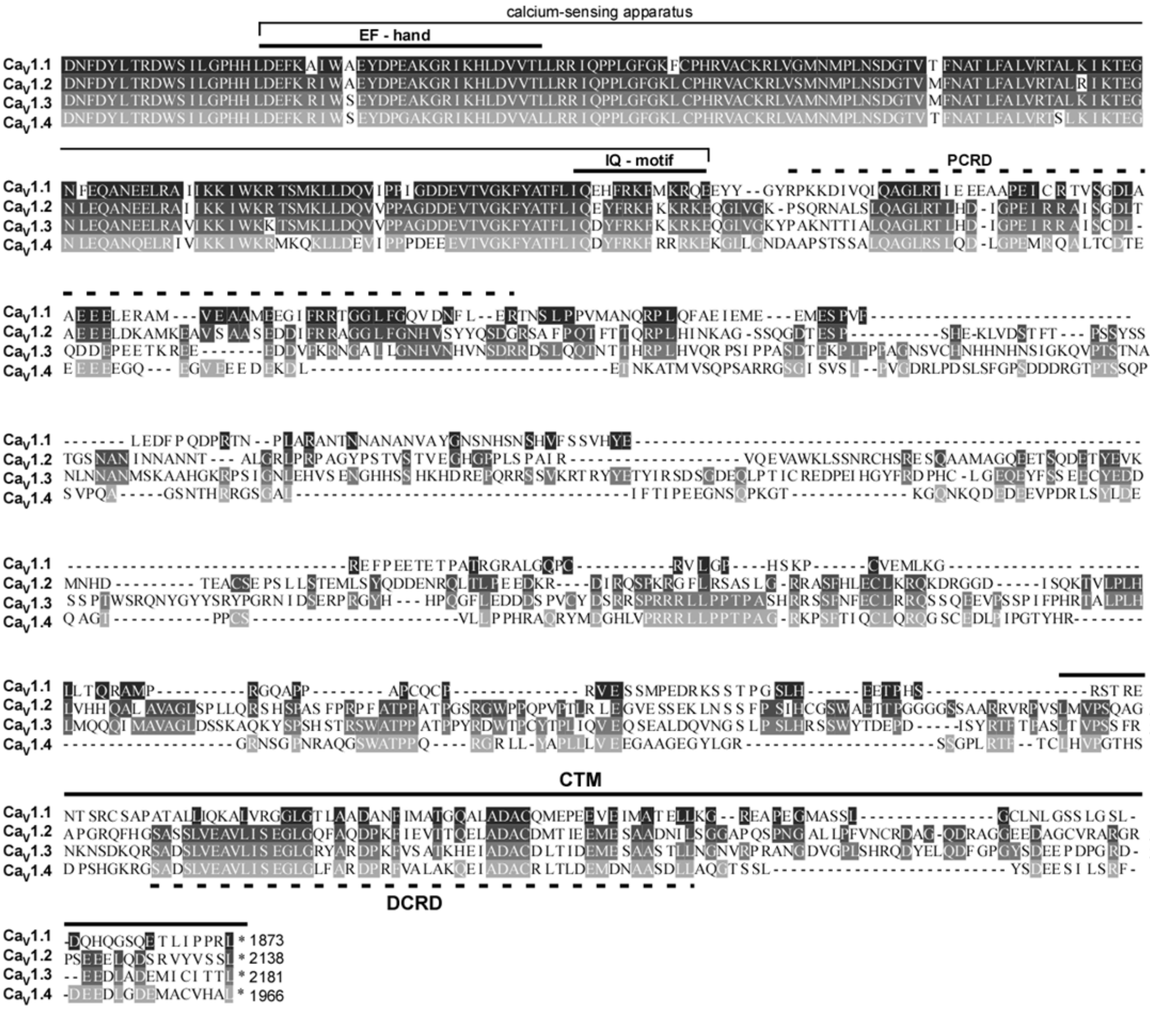

Figure 1.1 Alignment of L-type calcium channels' carboxyl-terminal amino acid sequences. Amino acid sequences are according to GenBank Accession No: Ca$_V$1.1: NP_000060; Ca$_V$1.2: NP_000710; Ca$_V$1.3: NP_000711; and Ca$_V$1.4: NP_005174. Grey-shaded areas indicate regions of sequence homology. Annotated motifs are the EF-hand, IQ-motif, C-terminal modulator (CTM), proximal conserved region of C-terminus (PCRD) and distal conserved region of C-terminus (DCRD). The EF and IQ regions form the calcium-sensing apparatus responsible for calcium-dependent inactivation (CDI).

1.3 RNA editing

Pre-mRNA editing by selective adenosine deamination is catalysed by Adenosine Deaminases Acting on RNA (ADARs), resulting in a single nucleotide change from adenosine (A) to inosine (I) (Bass, 2002). A-to-I RNA editing is a dynamic and versatile post-transcriptional mechanism of single-nucleotide recoding, which could drastically alter both the functional properties and expression levels of protein-coding mRNAs, increasing the repertoire of proteins available. Currently, most of the identified targets of A-to-I RNA editing are expressed in the mammalian nervous system, namely ion channels and neurotransmitter receptors that control electrical excitability and signal transduction. Hence, recoding of these proteins by RNA editing provides an attractive mechanism for customizing specific channel function within diverse biological niches.

1.3.1 Adenosine Deaminase Acting on RNA (ADAR)

Three members of the ADAR family (ADAR1-3) have been discovered in mammals, and are named according to their sequence of discovery. Through RT-PCR analysis and immune-staining studies, ADAR1 and ADAR2 were shown to be ubiquitously expressed, with enzymatic targets identified mainly in the nervous system (Wagner et al., 1990; Keegan et al., 2001). In contrast, expression of the latest family member ADAR3 is restricted to the brain, and has yet no known enzymatic targets (Melcher et al., 1996b). These three ADARs are highly conserved in vertebrates (Slavov et al., 2000a; Slavov et al., 2000b), and they share common functional domains – two or three repeats of the double-stranded (ds) RNA-binding motif (DRBM) and a catalytic deaminase domain. Certain structural features, such as

Z-DNA-binding domains and the arginine-rich R domain, are unique to ADAR1 and ADAR3 respectively.

The human ADAR2 gene consists of 14 exons, with exons -2 and -1 located in the 5'–untranslated region (UTR) and exons 9 and 10 in the 3'-UTR (Slavov and Gardiner, 2002). Multiple variations are also observed at the amino (N)-terminal via splicing, as indicated in Figure 1.2. In humans, the alternative inclusion of exon 1a adds 28 a.a. to the front of the commonly recognized initiator methionine residue, while retention of exon 1b in mouse results in frame-shifting and early truncation of the protein (Slavov and Gardiner, 2002). The inclusion of an in-frame *Alu* sequence, encoded by exon 5a in human ADAR2 reduces its catalytic activity by 50% (Gerber et al., 1997) while use of an alternative 3' splice acceptor site in intron 5 of mouse ADAR2 results in the inclusion of 30 nt *Alu* sequence and relatively higher catalytic activity. Furthermore, use of the alternative splice site in exon 9 leads to deletion of 29 a.a. from the C-terminal of human ADAR2 protein, resulting in a premature stop in exon 10, producing ADAR2 isoforms that have little activity on GluR-2 mRNA (Lai et al., 1997a). Splicing in the 3' UTR of both human and mouse ADAR2 further contributes to the repertoire of ADAR2 proteins. Differential protein expression of C-terminal splice isoforms, detected by western blot, implies that such subtle splicing events could also play a role in regulating the translation efficiency of ADAR2 (Kawahara et al., 2005).

Both the pre-mRNA and mRNA of ADAR2 are susceptible to A-to-I editing, mediated by ADAR2 itself (Rueter et al., 1999). In the rat ADAR2 pre-mRNA, self-editing occurs in intron 1 and exon 2, which comprised the hotspot of this gene, at six different positions – namely -2, -1, +10, +14, +23, and +24 (Rueter et al., 1999; Dawson et al., 2004). In particular, editing at position -1 in intron 1 converts an adenosine-adenosine (AA) dinucleotides to adenosine-inosine (AI) that mimics the canonical AG dinucleotides found at the 3’ splice junction (Rueter et al., 1999). The presence of AI thus acts an alternative 3’ splice acceptor site, resulting in the retention of 47 nucleotides (nt) at +28 position of exon 1. Hence, a frame-shift occurs and a truncated protein with no editing activity is generated, if the translation begins at the first initiator methionine residue. Species difference is observed in the inclusion of 47-nt isoform in the brain, with an expression of approximately 80% in mouse brain and only 15% the human brain (Slavov and Gardiner, 2002).

Alternatively, a downstream initiator methionine at amino acid position 25 in rat ADAR2 could be used to generate the functional protein for the self-edited isoforms (Rueter et al., 1999). However, in human ADAR2, the next initiator methionine only occurs at position 84, which lies in the DRBM1. Initiation of translation at this site may then compromise the RNA binding capacity of the expressed protein, and furthermore, may decrease its editing efficiency and reduce protein expression.

Transgenic mice lacking self-editing of ADAR2 express significantly higher levels of ADAR2, accompanied by increase in the editing levels of various ADAR2 substrates (Lai et al., 1997a). This implies that editing of its own pre-mRNA may thus serve as a negative feedback mechanism by which ADAR2 regulates its own expression and activity.

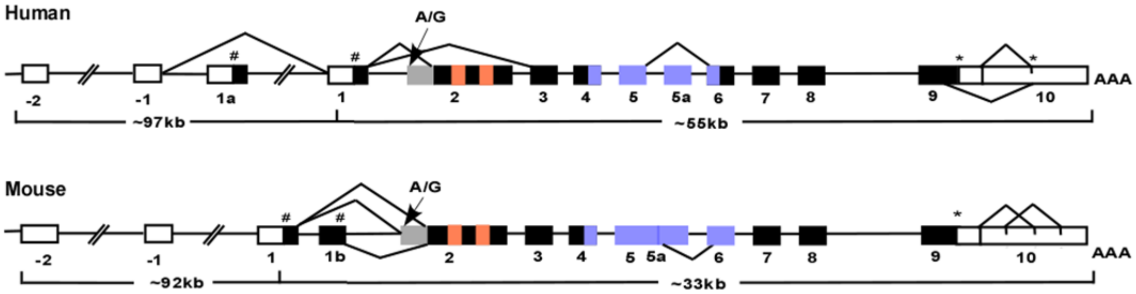

Figure 1.2 ADAR2 genomic structures for both human and mice. Exons are represented by boxes; intron, by lines. Filled boxes are coding and open boxes are non-coding. # and * indicate the positions of potential initiator methionines and stop codons respectively. The grey box before exon 2 indicates the 47 nucleotide cassette, and A/G denotes the site of editing that creates the AG splice site. Alternatively spliced exons are indicated. The pink box indicates the position of double-stranded RNA binding motif (DRBM) while the blue box indicates the position of catalytic deaminase domain. (Figure adapted from Slavov and Gardiner, 2002).

1.3.2 Mechanism of RNA editing

ADAR enzymes work by recognizing partial or complete dsRNA duplexes that are formed via base-pairing between the edited site and the editing-site complementary sequence (ECS), which is typically located in the downstream intron (Higuchi et al., 1993). One model suggests that in the presence of RNA substrate with specific secondary elements and sufficient length, conformational changes in ADAR2 protein release its DRBMII and catalytic domain from the N-terminal domain, allowing the subsequent binding of DRBMs and catalytic domain to RNA and activation of catalytic activity (Macbeth et al., 2004).

Although the mechanism of site-specific editing is still incomplete, at least two studies have shown the role of the DRBMs in the recognition and selective binding to RNA substrates (Wong et al., 2001; Macbeth et al., 2004; Stefl et al., 2006). The two repeats of the DRBM (~65 a.a.) of ADAR2 form a highly conserved α-β-β-β-α configuration structure. NMR-based model showed preferential binding of

DRBMI to loop regions and recognition of two bulges in the adjacent stem region to the edited site by DRBMII (Stefl et al., 2006). Hence, recognition of ADAR2 substrates by DRBM is structurally-dependent and length sensitive.

The catalytic domain of ADAR2 consists of amino acid residues that are conserved in several cytidine deaminases, which are involved in the cytidine-to-uridine mRNA editing mechanism and are predicted to participate in the formation of the catalytic center containing a zinc ion (Lai et al., 1995; O'Connell et al., 1995). The crystal structure of the catalytic domain of human ADAR2 reveals that histidine H394, glutamic acid E396, and two cysteine residues, C451 and C516, are involved in the coordination of a zinc atom and the formation of the catalytic center (Macbeth et al., 2005). Interestingly, an inositol hexakisphosphate IP_6 moiety is buried within the enzyme core and likely stabilizes multiple arginine and lysine residues present in the catalytic pocket. IP_6 is located very close to the catalytic center, and may thus play a critical role during the hydrolytic deamination reaction (Macbeth et al., 2005).

In vitro studies have revealed that the A-to-I editing activity of mammalian ADAR2 requires homo-dimerization (Cho et al., 2003), and *in vivo* homo-dimerization was verified through studies using bioluminescence resonance energy transfer and FRET methods (Gallo et al., 2003; Chilibeck et al., 2006). Use of mutant ADAR2 that is incapable of binding to dsRNA indicates that dimerization is independent of RNA binding, suggesting that homo-dimer complex formation is mediated through protein-protein interaction (Valente and Nishikura, 2007). In addition, a mutated ADAR subunit had a dominant-negative effect on dimer functions, indicating that DRBM of interacting monomers function cooperatively.

1.3.3 Substrates of RNA editing

In the mammalian nervous system, ion channels and neurotransmitter receptors are more common amongst the known targets of A-to-I RNA editing (Bass, 2002). Some notable examples include a number of glutamate-gated ion channels, the voltage-gated $K_V1.1$ potassium channels, the $GABA_A$ receptor and the serotonin 5-HT_{2C} receptor. In almost all cases, A-to-I editing occurs at precise and functionally important locations in the protein, changing key amino acid residues crucial for protein function (Keegan et al., 2001).

Glutamate-gated ion channels are the earliest and most extensively studied ADAR2 substrate (Melcher et al., 1996a). All five subunits (GluR-B, GluR-C, GluR-D, GluR-5 and GluR-6) are found to undergo editing at multiple sites, resulting in amino acid changes at four sites. In AMPA GluR-B subunit mRNA, adenosine in glutamate codon (C*A*G) at position 607 was changed to inosine, which encodes arginine (C*I*G) (Sommer et al., 1991). This edited Q > R site resides in the "pore loop region" of membrane segment 2, which determines the ion permeability of the glutamate channel (Seeburg et al., 2001). Channels with edited R form are less permeable to calcium. A second editing site in GluR-B causes an arginine (*A*GA) residue to glycine (*I*GA) change, which results in an enhanced rate of recovery from receptor desensitization (Lomeli et al., 1994) and decreases translocation to synaptic membrane (Greger et al., 2002; Greger et al., 2003). With the exception of Q > R site at the GluR-B subunits, editing is not 100% efficient and both edited and non-edited isoforms are expressed in the cell. In transgenic mice, failure to edit at Q > R site in GluR-B leads to epileptic seizure and death within three weeks after birth (Brusa et al., 1995).

The mRNA transcript of human $K_V1.1$ was discovered to undergo RNA editing, with an amino acid change from isoleucine (*A*TT) to valine (*G*TT) at position 400, located in the channel's S6 pore lining (Bhalla et al., 2004). Edited potassium channels exhibit rapid recovery from inactivation as compared to unedited channels, possibly due to disruption of the interaction between an inactivating particle and the channel pore (Bezanilla, 2004). Voltage-gated potassium channel plays an important role in the repolarization phase of the action potential. Hence, the faster recovery shortens the duration of each action potential and increases the frequency of firing. As potassium channels exist as tetramers, and each channel may contain different ratios of edited and unedited subunits, the physiological significance of editing on the final properties of channel inactivation and hence firing pattern of neuron has yet to be determined.

1.3.4 Role in neurophysiological and neuropathological events

Editing of mRNA transcripts is critical for normal life and development, as observed from the transgenic mice that are deficient in ADAR2. $ADAR2^{-/-}$ knockout mice develop normally, but are prone to early onset of epilepsy and die within three weeks of birth. Under-editing of the Q > R site in the GluR-B transcripts appears to be the underlying reason for epileptic seizures, which could be rescued by introducing an edited version of GluR-B gene into the $ADAR^{-/-}$ knockout mice (Higuchi et al., 2000). RT-PCR analysis of known RNA editing substrates shows that editing of certain sites is regulated during the development of the brain. These would include mRNA transcripts of the AMPA and kainite members of the glutamate receptor family – GluR-B, GluR-5 and GluR-6 (Lai et al., 1997a), the serotonin 5-HT_{2C} (Hang et al., 2008), the α3 subunit of $GABA_A$ receptor (Rula et al., 2008), and ADAR2 itself (Rueter et al., 1999). Stimulation of calcium-permeable AMPA receptors steers differentiation of neural progenitor cells (NPCs) preferentially to neuronal cells, and promotes dendritic arborisation. Overexpression of ADAR2 in NPCs results in Q > R editing and expression of calcium-impermeable AMPA receptors, which prevents AMPA-mediated differentiation, suggesting a physiological role for neurogenesis (Whitney et al., 2008).

Dysregulation of RNA editing has been linked to many human diseases. Patients with glioblastoma multiforme (GBMs) have a reduction in both ADAR2 activity and editing of the GluR-B mRNA at the Q > R site (Maas et al., 2001). Neoplasm of glial cells represents the most common tumours of the nervous system, with GBMs being the most malignant. Expression of non-edited GluR-B promotes migration and proliferation of the glioblastomas cells, driving its invasion and abnormal growth (Ishiuchi et al., 2002). Similarly, restoration of ADAR2 editing activity in astrocytoma cell lines inhibit cell migration and proliferation, which supports the correlation study between reduction of ADAR2 editing activity and grade of astrocytomas in children (Cenci et al., 2008)

1.4 Alternative splicing diversifies the function of calcium channels

Alternative splicing of $Ca_V1.3$ channels is the second post-transcriptional mechanism examined in the thesis. It is used extensively in the mammalian nervous system to increase the repertoire of proteins encoded by a set of genes. At least 75% of multi-exon genes in the human genome are alternatively spliced (Johnson et al., 2003). In voltage-gated calcium channels, alternatively spliced isoforms have been shown to exhibit diverse electrophysiological properties, and some are expressed in a developmental and tissue-specific manner or are altered in response to a physiological or pathological condition (Jurkat-Rott and Lehmann-Horn, 2004; Shen et al., 2006;

Gray et al., 2007; Liao et al., 2007; Tang et al., 2008). While the biological significance and full extent of pre-mRNA splicing is still incompletely understood, it is likely to be one of the main mechanisms for fine-tuning channel properties to achieve a high degree of functional specialization.

1.4.1 Mechanism of alternative splicing

There are several modes of alternative splicing (Figure 1.3). An exon may be excluded while its flanking neighbours are spliced together in exon skipping. Either one of two adjacent exons may be spliced in preference to the other in mutually exclusive exons. Splicing of a cryptic exon lying within an intron constitutes a cassette exon. Splicing to alternative splice donor and acceptor sites shortens or lengthens an existing exon. The splice donor site refers to the 3’-boundary of the exon, while the splice acceptor site is at the 5’-boundary. In all cases, the splicing events are specific. Splice sites are demarcated, almost invariably, by an intronic “*gt*” nucleotide pair at the splice donor boundary and an intronic “*ag*” at the splice acceptor boundary, popularly known as the “*gt…ag*” rule (Sharp and Burge, 1997). Mutations involving the canonical nucleotide residues defining splice junctions have been documented in various disease and was estimated to contributed to 15% of all point mutation-causing disease (Krawczak et al., 1992).

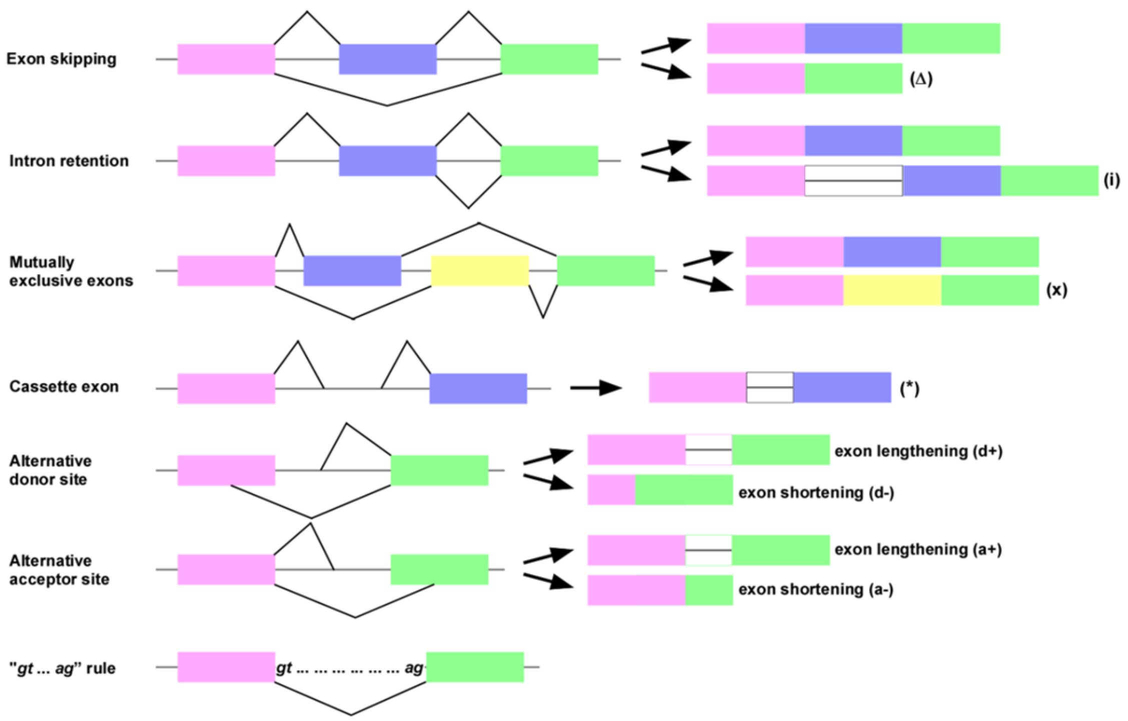

Figure 1.3 Common modes of alternative splicing. Exons can be alternatively spliced in a variety of combinations. Exon skipping joins two non-adjacent exons while the intermediate exon is excluded. Introns may be retained. In mutually exclusive exons, only one or the other exon gets spliced into the final transcript. A cassette exon may be spliced when a cryptic splice site within an intron is activated. Alternative use of donor and acceptor splice-sites could lengthen or shorten an existing exon. A pair of "*gt*" and "*ag*" nucleotides resides at the intronic boundary of splice sites.

Table 1.1 Nomenclature for describing alternatively splice exon variants. Here, we add the following suffixes or prefix to the exon number to denote the type of alternative splicing (i.e. 48a+, Δ41):

Suffix	
a^+	exon extension by alternative splice acceptor site
a^-	exon shortening by alternative splice acceptor site
d^+	exon extension by alternative splice donor site
d^-	exon shortening by alternative splice donor site
i	intron retention
x	mutually exclusion exon
*	cassette exon
Prefix	
Δ	exon skipping

Alternative splicing occurs in the spliceosome, a complex of five small nuclear RNAs, associated core proteins and several hundred proteins that assemble on nascent pre-mRNAs during transcription. The splicing pathway is an intricately choreographed series of assembly and conformational rearrangement events, punctuated by the chemical transformations of cleavage of phosphodiester bonds at exon/intron junctions and phosphodiester bond formation during exon ligation. The 5’-exon/intron boundary is first cleaved through nucleophilic attack by the 2’-hydroxyl of a specific branch-point adenosine located within the intron to generate a 5’-exon fragment and a lariat intermediate that contains intron and 3’-exon sequences and the branched adenosine (Figure 1.4). This is followed by cleavage at the 3’-exon/intron boundary via nucleophilic attack of the 3’-hydroxyl of the 5’-exon at the 3’-splice site, which ligates the exons and releases the intron in the form of a lariat. Spliceosomal proteins are not essential for catalysis since self-splicing of certain group II introns occurs through identical chemical steps, and are likely to contribute to splicing fidelity and linking splicing to other steps of mRNA biogenesis, transport, translation, and turnover.

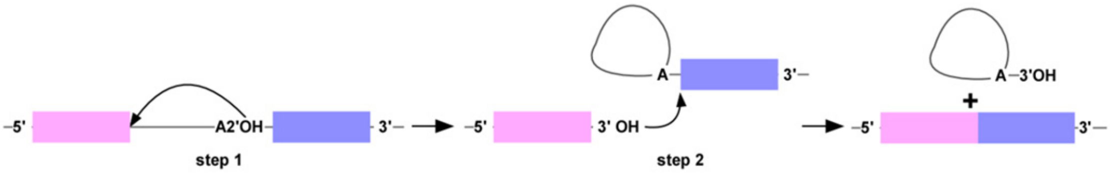

Figure 1.4 Precursor mRNA splicing pathway. Pre-mRNA splicing occurs through two sequential phosphate trans-esterification reactions. In step 1, the 2’-hydroxyl of a unique branch-point adenosine within the intron carries out a nucleophilic attack on the phosphodiester at the first splice site. This reaction cleaves the pre-mRNA at the exon/intron boundary to produce the free exon (denoted as a pink rectangle) and a lariat intermediate that contains the exon 2 sequence (denoted as a blue rectangle) and the intron with 2’-, 3’-, and 5’-ester linkages to the branch-point adenosine. In step 2, the 3’-terminal hydroxyl of exon 1 carries out nucleophilic attack on the exon 2/intron junction, in a reaction that is the chemical reverse of step 1. The second step releases the intron in the form of a lariat and ligates the exons 1 and 2.

1.4.2 Effects of alternative splicing in L-type calcium channels

Alternatively spliced exons in Ca$_V$1.2 are numerous and have been extensively studied (Tang et al., 2004; Liao et al., 2005). The distinctive segregation of some of these alternative exons into two major combinations had led to the identification of two tissue-specific Ca$_V$1.2 variants – namely “smooth muscle” and “cardiac muscle” variants with the alternative exon combinations of “1,8,9*, 32” and “1a, 8a, Δ9*, 32” respectively. Sub-variants of these have further identified (Liao et al., 2007), as were other forms of tissue and disease combinations (Tang et al., 2004; Tang et al., 2008). Protein kinase C selectively inhibits the smooth muscle variant expressing exon 1, but not the cardiac variant. Exon 8a confers a lower sensitivity towards DHP-inhibition to the cardiac Ca$_V$1.2 variant, while exon 9* enables the smooth muscle variant to activate at more hyperpolarized potentials.

Similarly, 19 different splice variants of the Ca$_V$1.4 has been identified in the human retina (Tan, 2010). Electrophysiological characterization of C-terminus splice variant 43* demonstrated that its modulated activation and inactivation properties were due to Ca$_V$1.4-CTM, and splice variant 45a- also regulates its post-inactivation recovery. It was suggested that 43* variant opens early when the rod photoreceptor recovers from a light pulse and thus serves to initiate neurotransmitter release at the synapse as well as various mechanism that maintained sustained exocytosis.

1.4.3 Ca$_V$1.3 in brain is alternatively spliced

Three alternatively spliced loci in the C-terminus of Ca$_V$1.3 transcripts from the mammalian brain were previously described (Shen, 2006; Singh et al., 2008). They are exons 41, 42 and 43. The alternative use of acceptor site in exon 41 led to the deletion of the IQ motif and a premature truncation of protein after exon 41, which resulted in abolished CDI. This isoform is observed in the hippocampus via RT-PCR analysis and immune-staining analysis of brain sections using splice variant-specific antibody (Shen, 2006). Alternative splicing of cassette exon 42a resulted in a premature stop in $Ca_V1.3$, just six a.a. after exon 41. The shorter variant activates at more hyperpolarized voltages and inactivates more robustly under the influence of calcium (Singh et al., 2008). However, in rat analogues of $Ca_V1.3_{42}$ and $Ca_V1.3_{42a}$, no major difference in the activation voltage range or the CDI was observed (Yang et al., 2006). The splicing of exon 42 to an alternative acceptor site in exon 43 led to a frame-shift with stop codon after 13 a.a. (Shen, 2006).

Interestingly, despite the early termination of translation observed in $Ca_V1.3$ C-terminus splice variants, the resultant channels are still functional. Alternative splicing controlled at the level of individual neurons could customize the proteins for optimal performance, resulting in the subtle but varied biophysical properties displayed by the principal neurons in different brain sub-regions.

1.5 Rationale and hypotheses

$Ca_V1.3$ channels play many unique physiological roles in a variety of cell types, including sensory and neuroendocrine cell signalling (Marcantoni et al., 2010), pace-making in neurons (Olson et al., 2005) and SAN cells (Mangoni et al., 2003), as well as a role in the pathology of Parkinson's disease (Chan et al., 2007; Guzman et al., 2009), which are dependent on its negative activation potential range and influx of Ca^{2+} ions during plateau or single action potentials (Helton et al., 2005). In this thesis, we focus on two forms of post-transcriptional modification – RNA editing and alternative splicing, as possible mechanisms for generating molecular diversity in channels encoded by the $Ca_V1.3$ gene, in particular examining the C-terminus.

Previous studies of alternative splicing in $Ca_V1.3$ have shown its critical importance for its negative activation range and CDI (Shen et al., 2006; Singh et al., 2008). The IQ motif is a crucial module in the calcium-sensing apparatus of LTCCs, and deletion of the motif completely abolishes CDI. In our laboratory, A-to-I RNA editing was observed in three conserved adenosine nucleotides in the IQ motif, and individual A-to-I conversion results in amino acid recoding. We proposed that the A-to-I recoding of IQ motif in $Ca_V1.3$ is likely to drastically alter CDI and aim to physiologically characterize this post-transcriptional event in the rats and mouse. In the process, we discovered that RNA editing of IQ motif is unique to $Ca_V1.3$ expressed in the central nervous system and is developmentally regulated. We hypothesized that the mechanism of RNA editing may be due to a variety of factors, and set to systematically identify them in cell culture systems. In light of the newly described CTM in $Ca_V1.3$, and the biophysical differences observed only in the human $Ca_V1.3$ splice variants, we analysed the $Ca_V1.3$ cDNA expressed in rat brain and heart and found a sequencing error in $Ca_V1.3_{42}$ clone that was characterized. Correction of mutation was sufficient for duplication of biophysical differences observed in human splice variants, similar to the single-residue switch done by Liu *et al*. (2010). In addition, we proposed that the $Ca_V1.3$ gene is likely to exhibit more alterative splicing in the C-terminus and that splice variation may serve to modulate the regulatory mechanism of this domain on CDI. We therefore undertook to systematically screen for alternatively spliced exons in rat brain and characterize them. We showed that the alternative splicing in exons 44 and 48 resulted in decreased CDI, and that the length and secondary structures between PCRD and DCRD may be necessary for regulatory effects of CTM.

Chapter 2

Physiological characterization of RNA editing of $Ca_V1.3$ IQ motif

2.1 Background and Objectives

Calcium-dependent inactivation (CDI) of L-type Ca^{2+} channels plays a critical role in controlling Ca^{2+} entry and downstream signal transduction in excitable cells. Structure-function analysis showed that even single amino-acid substitutions at critical channel hotspots could markedly alter modulatory properties, and such regulation impacts functions as diverse as neurotransmitter release, neuronal pace-making, neurite outgrowth, and gene expression. The best studied locus is a calmodulin (CaM)-binding domain approximating a consensus IQ element satisfying the amino-acid pattern IQxxxRGxxxR, with x denoting any residue. CaM binding at this IQ motif is a key determinant of CaM/channel regulation, and mutations in the central isoleucine or nearby residues can strongly attenuate Ca^{2+} regulation. In our lab, we discovered a novel RNA editing site in the IQ motif in $Ca_V1.3$ channels in rat brain. As the only other reported RNA editing of voltage-gated calcium channel is the *cacophony* gene in Drosophila melanogaster, which has high sequence similarity with $Ca_V1.3$, not much is known about this post-transcriptional modification of $Ca_V1.3$ at its IQ motif.

To address this knowledge gap, the objective of this study is to physiologically characterize RNA editing of $Ca_V1.3$. Firstly, we sought to identify all the editing sites and its frequency in $Ca_V1.3$ through sequencing analysis of $Ca_V1.3$ mRNA in mouse brain. Secondly, we aimed to determine the enzyme responsible for RNA editing of IQ motif of $Ca_V1.3$ via sequencing analysis of mRNA from $ADAR2^{-/-}$ knockout mice. Thirdly, we strived to physiologically characterize RNA editing levels of $Ca_V1.3$ via sequencing analysis of mRNA from different tissues with high $Ca_V1.3$ expression, developmentally, and in specific brain regions. Lastly, we aimed to confirm surface expression of endogenous edited $Ca_V1.3$ proteins in mouse brain, as well as surface localization of edited constructs in primary hippocampal neurons.

2.2 Materials and Methods

Materials

Experiments were carried out on Sprague-Dawley rats and C57BL mice, as approved by the institutional IACUC. The parental full-length rat $Ca_V1.3$ subunit was kindly provided by Prof. Diane Lipscombe (Brown University), while the β_{2a} and $\alpha_2\delta$ clones were gifts from A/P Terry Snutch (University of British Columbia). Parental full-length rat $Ca_V1.3$ subunit had been previously subcloned into pcDNA6/V5-His B expression vector.

Methods

Tissue preparation and total RNA extraction

Various regions of the brain and spinal cord were dissected for RT-PCR experiments. Total RNA was isolated using the Trizol method (Invitrogen, Carlsbad, CA) and first strand cDNA was synthesized with Superscript II and oligo $(dT)_{18}$ primers (Invitrogen, Carlsbad, CA). Negative control reactions without reverse transcriptase were performed in all reverse transcription RT-PCR experiments to exclude contamination by genomic DNA. Reverse transcription to generate the first strand cDNA was performed by standard methods.

Transcript scanning for edited sites in $Ca_V1.3$ IQ motif

Primer pairs were designed with the aid of Primer3 software (Rozen and Skaletsky, 2000) based on rat and mouse $Ca_V1.3$ cDNA sequence (GenBank accession numbers NM017298 and NM028981), and the sequence of the oligonucleotides (Proligo, Sigma-Aldrich) are detailed in Table 2.1. To optimize the yield of desired amplified product and to suppress non-specific amplification, a standard step-down PCR protocol was used that included a 3-cycle decrement from 59 °C to 53 °C final annealing temperature. The number of cycles for the main PCR was 35, where denaturation was performed at 94 °C for 30 sec, annealing at 53 °C for 30 sec, and extension at 72 °C for 50 sec. The final extension was at 72 °C for 5 min. PCR products were separated on a 1.5% agarose gel, isolated and purified using the Qiagen gel extraction kit. The PCR product was sent for direct automated DNA sequencing (Applied Biosystems, Foster City, CA).

Colony screening was performed by first sub-cloning PCR products into pGEM®-T Easy vector (Promega, Madison, WI), transforming 25 ng of plasmid into 25 µl of electrocompetent DH10B *Escherichia coli* cells at an electrical pulse of 25 µF capacitance, 1.8 kV and 200 Ω resistance, and then sending ~50 isolated clones for automated DNA sequencing. Three rats or mice were used for each group of animals. A total of 150 clones were screened to determine RNA editing for each brain or spinal cord region. To compare peak heights of the chromatogram bases, the peak height of guanosine was divided by the combined peak heights of adenosine and guanosine bases to estimate the percentage of RNA editing.

Table 2.1 Primers used for amplification of rat and mouse Ca$_V$1.3 at regions flanking IQ motif. Ta represents the annealing temperature.

	Primer name	Primer (5’ → 3’)	Ta (°C)
Sense	Mus1D4793IQF	CTCCGAGCTGTGATCAAGAAAATCTGG	53
Anti-sense	Mus1D5092IQR	GGTTTGGAGCTTCTGGCTCGTCA	
Sense	Rat1D5204IQF	GAGCTCCGCGCTGTGATAAAGAAA	53
Anti-sense	Rat1D5501IQR	GGTTTGGAGTCTTCTGGTTCGTCA	

In addition, primer pairs were designed to amplify the paralogous IQ motifs in other Ca$_V$ channels (GenBank accession numbers: Ca$_V$1.2, NM_009781; Ca$_V$1.4, NM_019582; Ca$_V$2.1, NM_007578; Ca$_V$2.2, NM_001042528; and Ca$_V$2.3, NM_009782). The oligonucleotide sequences are detailed in Table 2.2. The same step-down PCR protocol was utilized, and PCR product was similarly purified and sent for DNA sequencing analysis.

Table 2.2 Primers used for amplification of mouse Ca$_V$ channels at regions flanking paralogous IQ motif. Ta represents the annealing temperature. Ca$_V$ represents the channel name for the α subunit.

	Primer name	Primer (5’ → 3’)	Ta (°C)	Ca$_V$
Sense	1C5917IQF	CTTCGGGCCATCATCAAGAAAATCTGG	54	Ca$_V$1.2
Anti-sense	1C6214IQR	ATAGCCTTGTCCAACTCCTCCTCA		
Sense	1F4653IQF	GGAGCTTCGGATGGTCATCAAAAAG	54	Ca$_V$1.4
Anti-sense	1F4930IQR	TTCCTCAGTGTCATAGGTGAGGGC		
Sense	1A5670IQF	GAGCTTCGCAAGGAGATGATG	54	Ca$_V$2.1
Anti-sense	1A5996IQR	ATTCTGGCTGGGTCCTCCCTCCTGTGTT		
Sense	1B5407IQF	ACGAAGCAGCACCAGTGTGATGCT	54	Ca$_V$2.2
Anti-sense	1B5717IQR	TTTTGCCGAAGGAAAACCCGAGCTCCT		
Sense	1E5940IQF	GTGGTGCAGACAGACAGCAGCTAGACT	54	Ca$_V$2.3
Anti-sense	1E6268IQR	ACTCCGACCACTCAGGCCAGAAACA		

Tissue membrane preparation

Mouse brain tissues were cut up and homogenized in lysis buffer (10 mM Tris-base, pH 7.5, 1 mM $MgCl_2$), and mixed with NaCl at a final concentration of 150 mM before centrifugation at 1000g, 4 °C for 10 min. The supernatant was further spun at 100 000 g, 4 °C for 40 min, and pellet was resuspended in RIPA buffer (20 mM Tris-base, pH 7, 1 mM EDTA, 1 mM EGTA, 10 mM sodium-β-glycerophosphate, 1 mM sodium-orthovandate, 5% w/v glycerol, 1% w/v Triton X-100, and 270 mM sucrose). The resuspended solution was rotated at 4 °C for 1 h, before it was spun at 14 000 g, 4 °C for 30 min. The supernatant was further spun at 14 000 g, 4 °C for 30 min, and the final supernatant was used for affinity purification.

Affinity purification of $Ca_V1.3$ proteins

Membrane extract was first pre-cleared using Protein A/G Agarose beads (Pierce, Cat No: 20421). 50 µl of beads was added to 1 ml of membrane extract and rotated end-over-end for 1 h at 4 °C. The mixture was then spun at 14 000 rom at 4 °C for 5 min. The protein concentration of the resultant supernatant, containing pre-cleared membrane extract, was measured using Bradford assay. Affinity purification of $Ca_V1.3$ proteins was performed via incubation of 8 µg of membrane extract with 8 µl of anti-$Ca_V1.3$ antibody (Santa Cruz, H-240, sc-25687) and 60 µl of agarose beads overnight at 4 °C. Beads were collected, washed thrice with RIPA buffer and sent for MRM analysis.

Measurement of protein concentration

The protein concentration of affinity-purified $Ca_V1.3$ channels was determined by Bradford protein assay and the absorbance at 280 nm (GeneQuant *Pro*, Amersham Biosciences).

SDS-PAGE and immunoblotting

Two pull-down experiments were performed concurrently. The proteins from the control set were separated by denaturing SDS-PAGE according to the method of Laemmli, by using a Bio-Rad Mini PROTEAN II electrophoresis chamber. For immunoblotting, the proteins were electrophoresed and transferred to PVDF membranes. The membranes were blocked with 5% non-fat milk and subsequently probed with anti-$Ca_V1.3$ (Alomone, ACC-005, dilution of 1:200) primary antibody. Detection of the primary antibody was performed with anti-rabbit IgG Horseradish Peroxidase (HRP) (dilution of 1:10000), followed by SuperSignal West Pico Chemiluminescent Substrate reagents (Thermo Scientific).

MRM analyses of protein digest

Beads were washed with 100mM TEAB buffer, reduced with 10 mM TCEP, and then alkylated with 20 mM iodacetamide. Proteins were then digested from beads with 1 μg Trypsin (Promega) for 16 h at 37 °C. 0.5% formic acid was added to stop digest, and the supernatant was collected and freeze-dried in 96-well microtiter plate. Peptides were labeled with mTRAQ (Applied Biosystems), according to instructions manual, and freeze dried. Peptides were resuspended in 0.1% formic acid, concentrated on a trap-column (Reprosil pur, 0.3 x 5 mm, SGE, Australia, and Dr. Maisch, Germany), and eluted in a linear gradient from 5% acetonitrile to 50%

acetonitrile, 0.1% formic acid in water. For selective detective of edited peptides, a list of MRM transitions of potential tryptic peptides was generated by MRMPilot (Applied Biosystems), which predicts the collision-induced dissociated fragments and the optimized collision energies. In MRM, the first quadrupole filters the precursor mass of intact expected tryptic peptide, which is followed by peptide fragmentation in the collision cell. Finally, the third quadrupole only allows predicted fragments, based on the peptide sequence, from precursor ion to pass, and only the combination of precursor and fragment results in a signal. To prevent false positive signals, 2 to 4 MS/MS fragments per precursor were selected, depending on its length and sequence.

The targeted mass spectrometric analysis was carried out on a QTRAP4000 equipped with a TEMPO 2D nano HPLC (Applied Biosystems), FAMOS autosampler (SPARK, Holland) and micro ion spray II (Applied Biosystems). Data collection and control of instruments was done by Analyst 1.4 (Applied Biosystems).

In general, 18 peptides, wild-type (WT) and the different editing combinations, which also create additional shorter tryptic fragments due to the mutation of *Q* to *R*, and due to the RK sequence at the C-terminus, which is cut by trypsin either after the R or after the K, resulting in two peptides, were predicted, with 2 to 4 transitions predicted fragments per precursor. Cysteine was calculated as carboxymethylated, because of the reduction and alkylation steps, and methionines as oxidized, as after the preparation steps methionines are usually detected in the oxidized form in mass spectrometry. The peptides are namely - DCFR, DCFRK, FYATFLIQDCFR, FYATFLIQDCFRK, FYATFLIQDYFR, FYATFLIQDYFRK, FYATFLIR, FYATFLIRDCFR, FYATFLIRDYFR, FYATFLMQDCFR, FYATFLMQDCFRK, FYATFLMR, FYATFLMRDCFR, FYATFLMRDYFR, KFYATFLIQDCFR, KFYATFLIR, KFYATFLMQDCFR and KFYATFLMR.

Construct of HA-tagged edited $\mathrm{Ca_V}$1.3 constructs

The first four amino acids of the $\mathrm{Ca_V}$1.3 consensus IQ motif is IQDY corresponding to nucleotide sequence ATACAGGACTAC. Four edited $\mathrm{Ca_V}$1.3 α_{1D} subunits were generated from the reference WT $\alpha_{1D\text{-}IQfull}$ channels (Shen et al., 2006), now designated $\alpha_{1D\text{-}IQDY.}$ The edited subunits were named $\alpha_{1D\text{-}MQDY}$, $\alpha_{1D\text{-}IRDY}$, $\alpha_{1D\text{-}MRDY}$ and $\alpha_{1D\text{-}IQDC.}$ The $\alpha_{1D\text{-}MQDY}$ and $\alpha_{1D\text{-}IQDC}$ edited clones were generated by replacing a *Bst*EII/*Not*I RT-PCR fragment containing the respective edited sites into the reference clone. The other edited clones were generated by *in-vitro* mutagenesis using the primers listed in Table 2.3.

Table 2.3 Primers used for *in-vitro* site directed mutagenesis at IQ motif of $\mathrm{Ca_V}$1.3. Ta represents the annealing temperature. The nucleotides coding for mutant amino acids are italicized and underlined.

	Primers name	**Primer (5' → 3')**	**Ta (°C)**	**Mutant**
Sense	IRDY-F	TGATACG*G*GACTACTTTAGG	58	IRDY
Anti-sense	IRDY-R	CCTAAAGTAGTCC*C*GTATCA		
Sense	MRDY-F	TGAT*G*C*G*GGACTACTTTAGG	58	MRDY
Anti-sense	MRDY-R	CCTAAAGCAGTCC*C*G*C*ATCA		

The generation of HA-tagged $\mathrm{Ca_V}$1.3 construct has been described by Zhang *et al* (2006). Briefly the HA tag and the flanking sequences were inserted into extracellular S5-S6 loop of domain II of WT rat $\mathrm{Ca_V}$1.3 plasmid between amino acids Q693 and T694. The resulting sequence is 687FNFDETQ*TRH***YPYDVPDYA***VTFDEMQ*TKRS TFD694 (HA sequence is in bold, added sequence is italic) The HA tag and flanking sequences were inserted by PCR followed by ligation using *Ale*I (658) and *Bam*HI (2756) sites and verified by sequencing. The primers used are listed in Table 2.4.

Table 2.4 Primers used for construct of HA-tagged Ca$_V$1.3 channel. Ta represents annealing temperature.

	Primer name	Primer (5’ → 3’)	Ta (°C)
Sense	HA-tag-F	AAGCACCTTCGACAACTTCCC	58
Anti-sense	HA-tag-R	CTGTGTCTCATCGAAATTGAACTT	
Sense	HA-tag-overlap-F	CGGAGGGAAGTTCAATTTCG	58
Anti-sense	HA-tag-overlap-F	TGTGGGAAGTTGTCGAAGGT	
Sense	HA-tag-oligo-F	CGGAGGGAAGTTCAATTTCGATGAGACACAGACTCGTCATTATCCTTATGATGTTCCTGATTATGCTGTTACTTTTGATG	58
Anti-sense	HA-tag-oligo-R	TGTGGGAAGTTGTCGAAGGTGCTTCGCTTGGTTTGCATTTCATCAAAAGTAACAGCATAATCAGGAACATCATAAGGATA	

Hippocampal neuron culture and transfection

Low-density dissociated-cell culture of hippocampal neurons rat embryonic 18 (E18) rat was prepared, according to established protocol (Kaech and Banker, 2006). The neurons were cultured on poly-D-lysine-treated coverslips, which were suspended above an astrocyte feeder layer and maintained in serum-free N2 medium, in a 24-well plate format. Hippocampal cultures have been used widely for visualizing the subcellular localization of endogenous or expressed proteins for imaging protein trafficking. Preparation of glial feeder cultures begun at least 2 weeks in advance, and approximately 5 days was needed to prepare coverslips as a substrate for neuronal growth. Dissection of hippocampus from rat fetuses and plating of hippocampal neurons takes 2-3 hours. On days *in vitro* (DIV) 5 to 7, the primary neurons were transiently transfected with HA-$\alpha_{1D\text{-}IQDY}$, HA-$\alpha_{1D\text{-}MQDY}$, HA-$\alpha_{1D\text{-}IRDY}$, HA-$\alpha_{1D\text{-}MRDY}$, HA-$\alpha_{1D\text{-}IQDC}$ or $\alpha_{1D\text{-}IQDY}$ (1.7 μg) and rat β_{2a} (1.25 μg) and $\alpha_2\delta$ (1.25 μg), using 0.5 μl of PLUS Reagent and 1 μl of Lipofectamine LTX (Invitrogen, Carlsbad, CA). Cells were incubated in DNA-Lipofectamine LTX mixture for 5 h in 37 °C incubator, before coverslips were returned into conditioned medium.

Immunocytochemistry and confocal imaging

For immunofluorescence of cultured neurons, the following antibodies were used: rabbit polyclonal anti-$Ca_V1.3$ antibody (ACC-005, Alomone, 1:100), rat anti-HA antibody (monoclonal, clone 12CA5, Roche, 1:100), goat anti-rabbit Alexa 488 (1:400) and goat anti-rat Alexa 594 (1:400). 48 hours after transfection, neurons were fixed using 4% paraformaldehyde, washed thrice with PBS, blocked using 3% BSA/PBS, and incubated with primary antibody overnight at 4 °C. Coverslips were then washed thrice with PBS and incubated with secondary antibodies for 1 h at room temperature. Coverslips were washed thrice with PBS and mounted in *p*-phenylene-diamine-glycerol to retard photobleaching.

Preparations were analyzed using a Zeiss LSM-510 META confocal microscope using a 63x 1.4 numerical aperture (NA) oil immersion objective in the inverted configuration. Image brightness/contrast adjustments were performed on the Zeiss LSM Image Browser software, version 4.0.0.157. Images were then recorded and exported as tiff formats.

2.3 Results

Detecting RNA editing of the IQ motif in Ca$_V$1.3channels

Using mus1D4793IQF and mus1D5092IQR primers for RT-PCR of mRNA obtained from mouse brain, we obtained a PCR product of 299 base pair (bp) (Fig. 2.1A). Direct DNA sequencing of the purified product showed obvious evidence of RNA editing at two adenosine positions, characterized by conspicuous A/G double peaks in the sequencing chromatograms (Fig. 2.1B, arrows on green and black bands). These double peaks indicate that in addition to the canonical IQDY sequence, alternative sequences such as MQDY, IQDC, and MQDC could also manifest at the protein level, as summarized in Fig. 2.1B.

However, at the genomic level, the predicted amino acid sequence at the core of IQ motif is IQDY. These are coded by the nucleotides ATACAGGACTAC, as explicitly confirmed by PCR amplification and sequencing of the rat genomic DNA (Fig. 2.1C).

In order to detect rare occurrences of editing, we employed colony screening, where the purified PCR product was cloned into bacteria colonies, and sequencing was performed on amplified DNA from individual colonies (Fig. 2.2A). In addition to confirming the two sites of editing observed in Fig. 2.1B, this approach revealed a rarer locus where C*A*G (Q) was edited to C*G*G (R), which elaborates an IRDY sequence (Fig. 2.1B, bottom row). These instances of editing could then produce peptide variations as demonstrated in Fig. 2.1B, on top of other potential combinations – namely, IRDC, MRDY and MRDC. (Fig. 2.2 B).

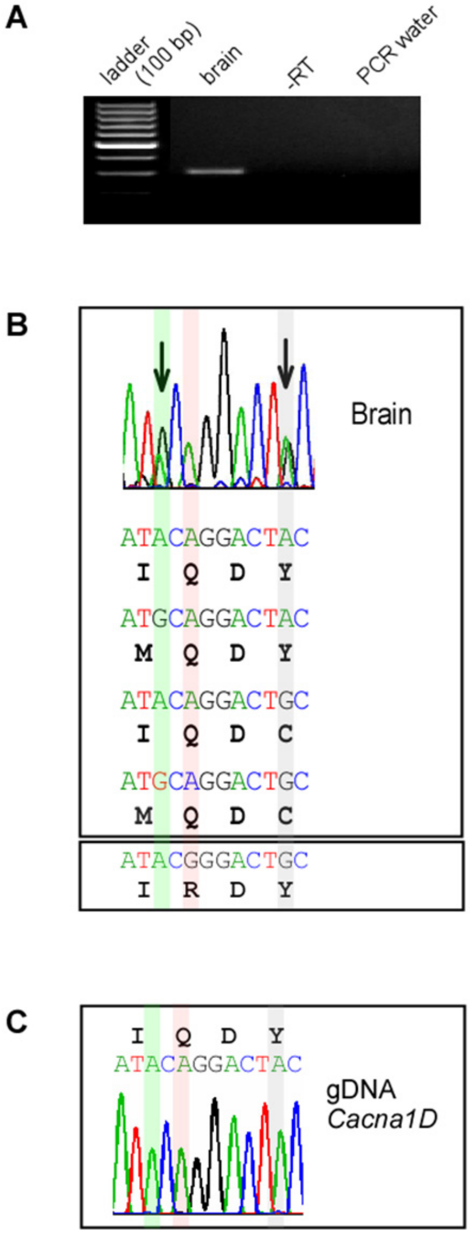

Figure 2.1 Detection of RNA editing sites in the Ca$_V$1.3 IQ motif. *A*. Exemplar PCR product (299 bp) from RT-PCR analysis of mouse brain mRNA. *B*. Direct sequencing results of RT-PCR from brain, showing distinct doublets of adenosine (A) and guanosine (G) (indicated by arrows) to generate MQDY or IQDC from unedited IQDY. Colony screening reveals an additional editing site in the IQ motif, resulting in the peptide combination IRDY. *C*. DNA sequencing chromatogram from direct analysis of PCR of genomic DNA yields a unique coding for the IQ motif at this level.

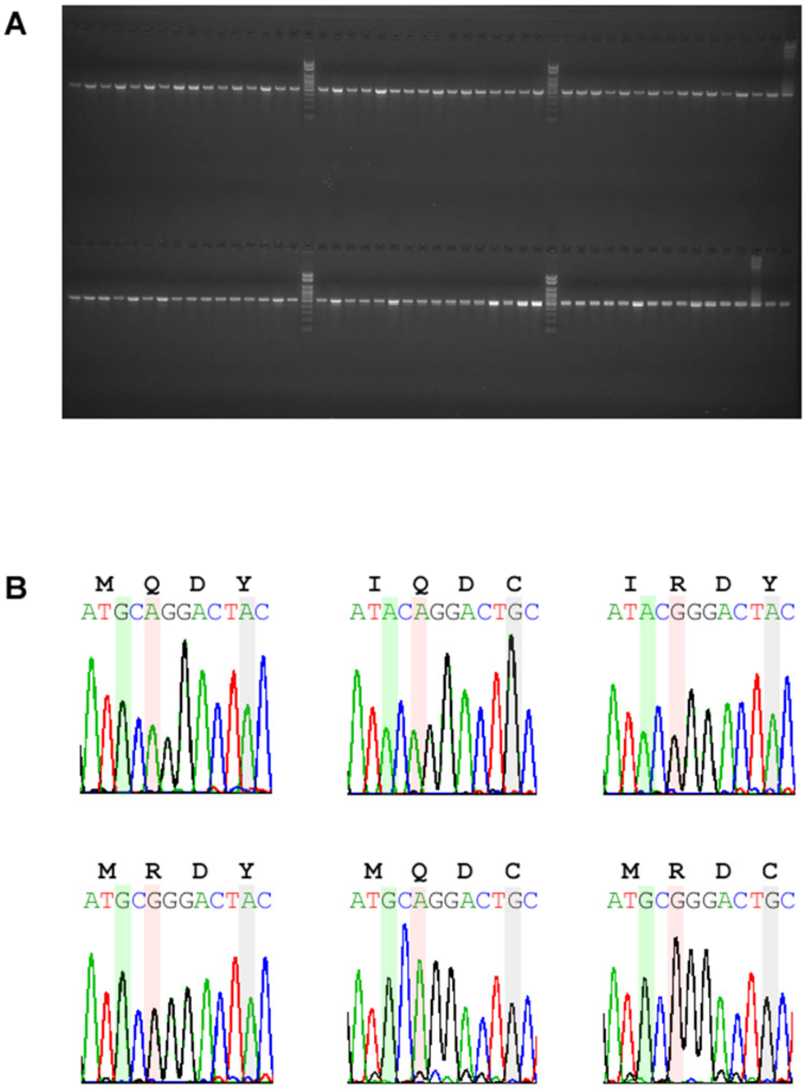

Figure 2.2 Colony screening of RNA editing sites in Ca$_V$1.3 IQ motif. *A*. Exemplar PCR products from the colony screening of 96 clones transformed with RT-PCR product ligated into pGEM$^®$-T Easy vector. *B*. Possible combinations Ca$_V$1.3 IQ motif editing in mouse brain, as evidence by DNA sequences from individual clones. These show editing at 2-3 sites in various combinations.

RNA editing of IQ motif is unique to $Ca_V1.3$ channels

In contrast to the ready detection of RNA editing within the $Ca_V1.3$ IQ motif, further regions of editing were not observed. Transcript-scanning of the complete $Ca_V1.3$ α-subunit from total mouse brain RNA, with direct sequencing of RT-PCR products, gave no indication of RNA editing outside of the IQ motif (data not shown). Detailed analysis of nearby adenosines upstream or downstream of IQ motif also showed clean adenosine peaks. Furthermore, analysis of the paralogous IQ motifs of other Ca_V channels ($Ca_V1.2$, $Ca_V1.4$, $Ca_V2.1$, $Ca_V2.2$ and $Ca_V2.3$) in mouse brain also failed to reveal additional sites of editing (Fig 2.3).

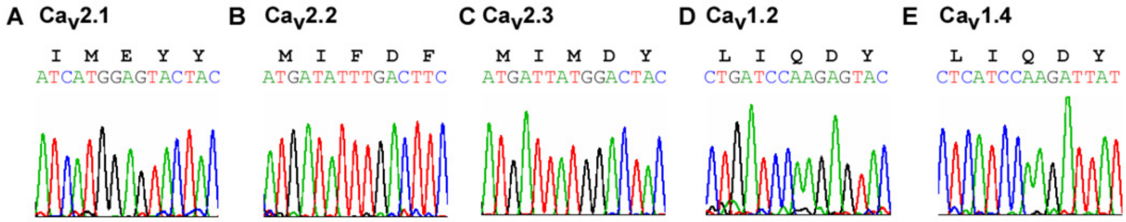

Figure 2.3 RNA editing was not detected in the paralogous IQ motifs of other voltage-gated calcium channels ($Ca_V2.1$, $Ca_V2.2$, $Ca_V2.3$, $Ca_V1.2$ and $Ca_V1.4$ channels). Direct sequencing of the RT-PCR products from mouse brain did not show any differences from published data. *A*. $Ca_V2.1$ channels; *B*. $Ca_V2.2$ channels; *C*. $Ca_V2.3$ channels; *D*. $Ca_V1.2$ channels; and *E*. $Ca_V1.4$ channels. Peptide combination of paralogous IQ motif is listed in black.

RNA editing of IQ motif is CNS-specific

Outside of the central nervous system (CNS), Ca$_V$1.3 is functionally important in cochlea (Shen et al., 2006), heart (Platzer et al., 2000), pancreas (Safa et al., 2001; Liu et al., 2004; Taylor et al., 2005), and other tissues. However, direct sequencing of cDNA from rat cochlea, heart, dorsal root ganglion cells and pancreatic islets using rat1D5204IQF and rat1D5501IQR primers demonstrated that the IQ motif of Ca$_V$1.3 channels in these tissues was not edited (Fig 2.4A-D). Overall, CNS editing of the Ca$_V$1.3 IQ motif appeared unique.

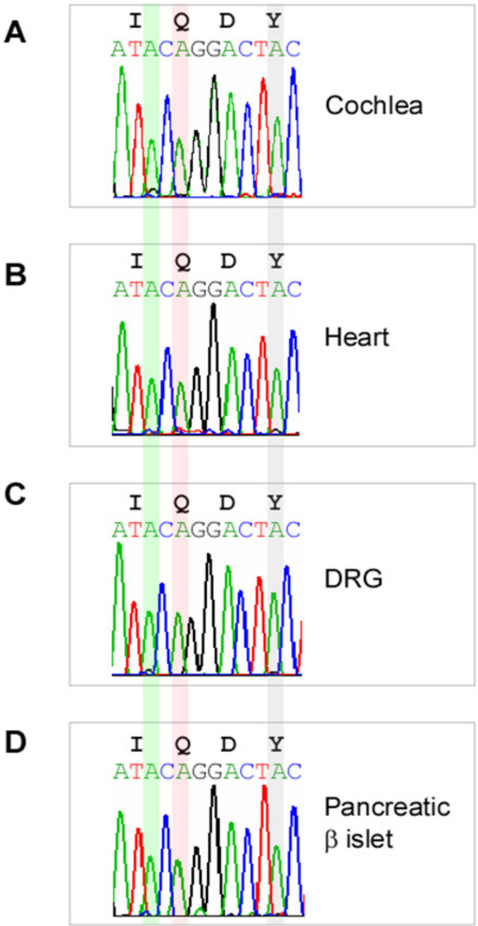

Figure 2.4 RNA editing of Ca$_V$1.3 channels' IQ motifs is CNS-specific. Direct sequencing of the RT-PCR products from tissues with high Ca$_V$1.3 channel expression showed identical patterns to the genomic analysis in Fig 2.1C, indicating no editing. *A*. cochlea; *B*. heart; *C*. dorsal root ganglion; and *D*. pancreatic islets.

ADAR2 mediates RNA editing of Ca$_V$1.3 IQ motif

Adenosine Deaminases Acting on RNA (ADARs) bind to duplex stem-loop structures within pre-mRNA and catalyses the deamination of adenosine (A) to inosine (I) (Keegan et al., 2001). This action effectively alters the codon within the mature edited mRNA, because the inosine is read off as guanosine (G) by the translation machinery, ultimately resulting in a different amino acid in the protein product. To test whether the specific deaminase isoform ADAR2 is responsible for Ca$_V$1.3 editing, we compared results from wild-type (WT) and ADAR2$^{-/-}$/GluR-B$^{R/R}$ knockout mice (Higuchi et al., 2000), focusing, in particular, on the lumbar region and whole mouse brain. Direct DNA sequencing of RT-PCR products from these regions gave strong qualitative indications of editing at each of the coloured locations (Fig 2.5A, left) identified earlier in Fig 2.1B. For more quantitative analysis, we measured the relative heights of chromatogram peaks for adenosine and guanosine at these loci, enabling specification of a percentage-editing metric shown as light-coloured bar graphs (Fig 2.5A, right). Reassuringly, colony screening produced a closely similar quantitative profile of editing (Fig 2.5A, right, darker-coloured bars). The quantitative analyses revealed an overall rank order of editing of AT*A* (I) → AT*G* (M) ~ T*A*C (Y) → T*G*C (C) > C*A*G (Q) → C*G*G (R). Indeed, while the WT background supported robust editing at the Ca$_V$1.3 IQ motif (Fig 2.5A), the knockout background was devoid of detectable editing (Fig 2.5B). This result provided strong evidence that ADAR2 is necessary for IQ motif editing.

Detailed analysis of the peptide combinations showed that doubly-edited MQDC and singly-edited MQDY were the most predominant edited combination in brain and lumbar respectively (Fig 2.5C), while editing combinations of IRDY and

IRDC were rarer. In knockout tissues, edited peptide combinations of IQDC and MQDC were observed at less than 1% (Fig 2.5D), which may be due to compensatory RNA editing by ADAR1.

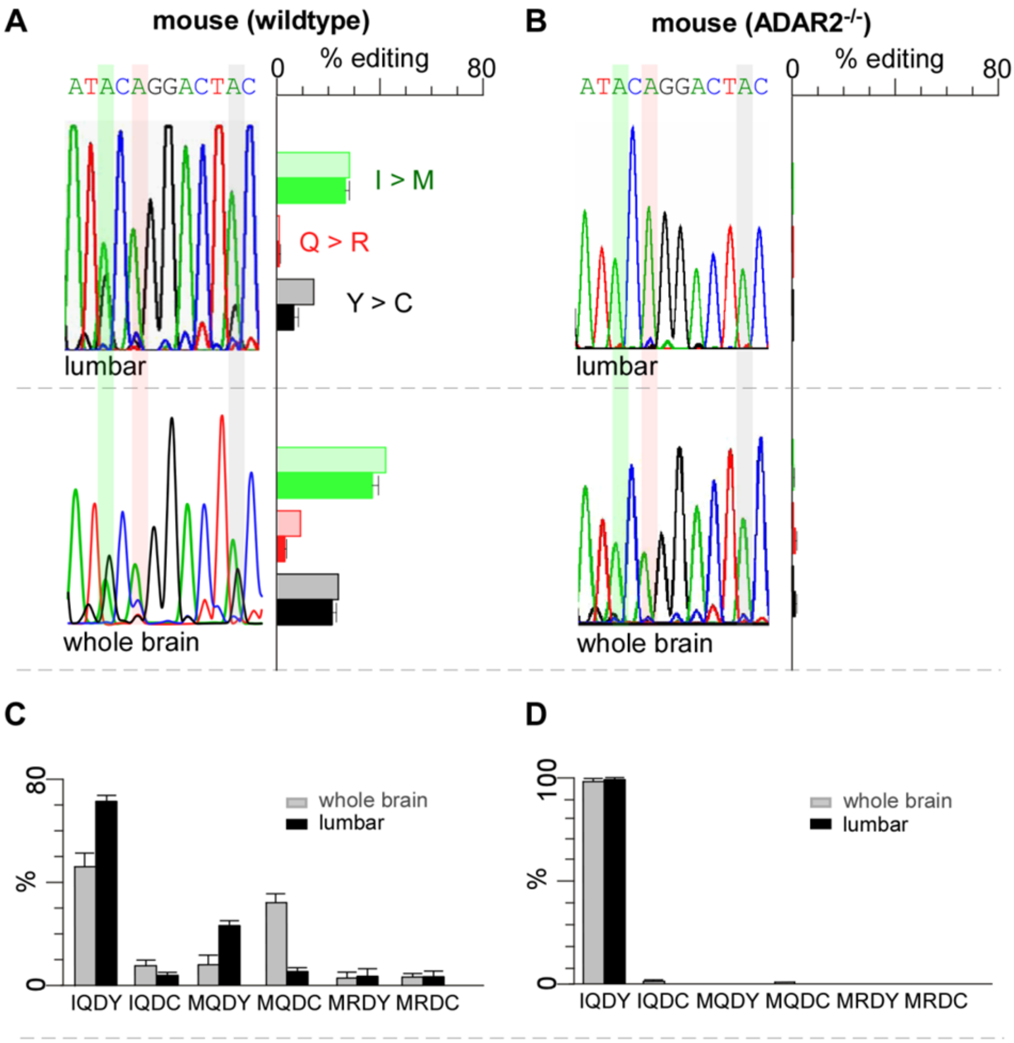

Figure 2.5 Profile of editing in Ca$_V$1.3 IQ motif in mouse lumbar and whole brain. *A*. Editing in wild-type (WT) mouse. Left column, direct DNA sequencing of mouse RT-PCR products. Right column, percentage editing at three locations (I > M, Q > R and Y > C), as calculated by measuring electropherograms heights for adenosine versus guanosine (translucent bars), or by colony counting from colony screening analysis (filled bars). The electropherograms are representative of independent RT-PCR reactions on cDNA from n=3 animals. 50 colonies were screened per animal. *Error bars* represent standard error. *B*. No editing in ADAR2$^{-/-}$/GluR-B$^{R/R}$ knockout mice. Format as in Fig 2.5A. *C*. Peptide combination of Ca$_V$1.3 IQ motif in WT mouse. IQDY depicts the non-edited combination, while IQDC, MQDY, MQDC, MRDY and MRDC depict the edited peptide combinations observed in colony screening analysis. Percentage with peptide combination, as calculated by colony counting of brain (grey bars) and of lumbar (black bars). *D*. Non-edited peptide combination IQDY expressed in ADAR2$^{-/-}$/GluR-B$^{R/R}$ knockout mice. Format as in Fig 2.5C.

Spatio-developmental RNA editing in mouse

Given the nuanced distribution of ADAR2 throughout the brain (Paupard et al., 2000), we next explored the spatio-temporal occurrence of $Ca_V1.3$ RNA editing across the CNS. Accordingly, the editing analysis introduced in Fig 2.5 was applied to individual brain regions, such as frontal cortex, hippocampus, medulla oblongata and cerebellum of mouse brain. The analysis revealed that editing was spatially regulated across the brain, with frontal cortex and hippocampus showing the most editing (Fig 2.6B). These general trends from mice were largely recapitulated in the rat brain (data not shown), with some inter-species differences present at the quantitative level.

Beyond spatial regulation, we also observed marked developmental modulation of IQ motif editing (Fig 2.7). At embryonic day 14 (E14), the $Ca_V1.3$ IQ motif lacks detectable levels of editing. By contrast, editing was observed as early as postnatal day 4 (P4), and reached adult levels by postnatal day 7 (P7). Similar trends were observed in both rats and mice, with line-graph population summaries shown at the far right.

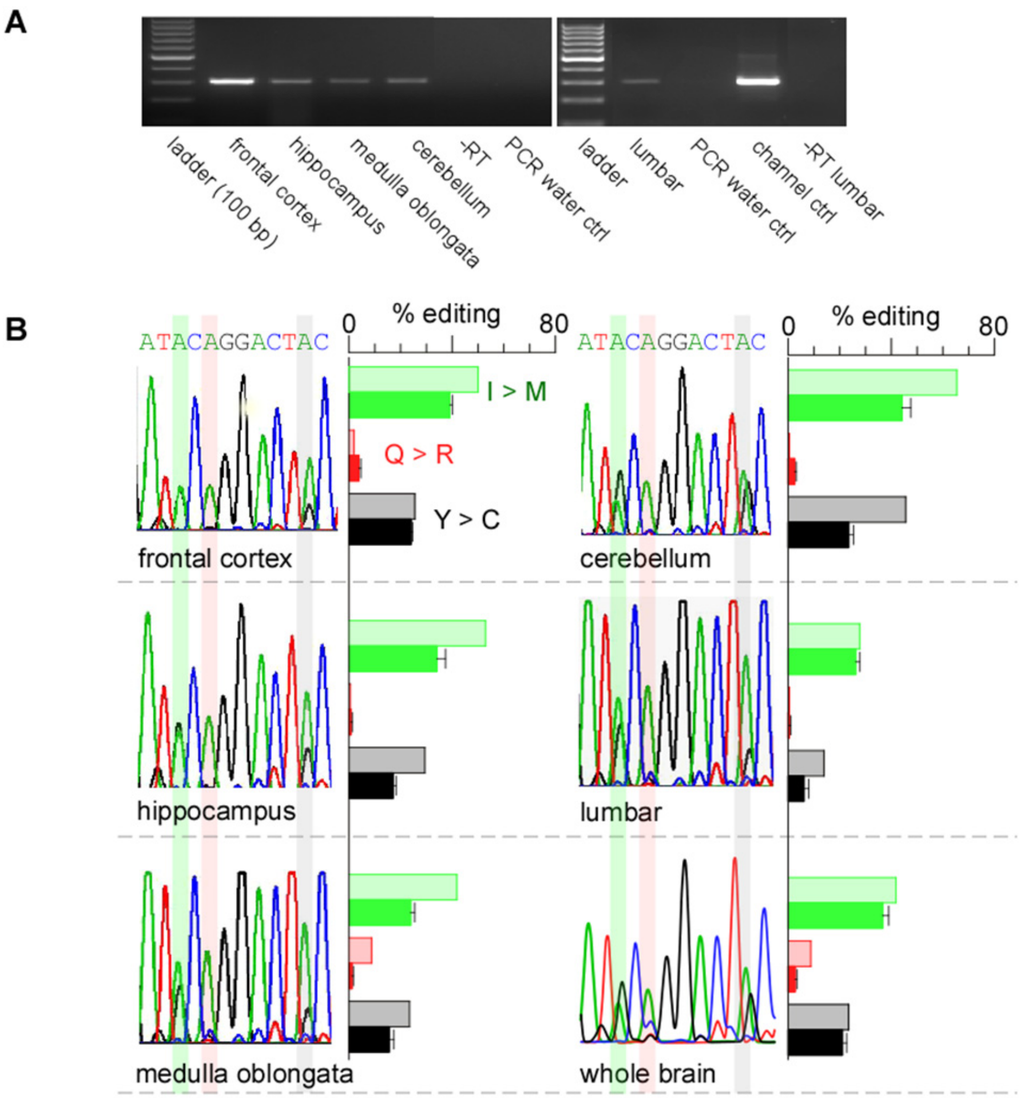

Figure 2.6 Profile of editing in Ca$_V$1.3 IQ motif in different mouse brain regions. *A*. Exemplar PCR product (297 bp) from RT-PCR analysis of mouse frontal cortex, hippocampus, medulla oblongata, cerebellum and lumbar mRNA. *B*. Left column, direct DNA sequencing of mouse RT-PCR products. Right column, percentage editing at three locations (I > M, Q > R and Y > C), as calculated by measuring electropherograms heights for adenosine versus guanosine (translucent bars), or by colony counting from colony screening analysis (filled bars). The electropherograms are representative of independent RT-PCR reactions on cDNA from n=3 animals. 50 colonies were screened per animal. A similar trend of higher editing at I > M and Y > C sites was observed from both direct sequencing and colony screening, in all regions of the brain and spinal cord.

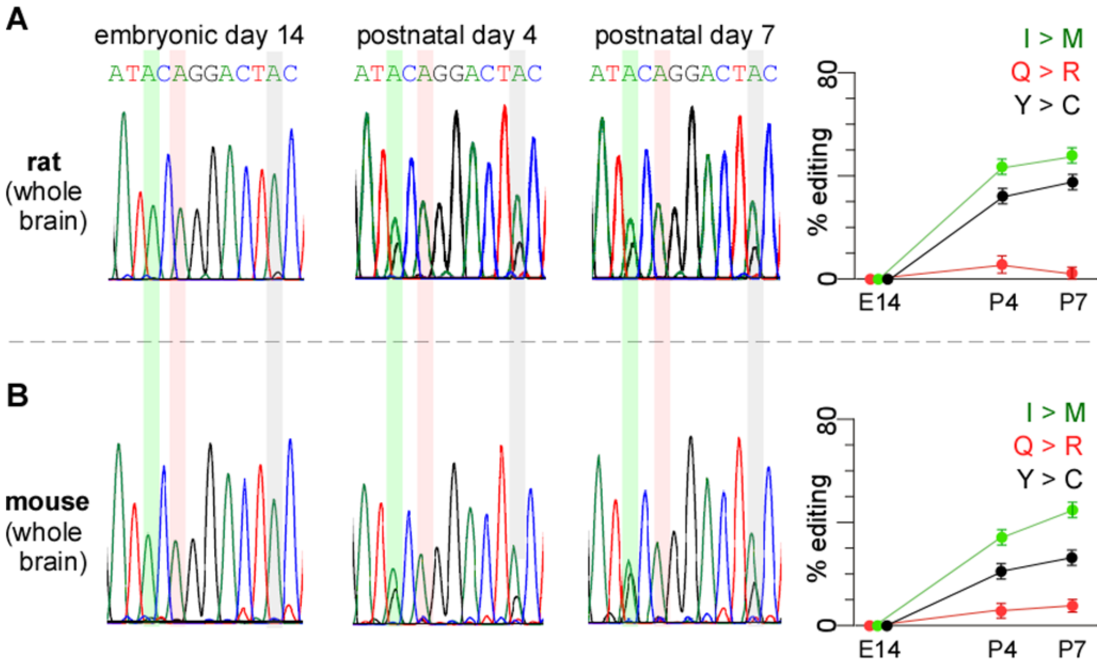

Figure 2.7 Developmental profile of editing in Ca$_V$1.3 IQ motif in mouse and rat brains. *A*. RNA editing levels at all three adenosine sites increased with age in rat whole brain. Left panel, direct DNA sequencing of RT-PCR products from brains of different ages (n = 3 animals per age). Right panel, percent editing at three locations (I > M, Q > R and Y > C), as calculated by measuring electropherograms heights for adenosine versus guanosine. *Error bars* reflect S.E.M. *B*. Similar trend of increased RNA editing levels observed in mouse whole brain. Format as in Fig 2.7A.

Surface expression and localization of edited peptides

Expression of edited $Ca_V1.3$ proteins in endogenous tissue was confirmed via high performance liquid chromatography mass spectrometry (HPLC-MS/MS) multiple reaction monitoring (MRM) of mTRAQ-labelled peptides. Targeted mass spectrometry is an assay technology capable of selective and sensitive detection and quantification of potentially any protein of interest in the proteome. In HPLC-MS/MS MRM, peptides (precursors) from candidate proteins of interest are selectively detected and caused to fragment (products) in the mass spectrometer. Due to the low expression levels of $Ca_V1.3$ proteins, it was first concentrated via affinity purification, using anti-$Ca_V1.3$ antibodies, onto agarose beads before protein identification. Signals for mTRAQ-labelled peptides containing FYATFLMR, FYATFLMRDYFR, KFYATFLIQDCFR, and KFYATFLIR isoforms of the IQ motif were distinctly detected, in addition to that of the non-edited IQ motif (FYATFLIQDYFR) (Fig 2.8). The MRM chromatograms, representative of both non-edited and edited peptides (Fig 2.9A and Table 2.5) showed good recovery of the peptides, and therefore clear identification of these molecules. Hence, I to M, Q to R and Y to C edited amino acids could be detected within the $Ca_V1.3$ IQ motif, and RNA editing does in fact yield channel proteins featuring various IQ motifs. The other $Ca_V1.3$ IQ motif variants were observed at very low intensity, either because of low abundance of the peptide or due to MS incompatibility. Immunoblot analysis of the duplicate control pull-down confirmed successful concentration of $Ca_V1.3$ proteins from wild-type mice.

To assess whether editing affects the ability of $Ca_V1.3$ channels to target to the neuronal surface membrane, we generated cDNAs encoding both non-edited (IQDY) and various edited forms of $Ca_V1.3$ channels (MQDY, IRDY, MRDY or IQDC). These channels were also endowed with an extracellular HA-tag to facilitate subsequent immunocytochemical assays of surface-membrane expression. We then transiently expressed the suite of HA-tagged Ca$_V$1.3 clones in primary hippocampal neurons. In neurons, Ca$_V$1.3 channels are localized mainly at neuronal cell bodies and proximal dendrites, and could be detected in both synaptic and extrasynaptic compartments (Hell et al., 1993; Obermair et al., 2004). Immunocytochemistry revealed similar surface expression patterns between the non-edited and edited forms of Ca$_V$1.3 variants (Fig 2.10A-E, red staining), arguing that transport of channels to the neuronal surface membrane was largely unaffected by editing. In addition, expression patterns of transfected Ca$_V$1.3 were similar to those of endogenous channels, staining predominantly the surface of cell bodies and proximal dendrites (Fig 2.9A-E, green staining).

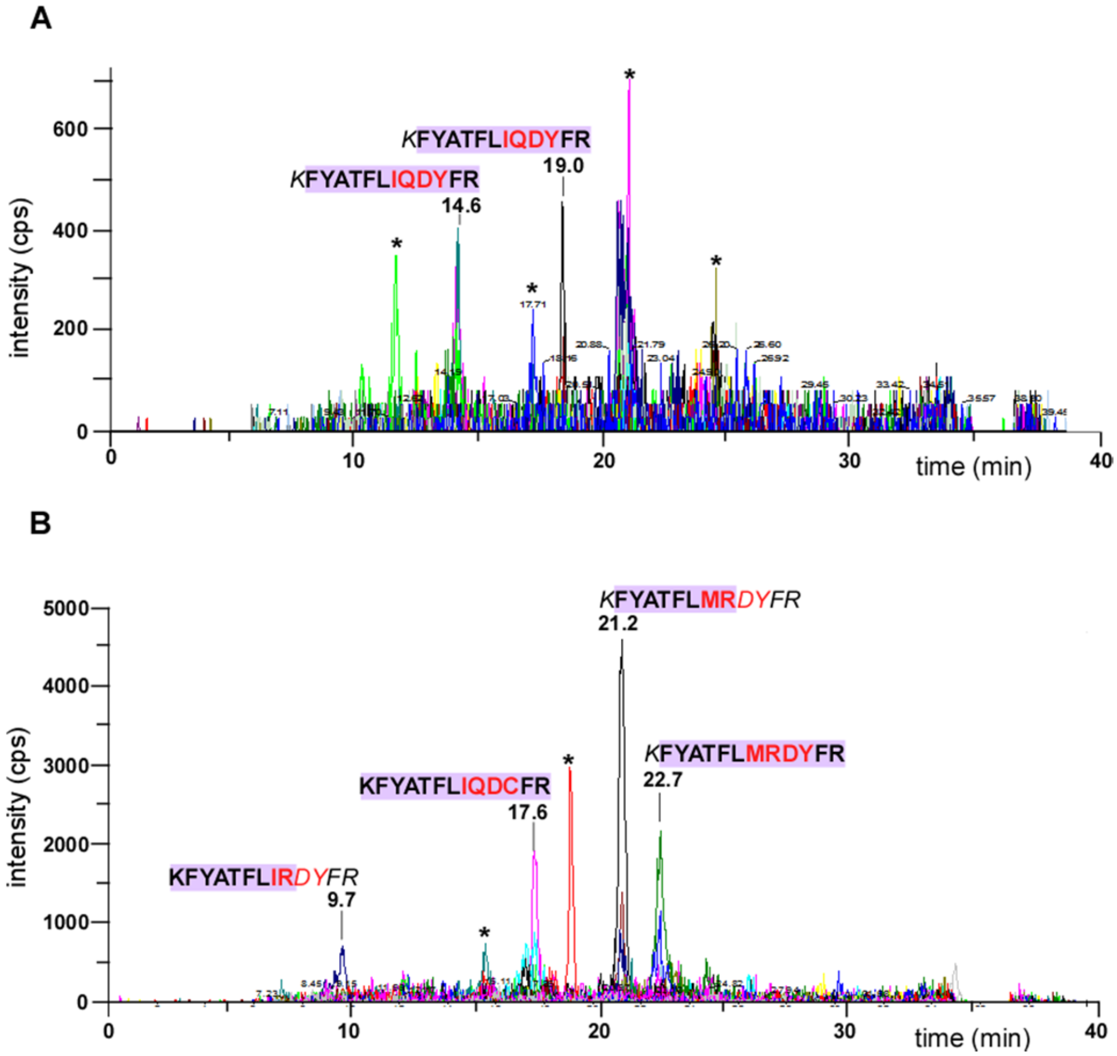

Figure 2.8 Membrane expression of edited Ca$_V$1.3 proteins was confirmed via HPLC-MS/MS multiple reaction monitoring (MRM) of mTRAQ-labelled peptides. Expression of both non-edited and edited peptides in mouse brain membrane fraction. *A*. Extracted ion chromatogram (XIC) of WT mouse brain membrane protein fraction that was specifically targeted at the non-edited IQDY peptide sequence. Peptide sequences and retention times (detected using Analyst software) are labelled above the corresponding peaks. The four amino acids in the IQ motif are displayed in red, while the predicted peptide sequence is highlighted in purple. *Asterisks* denote background. *B*. XIC of WT mouse brain membrane protein fraction, this time specifically targeted at the edited peptide sequences of the IQ motif. Format as in Fig 2.8A.

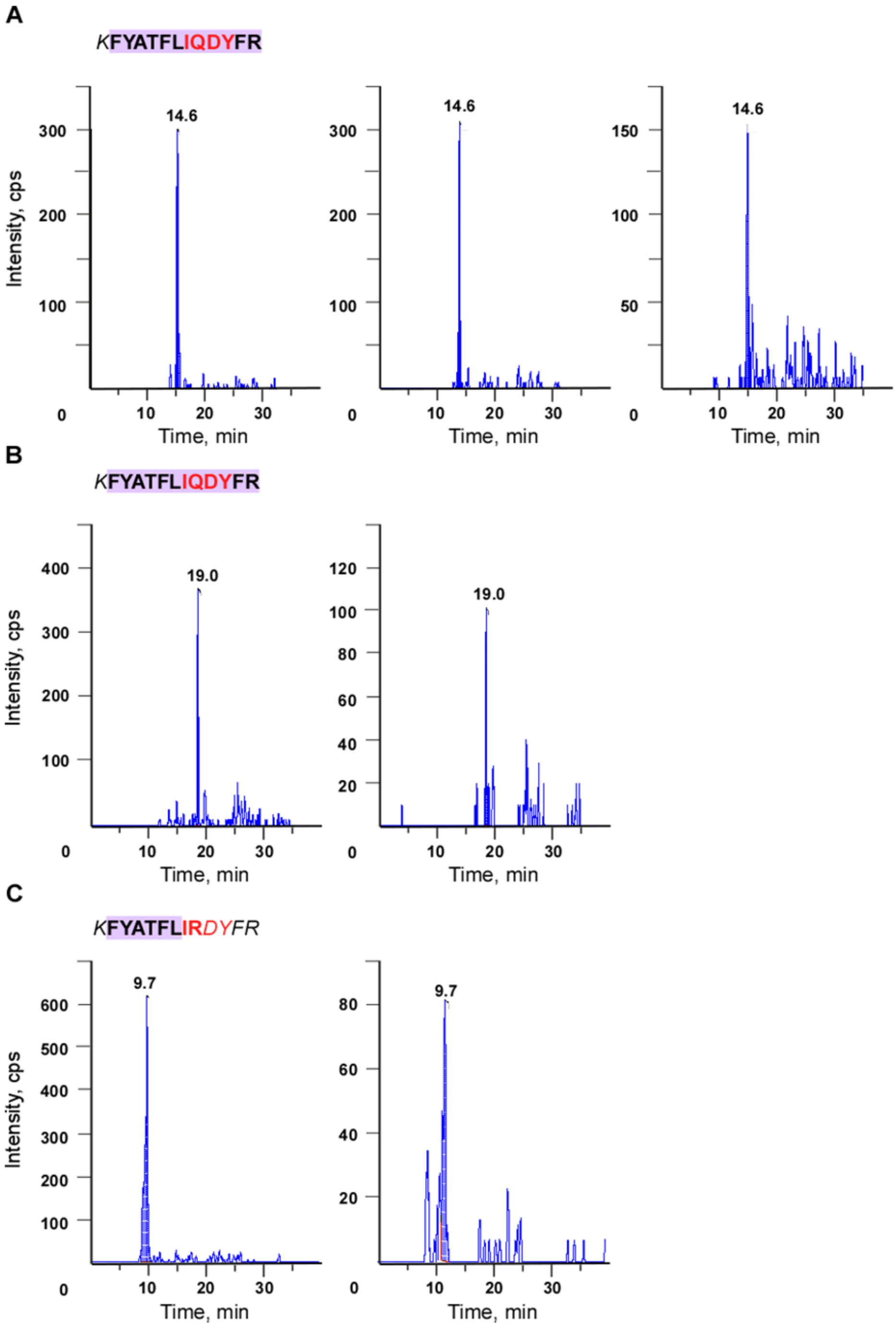
A
KFYATFLIQDYFR
Intensity, cps
300
200
100
0
14.6
10
20
30
Time, min
14.6
150
100
50
B
KFYATFLIQDYFR
400
300
200
100
19.0
120
100
80
60
40
20
C
KFYATFLIRDYFR
600
500
400
300
200
100
9.7
80
60
40
20

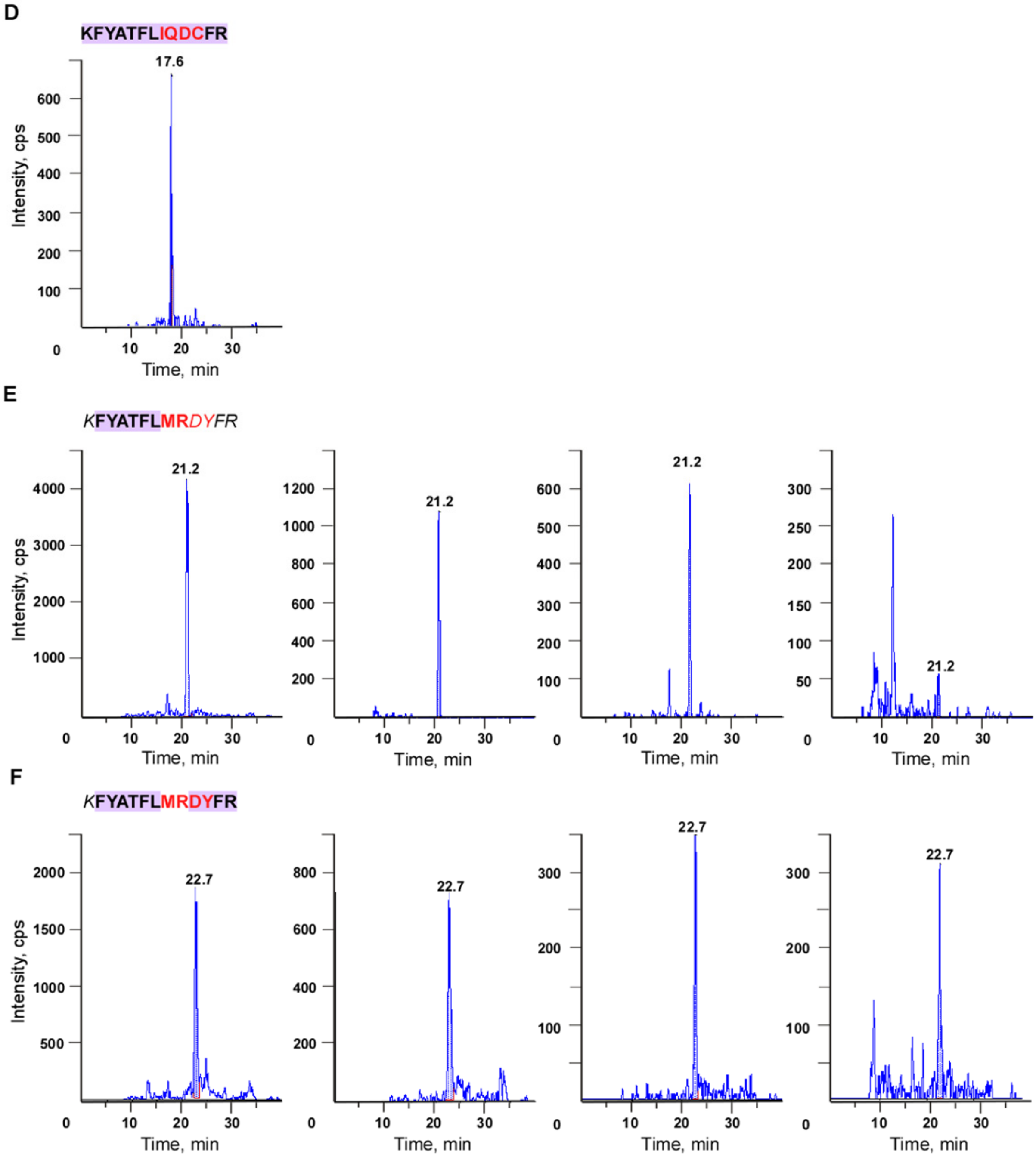

Figure 2.9 MRM transitions for the peptide sequences predicted using MRM software. Individual spectrums and transitions for each peptide labelled with mTRAQ light are shown. The MRM chromatograms, representative of non-edited peptide FYATFL*IQDY*FR (Fig 2.9A-B) and edited peptides KFYATLF*IR*, FYATFL*IQDC*FR, FYATFL*MR* and FYATFL*MRDY*FR (Fig 2.9C-F), all showed good peptide recovery and thereby clear identification of molecular species.

Table 2.5 Table accompanying Figure 2.9. The table below summarizes details of the mTRAQ-labelled peptide sequences detected in panels A-F. The columns are defined as follows (left to right), with column headings in italics. *Panel* gives the panel reference to which the detailed information at right refers; each row corresponds to individuals species identified in panels A through F. *Peptide sequence* indicates the sequence of the tryptic fragment identified in a given panel, prior to collision-cell (Q2) fragmentation. These tryptic peptides are labelled with light mTRAQ. Amino acids labelled with one mTRAQ molecule are indicated in bold, while those labelled with two mTRAQ molecules are indicated in bold and underlined. *Retention time* gives the characteristic time at which a given tryptic-peptide species exits the chromatography apparatus, and enters the mass spectrometer. For MRM transitions using two or more fragments, they have to be detected at the same retention time; otherwise the signal results from background ions and is considered random. *Molecular mass* (*m*) gives the predicted molecular mass of a given tryptic peptide, with mTRAQ label attached. *Precursor*, mass-to-charge (*m/z*) and valence (*z*) of a species at Q1. *Fragment*, mass-to-charge (*m/z*) and valence (*z*) of a species at Q3, after fragmentation in Q2. Bonafide detection of a specific IQ domain variant requires matching retention time, precursor m/z, and fragment m/z, all collectively diagnostic for a given IQ domain species.

Panel	**Peptide sequence labelled with mTRAQ light**	**Retention time (*min*)**	**Molecular mass (*m*)**	**Precursor**		**Fragment**	
				m/z	*z*	***m/z***	*z*
A	**FY**ATFLIQD**Y**FR	14.6	2003.1	1002.54	2	1241.67	1
	FYATFLIQD**Y**FR	14.6	2003.1	1002.54	2	1342.72	1
	FYATFLIQD**Y**FR	14.6	2003.1	1002.54	2	981.52	1
B	**FY**ATFLIQDYFR	19.0	1722.9	932.49	2	1202.62	1
	FYATFLIQDYFR	19.0	1722.9	622	3	1202.62	1
C	**K**FYATFLIR	9.7	1437.8	719.9	2	883.5	1
	KFYATFLIR	9.7	1437.8	480.3	3	883.5	1
D	**K**FYATFLIQDCFR	17.6	1988.0	663.7	3	1199.6	1
E	**F**YATFLMR	21.2	1203.6	602.8	2	754.4	1
	FYATFLMR	21.2	1203.6	602.8	2	917.5	1
	FYATFLMR	21.2	1203.6	402.2	3	754.4	1
	FYATFLMR	21.2	1203.6	402.2	3	683.4	1
F	**F**YATFLMRDYFR	22.7	1784.9	893.4	2	1016.5	1
	FYATFLMRDYFR	22.7	1784.9	893.4	2	1163.6	1
	FYATFLMRDYFR	22.7	1784.9	893.4	2	1264.6	1
	FYATFLMRDYFR	22.7	1784.9	596	3	1016.5	1

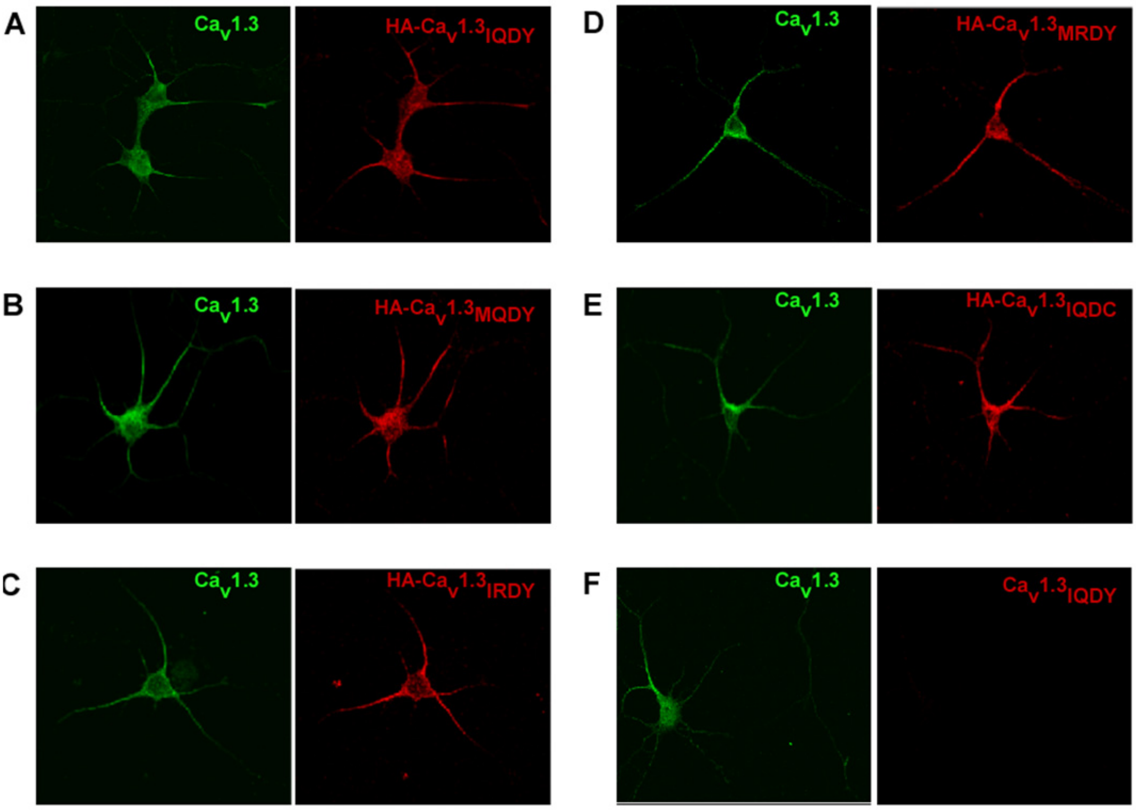

Figure 2.10 Surface localization of non-edited and edited Ca$_V$1.3 channels. Confocal images of subcellular distribution of HA-tagged Ca$_V$1.3 channels transiently transfected into E18 primary hippocampal neurons. Endogenous and transfected Ca$_V$1.3 channels were visualized using generic anti-Ca$_V$1.3 antibody (Alexa488, green) and anti-HA antibody (Alexa594, red) staining respectively. Ca$_V$1.3 plasmid without HA-tag was transfected was used as negative control. *A*. HA-tagged non-edited Ca$_V$1.3$_{IQDY}$; *B*. HA-tagged edited Ca$_V$1.3$_{MQDY;}$ *C*. HA-tagged edited Ca$_V$1.3$_{IRDY;}$ *D*. HA-tagged edited Ca$_V$1.3$_{MRDY;}$ *E*. HA-tagged edited Ca$_V$1.3$_{IQDC;}$ and *F*. non-edited Ca$_V$1.3$_{IQDY}$. The data are representative of three independent transfection experiments with HA-Ca$_V$1.3 constructs.

2.4 Discussion and Conclusion

In our laboratory, we discovered a novel RNA editing substrate in the IQ motif of $Ca_V1.3$ channel. In the present study, we aimed to confirm and physiologically characterize this editing event. The editing site was confirmed by genomic analysis of rat brain tissues, whereby only adenosine molecules, and not guanosine, were observed. Thus, the possibility that the doublet peaks observed from direct sequencing of RT-PCR is due to single nucleotide polymorphism could be eliminated. Sequencing of individual colonies revealed a third editing site in the IQ motif, increasing the possible IQ motif peptide combinations to eight. Indeed, this was confirmed by the observation of doubly- and triply-edited combinations in the colonies. In addition, we identified the enzyme responsible for editing $Ca_V1.3$ channels as ADAR2 enzyme, through detailed analysis of RT-PCR products and colony screening of $ADAR2^{-/-}$ knockout mouse brain and spinal cord mRNA. RNA editing of the $Ca_V1.3$ channel at its IQ motif appears specific to the central nervous system, since editing in other tissue regions with high $Ca_V1.3$ channel expression appears to be absent. Adding to the theme of specificity, RNA editing was not found in $Ca_V1.3$ coding regions outside the IQ motif, and editing was absent in the IQ motif of other members of the Ca_V1-2 channel family. Proteomic analyses confirmed the expression of edited $Ca_V1.3$ channel proteins within the native brain tissues. Furthermore, surface expression of edited $Ca_V1.3$ constructs was similar to that of both non-edited $Ca_V1.3$ construct and endogenous $Ca_V1.3$ channels in primary hippocampal neurons, as observed from immunocytochemical assays of transiently transfected neurons.

Adenosine-to-inosine RNA editing regulates protein function by post-translational recoding of genomic information, thereby generating molecular diversity. Most of the identified editing targets are found in the mammalian nervous system, with a predominant historical focus on the family of GluR ion channels and serotonin 2C receptors (Schmauss, 2003; Seeburg and Hartner, 2003). Beyond this historical focus, the list of editing targets is expanding. For example, outside of $Ca_V1.3$ channels, there are some instances of Ca_V channel editing exclusive of the IQ motif, though with uncertain consequences (Kawasaki et al., 2002; Tsunemi et al., 2002; Keegan et al., 2005). In other voltage-gated channels, editing of $K_V1.1/K_V\beta1.1$ channels speeds inactivation recovery (Bhalla et al., 2004), and editing of insect Na channels alters the channel gating properties (Song et al., 2004; Dong, 2007). Here, our discovery of editing within the $Ca_V1.3$ IQ motif represents a significant expansion to this group, given the striking functional modulation of Ca^{2+}-dependent feedback control at this particular locus, and the broad range of biological roles served by these channels.

Accordingly, work done by another graduate student in our laboratory demonstrated that RNA editing of the $Ca_V1.3$ IQ motif can strongly diminish the CDI of these channels (Huang et al, submitted). Furthermore, to clearly evaluate the neurological impact of $Ca_V1.3$ IQ motif editing, characterization of the repetitive firing properties of neurons in the suprachiasmatic nucleus (SCN), where the bulk of L-type Ca^{2+} current is carried by $Ca_V1.3$ channels, was performed. In particular, it was observed that RNA editing alters the frequency of repetitive action potentials and calcium spikes. As the SCN contributes a central biological clock for circadian rhythms, it is plausible that the regulation of mammalian rhythmicity constitutes one of many important potential consequences of $Ca_V1.3$ RNA editing.

Notably, ADAR2-mediated editing of the $Ca_V1.3$ IQ motif, as shown in our study, is exquisitely selective and site-specific. Firstly, such IQ motif editing was not observed in other calcium channel family members, all of which contain an IQ motif. Secondly, the nearby adenosines located upstream or downstream of the IQ motif in $Ca_V1.3$ were not edited. Finally, IQ motif editing reaction seems restricted to the central nervous system in mouse and rat, even though $Ca_V1.3$ channels are crucial to function in pancreas (Safa et al., 2001; Liu et al., 2004; Taylor et al., 2005), heart and cochlear (Platzer et al., 2000; Shen et al., 2006). Intriguingly, editing of the $Ca_V1.3$ IQ motif editing was not observed in these tissues despite the endogenous expression of ADAR2 (Melcher et al., 1996a; Gan et al., 2006). This selectivity suggests that RNA editing of the $Ca_V1.3$ IQ motif may be critical for certain biological niches, where fine-tuning of Ca^{2+} feedback on channels (CDI) is especially desirable.

Chapter 3

Mechanism for CNS-specific RNA editing of $Ca_V1.3$ IQ motif

3.1 Background and Objectives

Low voltage activation of $Ca_V1.3$ L-type Ca^{2+} channels controls excitability in central neurons and sensory cells – sensory signalling in cochlear inner hair cells (Shen et al., 2006) and pancreatic islets (Wiser et al., 1999), as well as SAN pace-making (Striessnig, 2007). However, with the exception of central nervous system, $Ca_V1.3$ is not edited in the heart, cochlea and pancreatic islets.

There are four possible models to explain the increase or lack of RNA editing in $Ca_V1.3$ calcium channel. First, ADAR2 could be regulated at the post-translational level, either via protein modification or cellular compartmentalization. Second, a cofactor in the editing machinery, which synergistically enhances the action of ADAR2, by increasing their access to certain editing sites, may be absent or inadequately expressed. Third, expression of a competitive inhibitor that hinders access of ADAR2 to editing sites, which may be in the form of a double-strand RNA binding protein that competes for binding to the $Ca_V1.3$ mRNA editing sites (Lai et al., 1997b). Fourth, the absolute and relative levels of ADAR family isoforms, ADAR1-3, and splice variants, which may perturb the dsRNA structure, and hence pattern of edited $Ca_V1.3$ (Werry et al., 2008). In order to elucidate the mechanisms regulating tissue-specific and age-dependent RNA editing of $Ca_V1.3$ channels' IQ motif, we screened several cell lines for $Ca_V1.3$ RNA editing as well as for easier manipulation and identification of crucial conditions necessary to facilitate the event. We transiently transfected the cell lines with ADAR family members at different ratios, exposed them to different cofactors of ADAR2, and exposed neuroblastoma cell lines to differentiation agents to mimic age development of neurons. The subcellular localization and expression of the ADAR2 was also examined via immunochemistry. In addition, we cloned and analysed the full length ADAR2 sequences obtained from rat brain and heart to identify and characterize the frequency of splice variants and mutations. We propose that a combination of factors may be necessary for RNA editing of $Ca_V1.3$ channel.

Furthermore, RNA editing by ADAR2 in pancreatic islets and β-cells is metabolically regulated by nutritional and energy status (Gan et al., 2006), and exposure to glucose at physiological concentration that stimulate insulin secretion may possibly also modulate RNA editing of $Ca_V1.3$ IQ motif. To address this gap in knowledge, we repeated the same experimental conditions, exposing rat and mouse insulinoma cell lines to diabetic glucose concentration for different duration to characterize possible changes in RNA editing of $Ca_V1.3$ channels.

3.2 Materials and Methods

Materials

Experiments were carried out on Sprague-Dawley rats and C57BL mice, as approved by the institutional IACUC. Rat and mouse insulinoma cell lines, INS-1, INS-1e and MIN6, were kind gifts from Dr Li Guodong (National University of Singapore, Singapore).

Methods

Tissue preparation and total RNA extraction

Various regions of the brain were dissected for RT-PCR experiments. Total RNA was isolated using the Trizol method (Invitrogen, Carlsbad, CA) and first strand cDNA was synthesized with Superscript II and oligo $(dT)_{18}$ primers (Invitrogen, Carlsbad, CA). Negative control reactions without reverse transcriptase were performed in all reverse transcription RT-PCR experiments to exclude contamination by genomic DNA. Reverse transcription to generate the first strand cDNA was performed by standard methods.

Mammalian cell culture and transient transfection

Mouse neuroblastoma cell lines – Neuro2A, N1E-115 and human neuroblastoma cell line, SH-SY5Y, were maintained in a growth media comprising of DMEM and 10% FBS, buffered with 20.71 mM sodium bicarbonate and 5.04 mM HEPES, and grown in a water saturated 5% CO_2 incubator at 37 °C. Cultures were passaged at a split ratio of 1:15 upon reaching ~80% confluency.

Mouse neuroblastoma/rat glioblastoma hybrid cell line, NG108-15 was maintained in a growth media comprising of DMEM and 10% FBS, supplemented with selective agent HAT (0.1 mM hypoxanthine, 400 nM aminopterin and 0.016 mM thymidine), buffered with 20.71 mM sodium bicarbonate and 5.04 mM HEPES, and grown in a water saturated 5% CO_2 incubator at 37 °C. Cultures were passaged at a split ratio of 1:10 upon reaching ~80% confluency.

Mouse insulinoma cell line, MIN6 was maintained in a growth media comprising of DMEM and 20% FBS, buffered with 20.71 mM sodium bicarbonate and 5.04 mM HEPES, and grown in a water saturated 5% CO_2 incubator at 37 °C. Cultures were passaged at a split ratio of 1:5 upon reaching ~80% confluency.

Rat insulinoma cell line, INS-1 and its variant, INS-1e, were maintained in a growth media comprising of RPMI-1640 and 10% FBS, supplemented with 10 mM HEPES, 2 mM L-glutamine, 1 mM sodium pyruvate and 0.05 mM 2-mercaptoethanol, and grown in a water saturated 5% CO_2 incubator at 37 °C. Cultures were passaged at a split ratio of 1:5 upon reaching ~80% confluency.

For transfection, cells were harvested at ~80% confluency, counted and seeded onto 6-well cell culture plate. The cells were seeded at a density of approximately 5 x 10^4 cells/cm^2 to ensure that sufficient cells were available after transfection for RNA extraction. The cells were then incubated for 16-24 h to allow the cells to adhere to the flat bottom of well. At about 1 h prior to transfection, the spent media was aspirated and fresh growth media containing no antibiotics was introduced. Approximately 4 μg of plasmid constructs was transfected into the cells using Lipofectamine™ 2000 (Invitrogen) transfection reagent. The plasmid DNA and 10 μl Lipofectamine™ 2000 were diluted separately in 250 μl Opti-MEM® I Reduced Serum Media each, and incubated for 5 min, before they were combined and incubated at r.t. for 30 min to allow plasmid/lipid complexes to form. The DNA/Lipofectamine™ mixture was then added to cell culture gently. The culture was returned to the incubator for 6 h. After which, the media was removed and fresh growth media was added. The cells were then incubated for at least 36 h before they were harvested for RNA extraction using Trizol (Invitrogen) method.

Detection and quantification of editing in ADAR2's editing substrates

Primer pairs were designed with the aid of Primer3 software (Rozen and Skaletsky, 2000) based on human, rat and mouse $Ca_V1.3$ cDNA sequence (GenBank accession numbers NM_000720, NM_017298 and NM_028981), rat and mouse $K_V1.1$ cDNA sequences (GenBank accession numbers NM_173095 and NM_010595), and rat and mouse GluR-B cDNA (GenBank accession numbers NM_017261 and NM_001083806) and the sequence of the oligonucleotides (Proligo, Sigma-Aldrich) are detailed in Table 3.1. To optimize the yield of desired amplified product and to suppress non-specific amplification, a standard step-down PCR protocol was used that included a 3-cycle decrement from 59 °C to 53 ^{o}C final annealing temperature. The number of cycles for the main PCR was 35, where denaturation was performed at 94 ^{o}C for 30 sec, annealing at 53 ^{o}C for 30 sec, and extension at 72 ^{o}C for 50 sec. The final extension was at 72 ^{o}C for 5 min. PCR products were separated on a 1.5% agarose gel, isolated and purified using the Qiagen gel extraction kit. The PCR product was sent for direct automated DNA sequencing (Applied Biosystems, Foster City, CA).

To compare peak heights of the chromatogram bases, the peak height of guanosine was divided by the combined peak heights of adenosine and guanosine bases to estimate the percentage of RNA editing.

Quantification of ADAR2 RNA editing catalytic activity by RT-PCR

Because ADAR2 edits its own pre-mRNA and thus generates a new splice site for alternative splicing (Fig 1.2), ADAR2 self-editing has been used as a marker for the intracellular ADAR2 deaminase activity (Maas et al., 2001). Primer pairs were designed with the aid of Primer3 software based on rat and mouse ADAR2 cDNA sequence (GenBank accession numbers NM_012894 and NM_130895), and the sequence of the oligonucleotides (Proligo, Sigma-Aldrich) are detailed in Table 3.1. To optimize the yield of desired amplified product and to suppress non-specific amplification, a standard step-down PCR protocol was used that included a 3-cycle decrement from 59 °C to 53 ^{o}C final annealing temperature. The number of cycles for the main PCR was 40, where denaturation was performed at 94 ^{o}C for 30 sec, annealing at 53 ^{o}C for 30 sec, and extension at 72 ^{o}C for 50 sec. The final extension was at 72 ^{o}C for 5 min. PCR products were separated on a 3% agarose gel, isolated and purified using the Qiagen gel extraction kit. The intensities of the splice variant bands were quantified digitally via ImageJ (NIH, US) or analytically via Agilent DNA 1000 kit (Agilent Technologies).

Table 3.1 Primers used for amplification of ADAR2 editing substrates. Ta represents the annealing temperature. Editing site states the gene and locus or peptide change upon RNA editing.

	Primer name	Primer (5' → 3')	Ta (°C)	Editing site
Sense	Mus1D4793F	CTCCGAGCTGTGATCAAGAAAATCTGG	53	*Cacna1D* IQ motif
Anti-sense	Mus1D5092R	GGTTTGGAGCTTCTGGCTCGTCA		
Sense	Rat1D5204F	GAGCTCCGCGCTGTGATAAAGAAA	53	
Anti-sense	Rat1D5501R	GGTTTGGAGTCTTCTGGTTCGTCA		
Sense	Hum1D4937F	GAACTTCGGGCTGTGATAAAGAAA	53	
Anti-sense	Hum1D5238R	CGTTTTGTTTCCTCAGGCTCG		
Sense	MusKv1141F	CATGACCACTGTGGGATACG	52	*Kcna1* I to V change
Anti-sense	MusKv1452R	GTTTTGATCAGCTGTGGTGC		
Sense	RatKv1141F	CATGACCACTGTGGGATACG	52	
Anti-sense	RatKv1486R	GTTTTGATCAGTTGCGGTGC		
Sense	MusGlu1929F	GAGGTGATTGACTTCTCGAAGC	52	*Gria2* Q to R change
Anti-sense	MusGlu2434R	GTGGAGCCAGAGTCTAATGTTCC		
Sense	RatGlu1952F	GAGGTGATTGACTTCTCCAAGCCC	52	
Anti-sense	RatGlu2457R	GTGGAGCCAGAGTCTAATGTTCC		
Sense	MusGlu2482F	GGACTTATATGAGGAGTGCAGAGC	52	*Gria2* R to G change
Anti-sense	MusGlu2894R	CAGCATTGCCAAACCAAGGC		
Sense	RatGlu2505F	GGACTTATATGAGGAGTGCAGAGC	52	
Anti-sense	RatGlu2917F	CAGCATTGCCAAACCAAGGC		
Sense	Red84F	CTCCGCCAGTCAAGAAGCCC	53	*Adarb1*
Anti-sense	Red368R	CAGGGCGTTCTTGGGTAGAACGG		

Sequencing analysis of rat ADAR2 full length clones

To characterize the ADAR2 expressed in adult rat brain and rat heart cDNA, full-length PCR was performed using ADAR2-specific primers situated in the 5'- and 3'-untranslated regions (UTRs) - -108U35 and 2322U23 respectively, and Elongase DNA polymerase (Invitrogen). The resultant ADAR2 full-length amplicons were sub-cloned into pGEM®-T Easy vector and transformed into DH10B *E.coli* cells. The positive transformants were then picked and grown in 96-well plates. A few clones from each plate were picked at random to verify that they were ADAR2 clones. The picked clones were first expanded by growing in LB broth and the plasmid DNAs extracted and sent for sequencing analysis.

Table 3.2 Primers used for amplification of rat ADAR2. Ta represents the annealing temperature. The primers without Ta are used for sequencing only. Two pairs of primers are being used to study occurrence of alternative splicing in rat ADAR2 – 84F20 and 368R23, and 1681F19 and 2167R19.

	Primer name	**Primer (5' → 3')**	**Ta (°C)**
Sense	-108U35	GCTCGCCCTGAAAGAGTTTGCCTCAGATTTGAGCC	55
Anti-Sense	2322U23	CCCTACACATCCCCACACTGCCC	
Sense	84F20	CTCCGCCAGTCAAGAAGCCC	53
Anti-sense	368R23	CAGGGCGTTCTTGGGTAGAACGG	
Sense	232F21	GTATTCCGCTCTCCAACGGGG	(sequencing only)
Anti-sense	614R22	GAAGTCTGTGTTCACGGAGAGG	
Sense	678F22	GAGCCACCCTTCTACGTAGGC	
Anti-sense	1135R24	GTCAGGTCACTGAACTTACCCAGG	
Sense	1307F23	GATAATCTCCCGAAGGTCCCTGC	
Anti-sense	1733R20	GATGCCCACCACGTTCCAGC	
Sense	1681F19	TGCTCACCATGTCCTGCAG	53
Anti-sense	2167R19	CCTTGGCAGCCTGGTACTC	

Glucose stimulation of insulinoma cell lines

It was previously shown that ADAR2 expression, editing of GluR-B and ADAR2 self-editing are markedly augmented in response to glucose at the physiological concentration for insulin secretion stimulation (Gan et al., 2006). The same protocol of glucose stimulation was repeated for rat insulinoma cell lines INS-1 and INS-1e, and modified for mouse insulinoma cell line MIN6, replacing RPMI-1640 with DMEM. Briefly, 16-24 h prior to glucose stimulation, the cells were plated at 3×10^4 cells/cm^2 in 6-wells plate to ensure sufficient cells were available for RNA extraction. The cells were first pre-cultured in 2.8 mM glucose for 24 h, followed by 16.7 mM glucose for different time points – 3 h, 6 h, 12 h, 24 h and 48 h.

Differentiation of neuroblastoma cell lines

About 16-24 h prior to application of differentiation agent, the cells were plated at 3×10^4 cells/cm^2 in 6-wells plate to ensure sufficient cells were available for RNA extraction. Cells were first rinse with PBS, before incubating with growth media containing differentiation agent and reduced serum for different time points – 1 day, 3 days, 7 days and 14 days.

Application of exogenous co-factors – zinc, magnesium

16-24 h prior to application of exogenous co-factors, the cells were plated at 5×10^4 cells/cm^2 in 6-wells plate to ensure sufficient cells were available for RNA extraction. Cells were first rinse with PBS, before incubating with growth media containing exogenous co-factors – zinc chloride or magnesium chloride, and buffered to different pH.

Semi-quantitative mRNA expression and sequence analysis of IPPK

To characterize the mRNA expression level of IPPK semi-quantitatively, PCR of both IPPK and housekeeping gene β-actin were performed. Primer pairs were designed with the aid of Primer3 software based on rat and mouse IPPK cDNA sequences (GenBank accession numbers NM_001008556 and NM_199056 respectively), and on rat and mouse β-actin cDNA sequences (GenBank accession numbers NM_031144 and NM_007393 respectively), and the sequence of the oligonucleotides (Proligo, Sigma-Aldrich) are detailed in Table 3.3. To optimize the yield of desired amplified product and to suppress non-specific amplification, a standard step-down PCR protocol was used that included a 3-cycle decrement from 58 °C to 52 ^{o}C final annealing temperature. The number of cycles for the main PCR was 25, where denaturation was performed at 94 ^{o}C for 30 sec, annealing at 53 ^{o}C for 30 sec, and extension at 72 ^{o}C for 50 sec. The final extension was at 72 ^{o}C for 5 min. PCR products were separated on a 1.5% agarose gel, and the intensities of the bands were quantified digitally via ImageJ (NIH, US).

To characterize the IPPK expressed in different mouse tissues, full-length PCR of IPPK was performed using IPPK-specific primers situated in the 5'- and 3'-untranslated regions (UTRs) – IPPK-3U25 and 1488U25 respectively, and Elongase DNA polymerase (Invitrogen). The resultant IPPK full-length amplicons were sub-cloned into pGEM®-T Easy vector and transformed into DH10B *E.coli* cells. The positive transformants were then picked and grown in 96-well plates. A few clones from each plate were picked at random to verify that they were IPPK clones. The picked clones were first expanded by growing in LB broth and the plasmid DNAs extracted and sent for sequencing analysis.

Table 3.3 Primers used for amplification of IPPK and β-actin. Ta represents the annealing temperature. The primers without Ta are used for sequencing only.

	Primer name	Primer (5' → 3')	Ta (°C)
Sense	IPPK-3U25	GGCATGGAAGAGGGGAAAATGGACG	55
Anti-Sense	IPPK1488U25	GACACCGCAGGGGAAAAGTTAGACC	
Sense	IPPK8F22	GAGGGGAAAATGGACGAGAATG	53
Anti-sense	IPPK403R20	CACAGAATCGGCCGGTGCTC	
Sense	IPPK505F18	GTAGCAACTGGAAAGTGG	
Sense	IPPK1000F18	GAAGGCCTCTACCCTCTG	
Sense	Beta_actin_for	GACTACCTCATGAAGATCC	53
Anti-sense	Beta_actin_rev	CCACATCTGCTGGAAGGTGG	

Immunocytochemistry and confocal imaging

Cells were harvested at ~80% confluency and seeded onto poly-D-lysine coated glass coverslips placed in 35 mm tissue culture dishes. The cells were plated at 2×10^4 cells/cm^2 to ensure sufficiently dispersed cells for immunocytochemistry. After designated period of treatment, cells were fixed were rinsed in PBS, fixed in 4% paraformaldehyde for 10 min, permeabilized for 10 min in PBS containing 0.2% Triton X-100 and blocked with 3% BSA in PBS for 1 h. Primary antibodies against ADAR family were applied at 4 °C overnight and then incubated with the fluorochrome-conjugated secondary antibodies for 1 h. Coverslips were then washed and mounted in ProLong® Gold Antifade Reagent with DAPI (Invitrogen) to retard photobleaching. Preparations were analyzed using a Zeiss LSM-510 META confocal microscope using a 63x 1.4 numerical aperture (NA) oil immersion objective in the inverted configuration. Image brightness/contrast adjustments were performed on the Zeiss LSM Image Browser software, version 4.0.0.157. Images were then recorded and exported as tiff formats.

3.3 Results

Developmental change in ADAR2 RNA editing activity

To investigate the mechanism for specificity in RNA editing of Ca$_V$1.3 channels, we first determined if there is a trend in age-dependent ADAR2 RNA editing in the mouse brain. Using time-mated C57 mice, we sacrificed and removed brain, heart and pancreas of the offspring from various time points, namely embryonic days 15, 17 and 19 (E15, E17, E19), new born P0, postnatal days 1 to 7 (P1-14) and 2 week-old pups P14. DNA sequencing analysis revealed that editing of Ca$_V$1.3 channels' IQ motif first occurs shortly after birth, with percent editing of 6.96 ± 2.86% and 4.58 ± 1.9% at I > Q position and Y > C position respectively (Fig 3.1A). The editing levels at the three locations increased in a non-linear manner from P0 to P7, reaching a peak with percent editing of 42.89 ±1.35%, 6.27 ±1.07% and 25.67 ±1.81% at I > Q, M > R and Y > C locations respectively (Fig 3.1A). The editing levels of the three locations in P7 mouse approximated adult levels, and percent editing levels was maintained in P14 mouse (Fig. 3.1A). A similar pattern of percent editing was observed in I > V position in potassium channel K$_V$1.1 mRNA, with editing initiating at E19 (1.51 ± 0.34%, Fig 3.1B), increasing in a non-linear manner from 2.47 ± 0.62% at P0 to 14.39 ± 1.85% at P7 and 24.77 ± 1.44% at P14. The editing levels observed were similar to those observed in adult human brain, but higher percent editing may be observed in specific brain regions (Hoopengardner et al., 2003; Decher et al., 2010). Potassium channels of the voltage-gated K$_V$1 subfamily play an important role in excitability by repolarizing membranes and shaping the firing properties of neurons, and editing of its mRNA within the sixth transmembrane domain results in an isoleucine (*A*TT) to valine (*G*TT) change (Bhalla et al., 2004).

As mentioned, ADAR2 edits its own pre-mRNA at multiple positions, mainly in intron 1 and exon 2 (Rueter et al., 1999; Dawson et al., 2004). In particular, editing at position -1 in intron 1 converts and adenosine-adenosine (AA) dinucleotide to adenosine-inosine (AI), which mimics the canonical adenosine-guanosine (AG) dinucleotide (Fig 3.5) normally found at the splice junction. The presence of AI thus acts as an alternative 3' splice acceptor site, resulting in the retention of 47 nt at +28 position of exon 1 (Fig 3.5). This generates a frame-shift and a truncated protein sequence with no editing activity, if translation starts as the first initiator methionine residue. Hence, ADAR2 self-editing and alternative splicing has been used as a marker for the intracellular ADAR2 deaminase activity, and quantified via comparing the intensity of larger splice (+47-nt) fragment to the combined intensities of both bands (Fig 3.2B, left panel). As early as E15, alternative splicing occurs at 14.62 ±1.18%, increasing in a non-linear manner to 60.77 ±1.32% at P14 (Fig 3.2B, right panel). It was observed that in adult mice brain, alternative splicing could almost reach 80%.

There is no direct correlation between the frequency of RNA editing in the ADAR2 substrates and ADAR2 deaminase activity, even though a certain threshold level of deaminase activity appears to be required for editing of $Ca_V1.3$ pre-mRNA to occur (Fig 3.2B). Q > R site of glutamate-gated receptor channel, GluR-2 was 100% edited as early as P15 (Fig 3.2A). In addition, percent editing at its R > G location was 16.38 ± 1.24% at E15 and reached 47.96 ± 3.74% by P0 (Fig 3.2A), whereby editing of $Ca_V1.3$ and $K_V1.1$ had only just initiated. At P0, self-editing and alternative splicing of ADAR2 was 40.54 ± 0.87% and may be the minimal deaminase activity required for RNA editing of $Ca_V1.3$ channels.

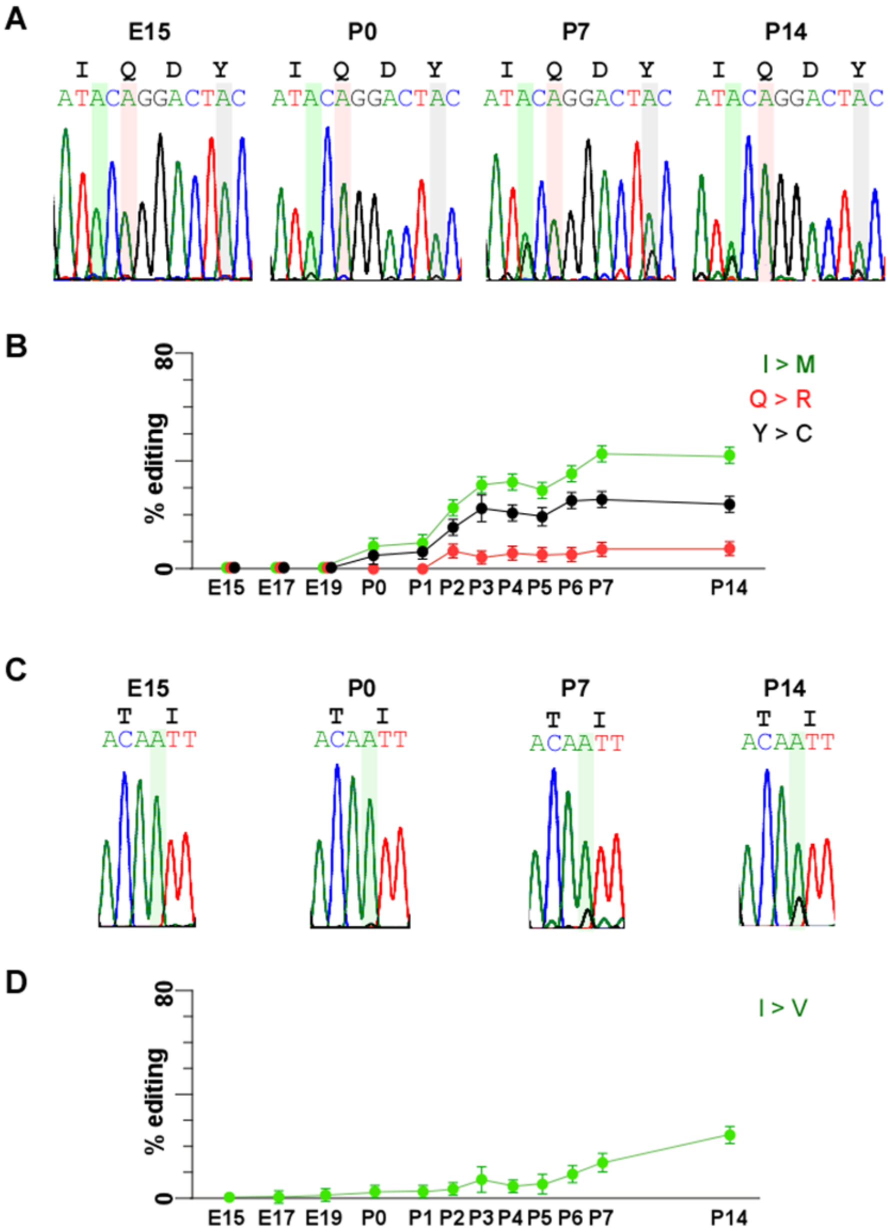

Figure 3.1 Developmental profile of RNA editing in ion channels Ca$_V$1.3 and K$_V$1.1in mouse brain. RNA editing levels at all three adenosine sites in Ca$_V$1.3 channels' IQ motif increased with age in mouse whole brain. *A*, direct DNA sequencing of RT-PCR products from brains of different ages (n = 3 animals per age). *B*, percent editing at three locations (I > M, Q > R and Y > C), as calculated by measuring electropherograms heights for adenosine versus guanosine. *Error bars* reflect S.E.M. RNA editing at I > V location in K$_V$1.1 channels increased with age in mouse whole brain. *C*, direct DNA sequencing of RT-PCR products from brains of different ages (n = 3 animals per age). *D*, percent editing at location I > V, as calculated by measuring electropherograms heights for adenosine versus guanosine. *Error bars* reflect S.E.M.

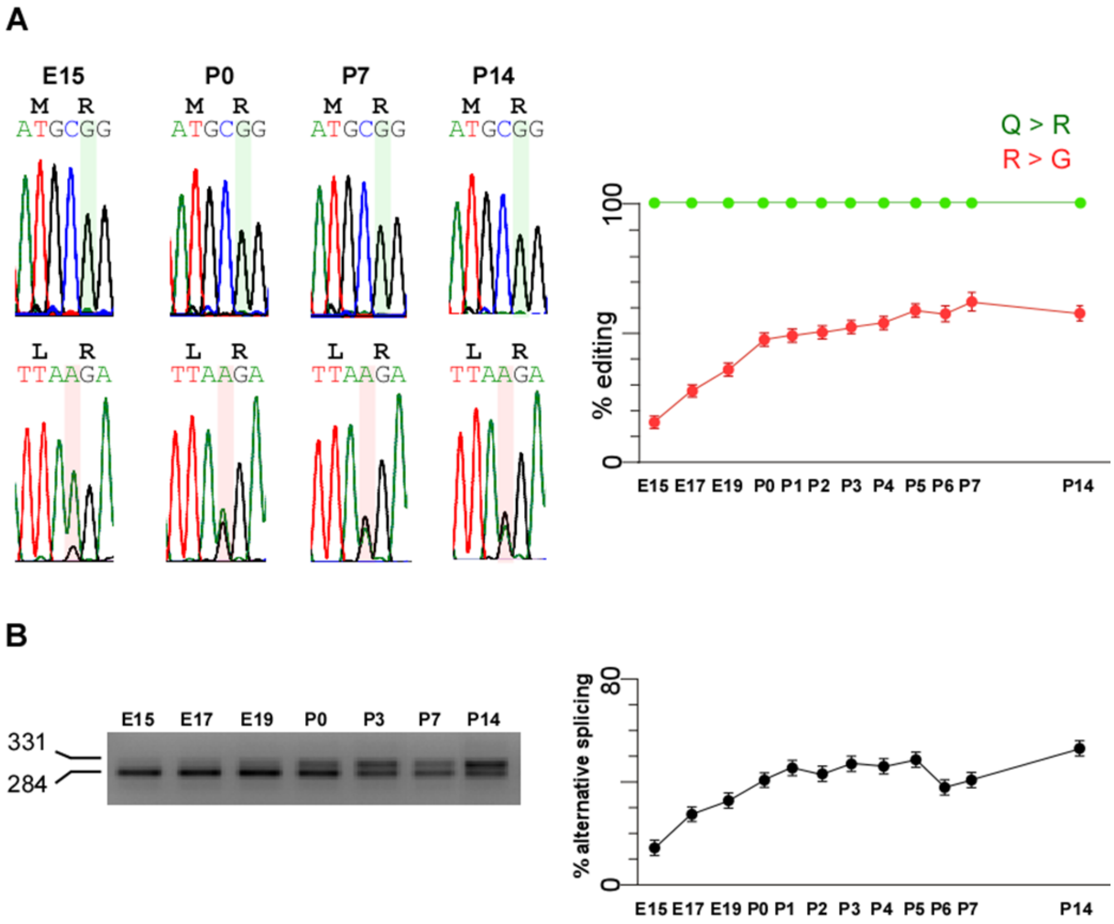

Figure 3.2 Developmental profile of editing in ADAR2 substrates in mouse brain. *A*, RNA editing at Q > R location in GluR-B receptors is 100% even at E15, while RNA editing levels at R > G location increased with age in mouse whole brain. Left panel, direct DNA sequencing of RT-PCR products from brains of different ages (*n* = 3 animals per age). Right panel, percent editing at two locations (Q > R and R > G), as calculated by measuring electropherograms heights for adenosine versus guanosine. *Error bars* reflect S.E.M. *B*, self-editing and hence alternative splicing of ADAR2 at position -1 in intron 1 increased with age in mouse whole brain. Left panel, exemplar PCR products (284 bp and 331 bp) from RT-PCR analysis of mouse brain mRNA. The extent of splicing in ADAR2 is an assessment of efficiency of ADAR2 self-editing, and hence ADAR2 deaminase activity. Right panel, percent alternative splicing at intron 1 – exon 2 boundary, as calculated by measuring peak area for 331 bp versus 284 bp. *Error bars* reflect S.E.M.

Spatial change in ADAR2 RNA editing activity

In addition to developmental profile of ADAR2 RNA editing activity, we also looked more deeply into its spatial profile, using tissues extracted from adult mice of P28 age. Similar to the tissue-specificity exhibited by RNA editing of $Ca_V1.3$, $K_V1.1$ is only edited at I > V location in the brain (Fig 3.3). The potassium channel was not detected in β-islets. Editing of GluR-2 at the Q > R location was consistently 100% in all three tissue regions examined, while percent editing at R > G location was significantly lower in β-islets (36.29 ± 2.36%, Fig 3.4A) as compared to percent editing in brain and heart (68.91 ± 1.43% and 84.32 ± 1.37% respectively, Fig 3.4A). Comparable levels of ADAR2 self-editing and alternative splicing was observed in the heart and β-islets, at 52.38 ± 1.28% and 44.29 ± 1.09% respectively, while that in brain was slightly higher at 76.39 ±1.38% (Fig 3.4B).

Although ADAR2 deaminase activity in both heart and β-islets should have been sufficient for editing of $Ca_V1.3$, as determined from the developmental profile, other factors may still be critical for this editing specificity.

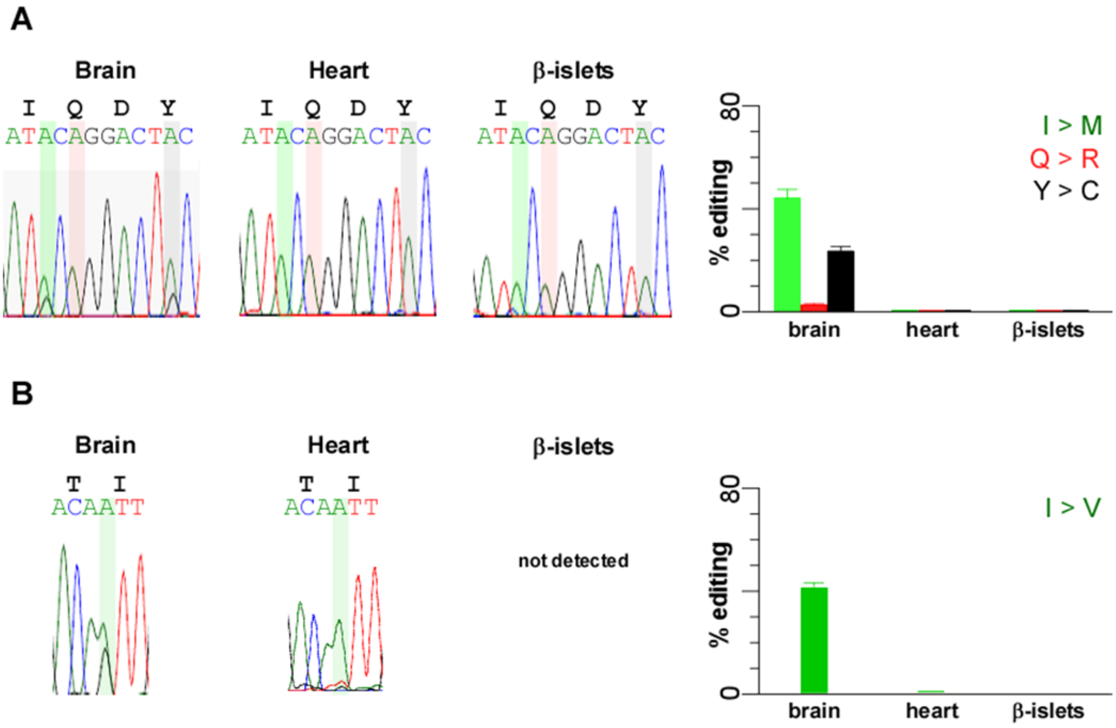

Figure 3.3 Spatial profile of editing in ion channels in adult mouse. *A*, Only Ca$_V$1.3 in mouse brain was edited. Left panel, direct DNA sequencing of RT-PCR products from whole brain, heart and β-islets of P28 mouse (*n* = 3 animals). Right panel, percent editing at three locations (I > M, Q > R and Y > C), as calculated by measuring electropherograms heights for adenosine versus guanosine. *Error bars* reflect S.E.M. (*n* = 3). *B*, Only K$_V$1.1 in mouse brain was edited. Left panel, direct DNA sequencing of RT-PCR products from whole brain, heart and β-islets of P28 mouse (*n* = 3 animals). Right panel, percent editing at location I > V, as calculated by measuring electropherograms heights for adenosine versus guanosine. *Error bars* reflect S.E.M. (*n* = 3).

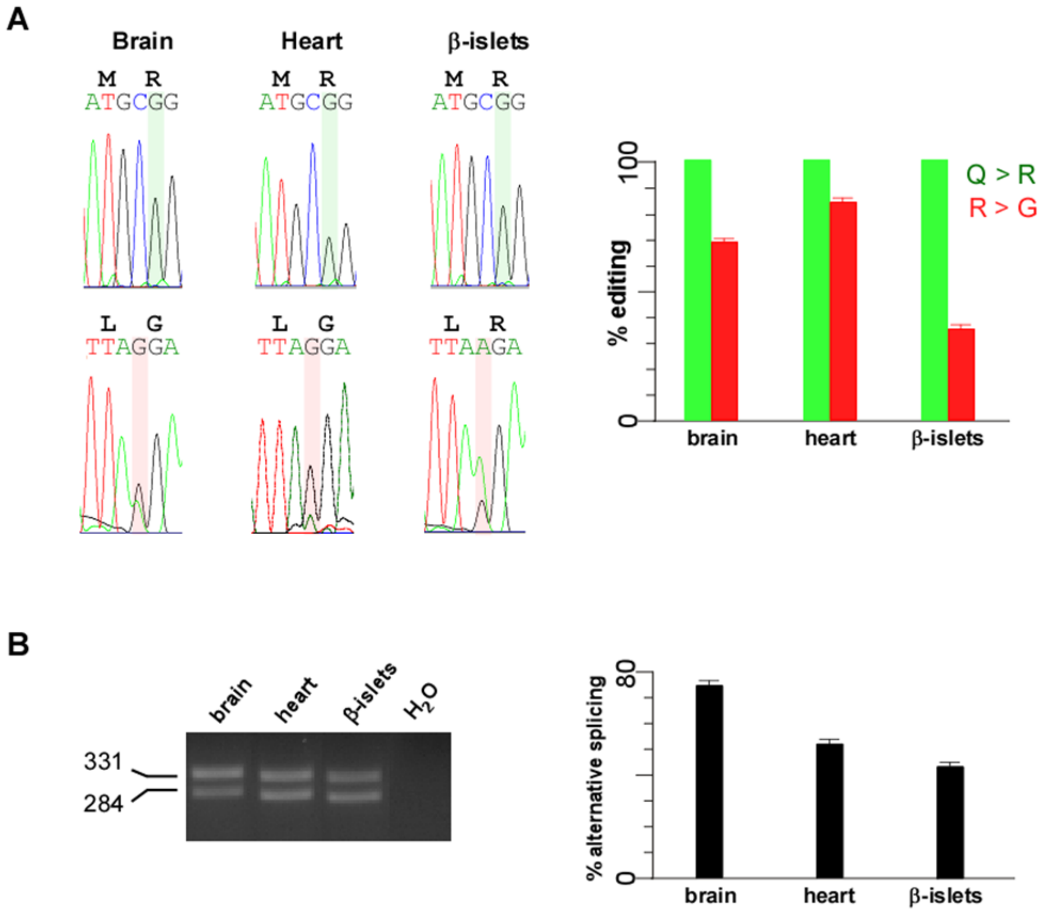

Figure 3.4 Spatial profile of editing in ADAR2 substrates in adult mouse. *A*, GluR-B was edited in all three tissues. Left panel, direct DNA sequencing of RT-PCR products from whole brain, heart and β-islets of P28 mouse (*n* = 3 animals). Right panel, percent editing at two locations (Q > R and R > G), as calculated by measuring electropherograms heights for adenosine versus guanosine. *Error bars* reflect S.E.M. (*n* = 3). *B*, Comparable levels of self-editing and hence alternative splicing of ADAR2 at position -1 in intron 1 between heart and β-islets, but significantly higher deaminase activity in brain. Left panel, exemplar PCR products (284 bp and 331 bp) from RT-PCR analysis of whole brain, heart and β-islets of P28 mouse. Data are representative of three independent experiments. Right panel, percent alternative splicing at intron 1 – exon 2 boundary, as calculated by measuring peak area for 331 bp versus 284 bp. *Error bars* reflect S.E.M. (*n* = 3).

Characterization of full length ADAR2 in rat brain and heart

Comparison of ADAR2 amino acid sequences between mouse, rat and human revealed > 90% sequence conservation, especially among the domains predicted to be involved in double-stranded RNA binding and catalytic deamination (Fig 3.5). Multiple splice variations of ADAR2 have been identified for mouse, rat and humans; yet only a subset of these RNA-processing events are conserved in all three species. Alternative splicing of exon 5a results in the production of ADAR2 protein isoforms containing an additional 40 (human) or 10 (mouse or rat) a.a. between the second and third zinc coordination residues of the deaminase domain, reducing catalytic activity by 50% in human isoforms (Gerber et al., 1997) but increasing catalytic activity by 60% in rat (Rueter et al., 1999). Alternative 3' splice site selection in intron 1 introduces an additional 47 nt to mature ADAR2, generating a -1 frame-shift that is predicted to produce a 9 kDa protein lacking the DRBMs and the deaminase domain required for protein function (Rueter et al., 1999).

Colony screening and sequencing analysis of full length ADAR2 cloned from rat brain and heart cDNA libraries revealed that the splicing frequencies at exon 5a and intron 1 varies significantly (Fig 3.6B and Table 3.3). The higher percent splicing at intron 1 of 79.2% in rat brain and 34.7% in rat heart was comparable to ADAR2 transcripts from mouse (Fig 3.4B), and could reinforce the deaminase activity in different tissues should be sufficient for RNA editing of $Ca_V1.3$ In addition, proportion of ADAR2 isoforms containing exon 5a in rat brain was higher (brain: 36.1%, heart: 18.7%, Table 3.3), which could mean higher catalytic activity in brain. Sequencing analysis revealed that of the three mutations detected, T160C and T221G could be cloning errors in rat ADAR2 clone U43534 since they were consistently observed in both rat brain and heart cDNA libraries. The unique A1310G mutation in rat heart results in an isoleucine to valine amino acid change near the first zinc coordination residue in 8.5% of ADAR2 clones (Table 3.3). However, due to the similar biophysical properties of these two amino acids, it should not significantly alter deaminase activity of ADAR2.

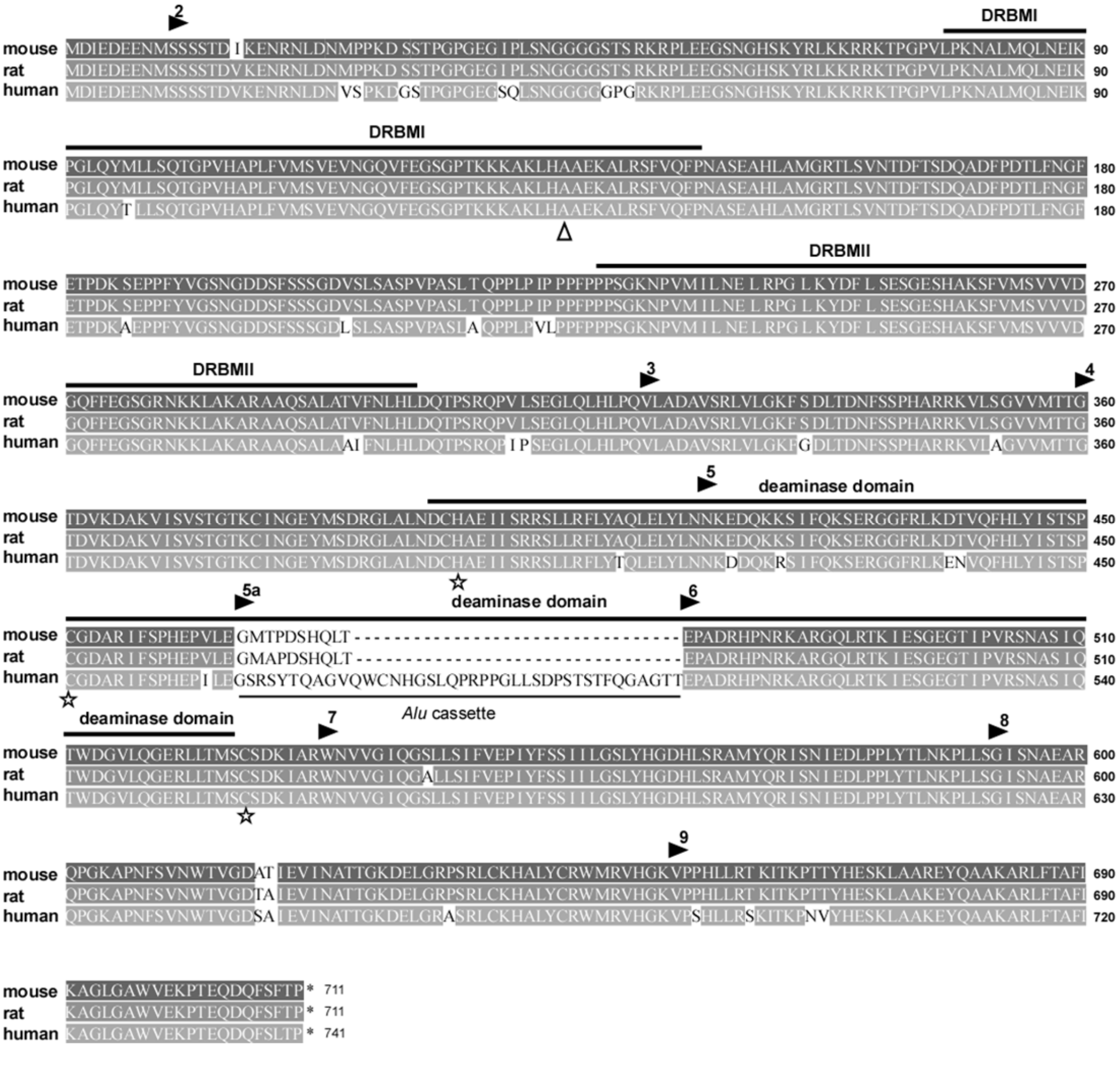

Figure 3.5 Alignment of mouse, rat and human ADAR2 amino acid sequences. Amino acid sequences are according to GenBank Accession Numbers: mouse ADAR2: NM_001024837, rat ADAR2: NM_012894, and human ADAR2: NM_015833. Grey-shaded areas indicate regions of sequence homology. Annotated motifs are DRBMI, DRBMII and deaminase domain. Critical alanine residue in DRBMI for ADAR2 dimerization is denoted by white triangle. Putative Zn^{2+} chelating residues in the deaminase domain are denoted by white stars (Kim et al., 1994; Lai et al., 1995; Melcher et al., 1996a). Alternative splicing of exon 5a results in ADAR2 protein isoforms containing an additional 40 (human) or 10 (rat or mouse) a.a. between the second and third zinc coordination residues of the deaminase domain. ADAR exon boundaries are denoted by black triangles.

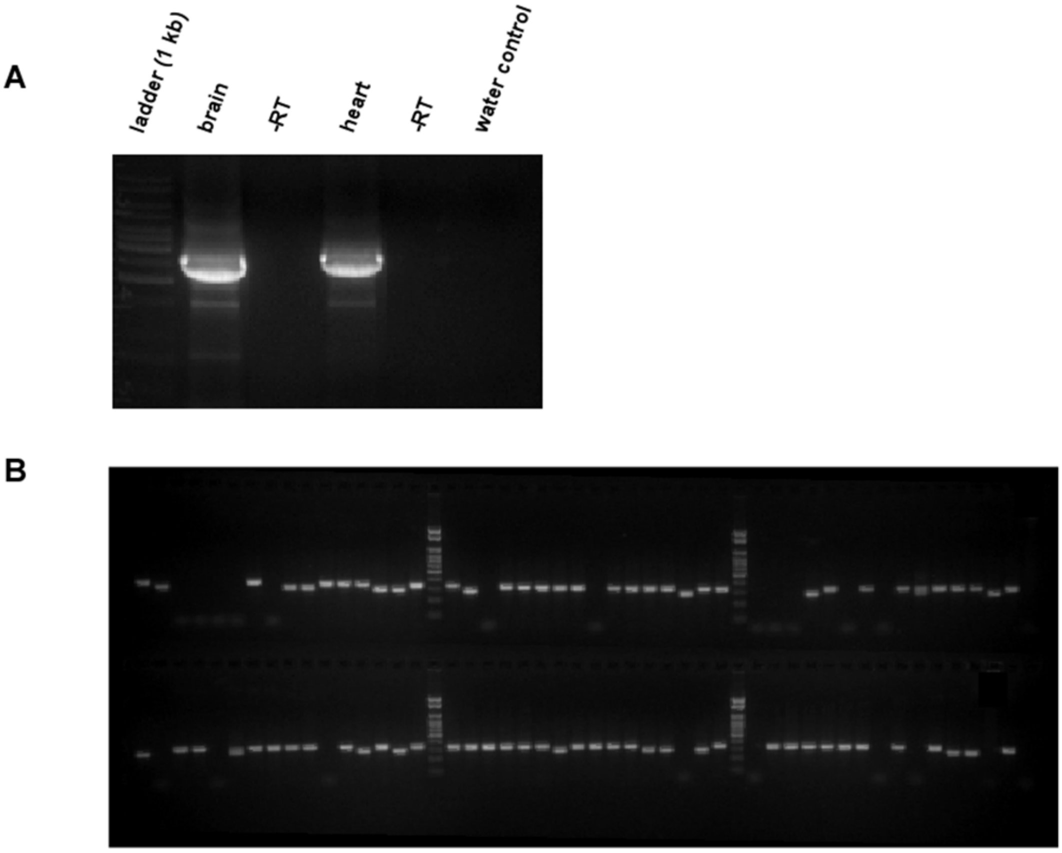

Figure 3.6 Full length cloning and colony screening of ADAR2 from rat brain and rat heart. *A*, Exemplar PCR products (~2.4 kb) from full length RT-PCR analysis of ADAR2 in rat brain and rat heart. *B*, Exemplar PCR products from the colony screening of 96 clones transformed with RT-PCR product ligated into pGEM®-T Easy vector. Approximately 50 bacteria clones each from rat brain and rat heart were amplified, purified and sent for DNA sequencing analysis.

Table 3.3 Summary of mutations and alternative splicing in full length ADAR2 clones extracted from rat brain and heart. Sequences are compared against rat ADAR2 clone (GenBank Accession number: U43534). Mutations in cDNA sequences and the relative nucleotide position in rat ADAR2 clone is indicated (top), together with the resultant amino acid change and the relative amino acid position in rat ADAR2 clone (bottom). Alternative splicing at position -1 of intron 1 is indicated by $\text{ADAR2}_{+47\text{nt}}$ while alternative splicing of exon 5a is indicated by $\text{ADAR2}_{5\text{a}+}$. Approximately 50 clones from rat brain and heart are sequenced and analysed, and the frequencies of mutation and splicing are summarized in table.

	Rat brain	**Rat heart**
Consistent mutations		
T → C (160)	100%	100%
I > T (14)	(53/53)	(59/59)
T → G (221)	100%	100%
No amino acid change	(53/53)	(59/59)
A → G (1310)	0%	8.5%
I > V (397)	(0/53)	(5/59)
Alternative splicing		
$\text{ADAR2}_{+47\text{nt}}$	79.2%	34.7%
	(57/72)	(26/75)
$\text{ADAR2}_{5\text{a}+}$	36.1%	18.7%
	(26/72)	(14/75)

Glucose metabolic regulation of RNA editing of $Ca_V1.3$ in insulinoma cells

In the pancreatic β-cells, glucose metabolism causes an increase in ATP or the ATP/ADP ratio, which in turn closes K_{ATP} channels, leading to membrane depolarization, opening of L-type calcium channels, influx of Ca^{2+}, and a rise in cytosolic free Ca^{2+} concentration which directly triggers insulin exocytosis. Studies of $Ca_V1.3^{-/-}$ knockout mice indicate that $Ca_V1.3$ channels are required for proper generation of β-cells in the postnatal pancreas (Namkung et al., 2001), and in pancreatic insulinoma cell line INS-1, the channels are preferentially coupled to glucose-stimulated insulin secretion (Liu et al., 2003a). In addition, expression levels of ADAR2, GluR-B editing and ADAR2 self-editing in INS-1 cells were markedly augmented in response to glucose at the physiological concentration for insulin secretion stimulation (Gan et al., 2006). Hence, RNA editing by ADAR2 in insulinoma cells was metabolically regulated by nutritional and energy status, suggesting that A-to-I RNA editing is involved in modulation of β-cell function.

Given the fact that glucose serves as the most potent physiological stimulus of pancreatic islets and β-cells function, and could metabolically regulate ADAR2-mediated RNA editing, we investigated the effects of glucose on RNA editing of $Ca_V1.3$ mRNA. Briefly, rat insulinoma cell line INS-1e cells were pre-cultured in 2.8 mM glucose for 24 h, followed by incubation in media with 16.7 mM glucose for 3 – 48 h. Cell morphology of INS-1 cells remain consistent despite altered glucose content from normal DMEM media (11.1 mM glucose) (Fig 3.7A). $Ca_V1.3$ remained unedited at all three loci (Fig 3.7B) despite exposure to glucose at physiological concentration for insulin secretion stimulation, which progressively augment R > G site editing of the GluR-2 pre-mRNA (from 15.6 to 47.9% at 48 h) (Fig 3.8A) and ADAR2 self-editing and alternative splicing at intron 1 (from 22.2 to 45.5% at 48 h)

(Fig 3.8B). Hence, while glucose could metabolically regulate RNA editing, $Ca_V1.3$ was unaffected due to unknown factors. In addition, similar stimulation effect of glucose on the ADAR2 self-editing and R > G site of GluR-B pre-mRNA editing was also observed in mouse insulinoma cell line MIN6 (data not shown), while $Ca_V1.3$ mRNA remained unedited.

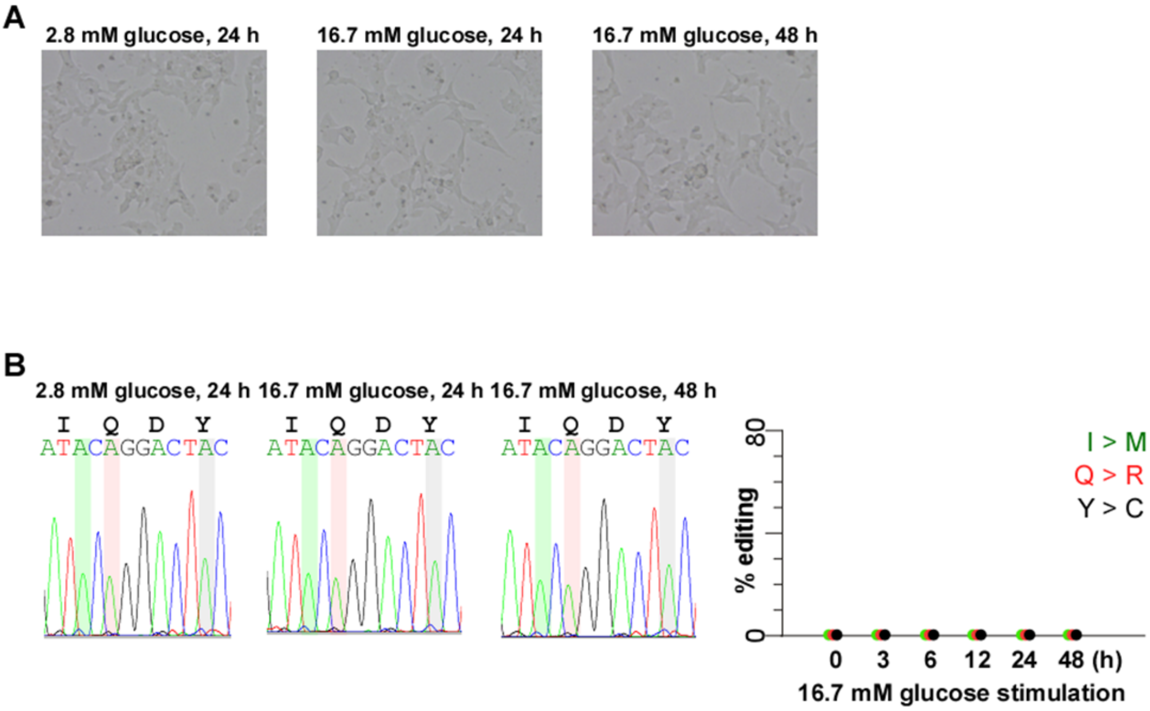

Figure 3.7 No RNA editing of $Ca_V1.3$ IQ motif with glucose stimulation. *A*, No morphological changes in rat insulinoma cells, INS-1e that were pre-cultured at 2.8 mM glucose and stimulated for up to 48 h at 16.7 mM glucose. *B*, No RNA editing of $Ca_V1.3$ IQ motif in INS-1e with glucose stimulation. Left panel, direct DNA sequencing of RT-PCR products from INS-1e cells exposed to glucose stimulation. Right panel, percent editing at three locations (I > M, Q > R and Y > C), as calculated by measuring electropherograms heights for adenosine versus guanosine. *Error bars* reflect S.E.M. ($n = 3$).

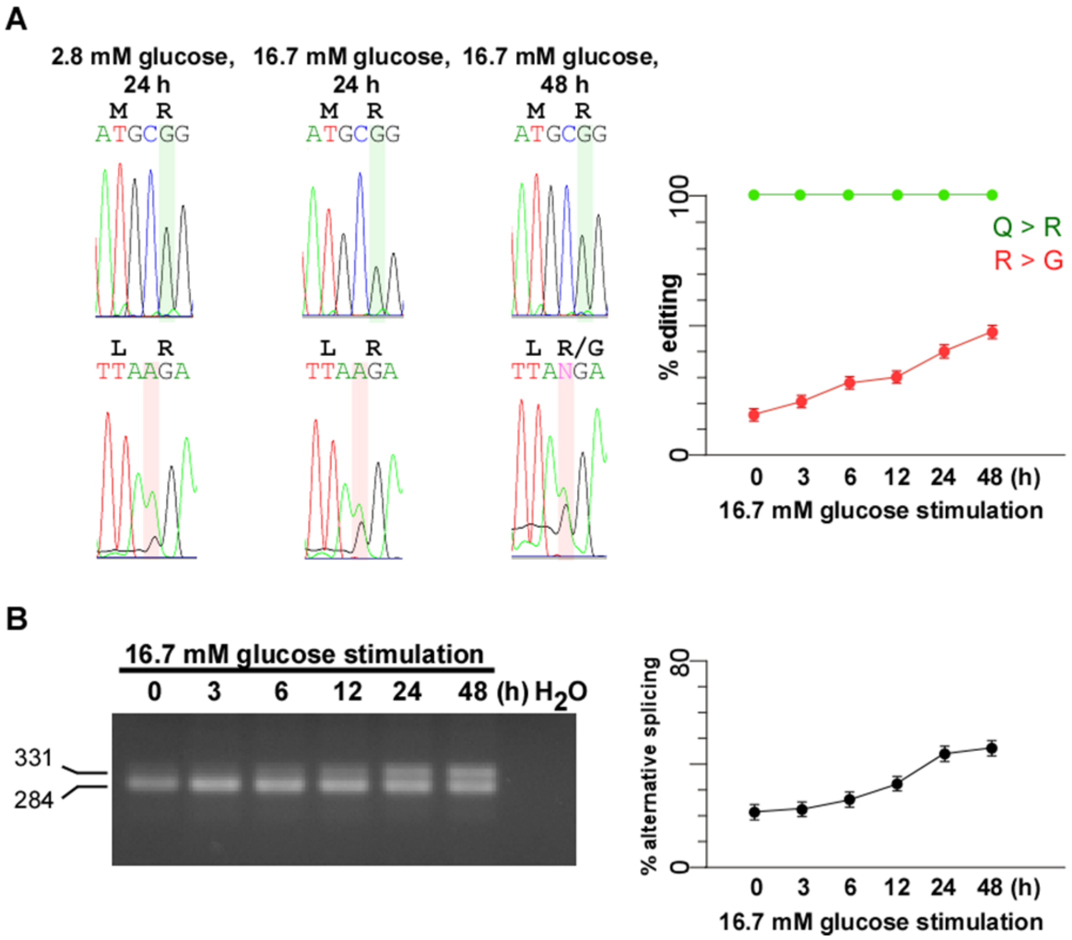

Figure 3.8 Increased RNA editing activity with glucose stimulation. *A*, Increased RNA editing of GluR-B at R > G location in INS-1e cells with glucose stimulation. Left panel, direct DNA sequencing of RT-PCR products from INS-1e cells exposed to glucose stimulation. Right panel, percent editing at two locations (Q > R and R > G), as calculated by measuring electropherograms heights for adenosine versus guanosine. *Error bars* reflect S.E.M. (*n* = 3). *B*, Increased in ADAR2 deaminase activity in INS-1e with glucose stimulation. Left panel, exemplar PCR products (284 bp and 331 bp) from RT-PCR analysis of INS-1e cells with glucose stimulation. Data are representative of three independent experiments. Right panel, percent alternative splicing at intron 1 – exon 2 boundary, as calculated by measuring peak area for 331 bp versus 284 bp. *Error bars* reflect S.E.M. (*n* = 3).

Differentiation of neuroblastoma cell lines and RNA editing of $Ca_V1.3$

Editing of $Ca_V1.3$ in the three adenosine sites of IQ motif appears to be regulated during the development of the brain, similar to that of $K_V1.1$ at the I > V site and GluR-B at the R > G site (Fig 3.1 – 3.2). It is currently not known whether there is a specific mechanism during brain development and neuron differentiation for the activation of RNA editing machinery, especially in conjunction with subcellular localization of ADAR2. Several neuroblastoma cell lines were examined under undifferentiated conditions for RNA editing activity, and $Ca_V1.3$ were found to be unedited in mouse neuroblastoma cell lines N1E-115 and Neuro2A, human neuroblastoma cell line SH-SY5Y, and even mouse neuroblastoma/ rat glioblastoma cell line NG105-15, despite detection of GluR-B Q > R pre-mRNA editing as well as splicing of ADAR2 at intron 1 (Fig 3.9 – 3.10).

Neuronal differentiation of mouse neuroblastoma N1E-115 cells was induced with serum deprivation and retinoic acid (RA) treatment. Undifferentiated N1E-115 cells (Fig 3.9A, left panel) were grown in 10% FBS, and neurite formation started to form after 24 h in the differentiation media (Fig 3.9A, middle panel) and differentiation was complete by day 14 as observed from the neuronal network consisting of dendritic outgrowth (Fig 3.9A, right panel). However, $Ca_V1.3$ remained unedited at all three adenosine sites even after 14 days in differentiation media (Fig 3.9B) while editing of GluR-B at R > G location, and self-editing of ADAR2 and hence splicing at intron 1 were moderately elevated (Fig 3.10). Increase in percent editing of $K_V1.1$ at I > V location was not significant (Fig 3.9C).

Unlike ADAR1, activity of ADAR2 proteins was restricted to the nucleus due to the single NLS in its N-terminal domain, and that while ADAR2 were transiently sequestered into the nucleolus, enhanced translocation of ADAR2 into the nucleoplasm could be correlated with increased editing efficacy (Desterro et al., 2003; Sansam et al., 2003). Hence, we examined the subcellular localization of ADAR2 proteins in N1E-115 cells upon differentiation, and observed anti-ADAR2 staining only in the nucleus of N1E-115 cells. Staining was most intense in the nucleolus in undifferentiated and differentiated N1E-115 cells, though there appeared to be more diffusion of ADAR2 into nucleoplasm in differentiated cells (Fig 3.10C).

Despite the increased catalytic activity and diffusion of ADAR2 into nucleoplasm with neuronal differentiation, it was not sufficient to edit $Ca_V1.3$ pre-mRNA.

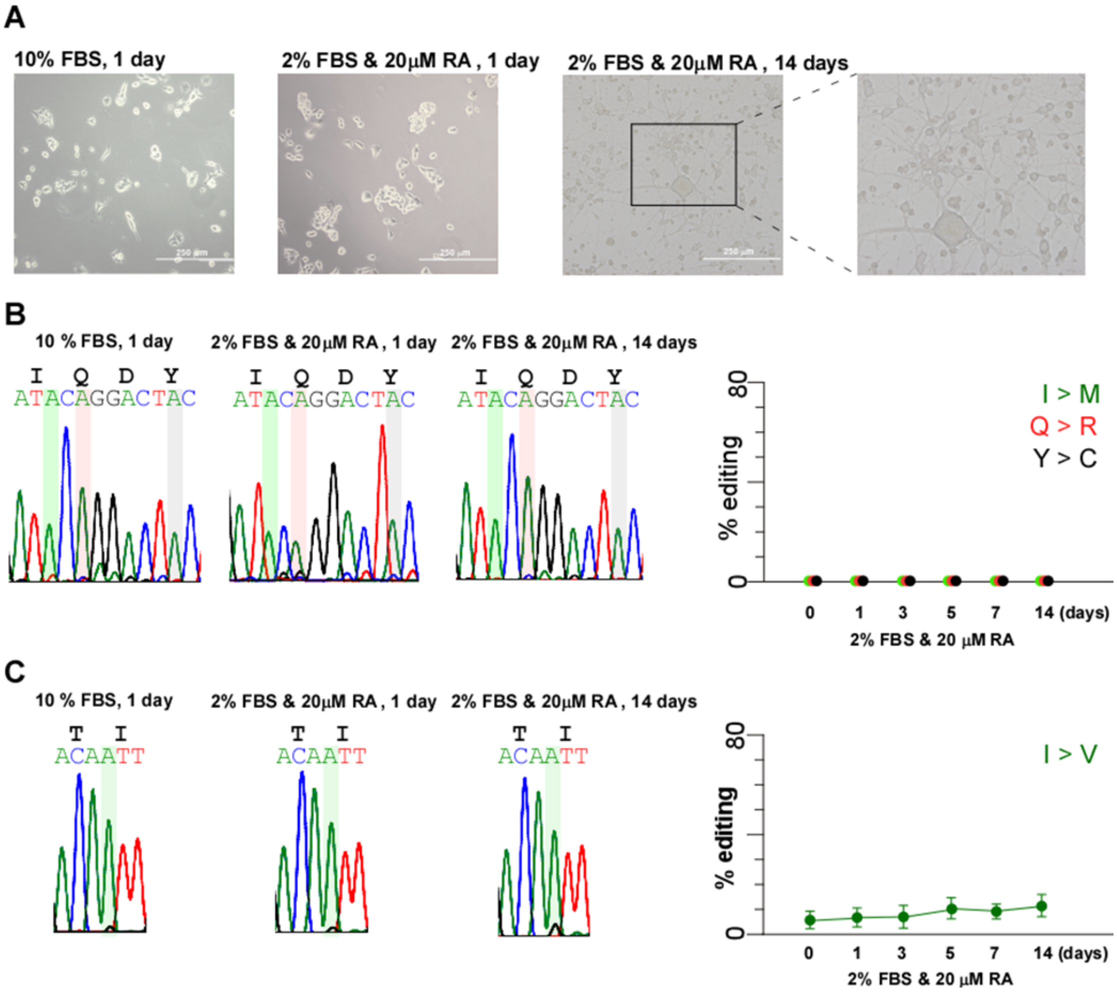

Figure 3.9 No RNA editing of $\mathrm{Ca_V}$1.3 IQ motif with prolonged differentiation of neuroblastoma cells. *A*, Undifferentiated N1E-115 neuroblastoma cells in normal 10% serum (leftmost), and turn into a neuronal network consisting of dendritic outgrowth with prolonged exposure to differentiating media containing 2% FBS and 20 μM RA (middle and rightmost, light microscopy x10). *B*, No RNA editing of $\mathrm{Ca_V}$1.3 IQ motif in N1E-115 cells with differentiation. Left panel, direct DNA sequencing of RT-PCR products from N1E-115 cells exposed to differentiating media. Right panel, percent editing at three locations (I > M, Q > R and Y > C), as calculated by measuring electropherograms heights for adenosine versus guanosine. *Error bars* reflect S.E.M. ($n = 3$). *C*, A modest increase in RNA editing of $\mathrm{K_V}$1.1 at I > V location in N1E-115 cells with differentiation. Left panel, direct sequencing of RT-PCR products from N1E-115 cells exposed to differentiating media. Right panel, percent editing at location I > V, as calculated by measuring electropherograms heights for adenosine versus guanosine. Error bars reflect S.E.M. ($n = 3$).

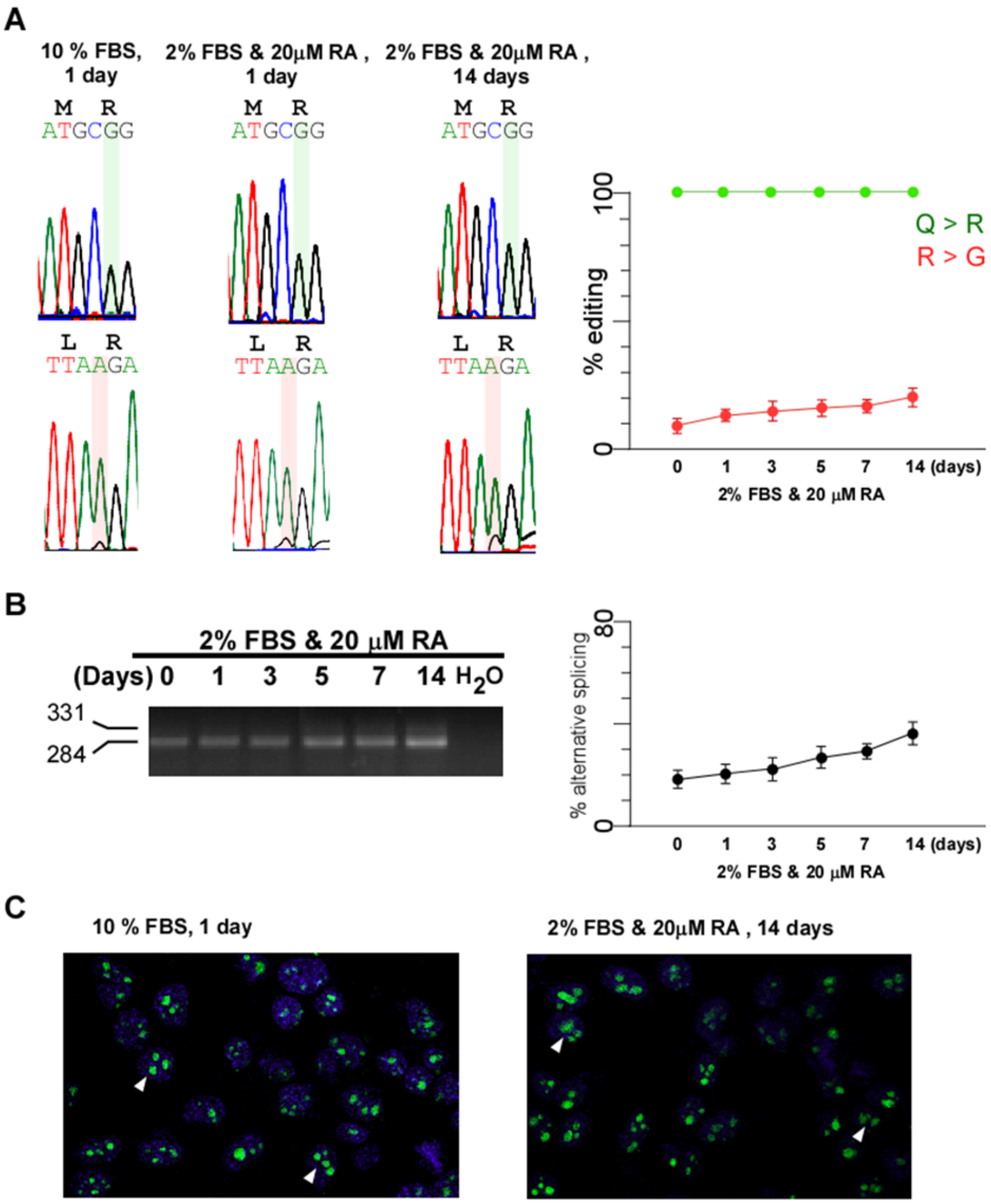

Figure 3.10 Increase in RNA editing activity with prolonged differentiation of neuroblastoma cells. *A*, Increased RNA editing of GluR-B at R > G location in N1E-115 cells with differentiation. Left panel, direct DNA sequencing of RT-PCR products from N1E-115 cells exposed to differentiating media. Right panel, percent editing at two locations (Q > R and R > G), as calculated by measuring electropherograms heights for adenosine versus guanosine. *Error bars* reflect S.E.M. (n = 3). *B*, Increased in ADAR2 deaminase activity in N1E-115 cells with differentiation. Left panel, exemplar PCR products (284 bp and 331 bp) from RT-PCR analysis of INS-1e cells with glucose stimulation. Data are representative of three independent experiments. Right panel, percent alternative splicing at intron 1 – exon 2 boundary, as calculated by measuring peak area for 331 bp versus 284 bp. *Error bars* reflect S.E.M. (n = 3). *C*, N1E-115 cells were assayed for ADAR2 localization by indirect immunofluorescence using anti-ADAR2 antibodies. The anti-ADAR2 antibody (green) stained the nucleoli in both undifferentiated (left panel) and differentiated (right panel) N1E-115 cells. Staining in differentiated cells appeared to be more diffused, with minor staining in nucleoplasm (white arrows). DAPI stained the nuclei.

Co-factors of ADAR2 and RNA editing of $Ca_V1.3$

The crystal structure of the catalytic domain of human ADAR2 reveals that several key conserved amino acids (Lai et al., 1995) were involved in the coordination of a zinc atom and the formation of the catalytic center (Macbeth et al., 2005). Hence, zinc is a crucial co-factor for deaminase function of ADAR2. Several studies have shown that zinc transport is a time-, concentration-, pH-, and temperature-dependent process, although there appear to be both saturable and non-saturable components (Reyes, 1996). Alteration of the pH of culture media for insulinoma cell MIN6 did not cause RNA editing of $Ca_V1.3$ (Fig 3.11B) but the increase in pH led to a slight decrease in both editing of GluR-B at the R > G location (pH 6.4: 23.36 ± 1.88%; pH 7.25: 21.69 ± 1.38%; pH 8.05: 21.10 ± 2.68%) and self-editing of ADAR2 (Fig 3.12). Exposure of cells to additional 10 μM zinc chloride for 24 h also did not result in $Ca_V1.3$ editing, although the additional zinc caused a modest increase in editing of GluR-B at the R > G location (pH 6.4: 23.86 ± 2.16%; pH 7.25: 23.12 ± 1.04%; pH 8.05: 22.82 ± 2.57%) and self-editing at all three pH tested (Fig. 3.12). A similar trend is observed in both mouse neuroblastoma N1E-115 and Neuro2A cells and rat insulinoma INS-1e cells.

Interestingly, from the crystal ADAR2 structure, an inositol hexakisphoshate (IP_6) moiety was discovered buried within the enzyme core and likely stabilized the multiple arginine and lysine residues present in the catalytic pocket. IP_6 was thought to play a critical role during the hydrolytic deamination reaction due to its close proximity to the catalytic center (Macbeth et al., 2005). The last step in the synthesis of IP_6 is the phosphorylation of inositol pentakisphosphate (IP_5) by inositol 1,3,4,5,6-pentakisphospahte 2-kinase (IPPK) (Fig 3.13A). Relative expression of IPPK in the various mouse tissues and cell lines were measured by RT-PCR analysis of mRNA and compared against that of housekeeping gene β-actin (Fig 3.13B). In mouse brain, heart and β-islets, the expression levels of IPPK was relatively constant, and similar expression levels were observed in both the mouse and human neuroblastoma cells N1E-115 and SH-SY5Y as well as mouse insulinoma cells MIN6. Furthermore, colony screening and sequencing analysis of full length IPPK cloned from mouse brain and heart cDNA showed sequence similarity with published sequences (GenBank Accession No: NM_199056). The *ippk* gene consist of 13 exons, and protein translation initiates 75 nt into exon 1 (Fig3.13C). In both the mouse brain and heart clones, alternative splicing of ippk mRNA was not observed at the N-termini, possibly due to sitting of primers at the initiator methionine site, nor in the C-termini.

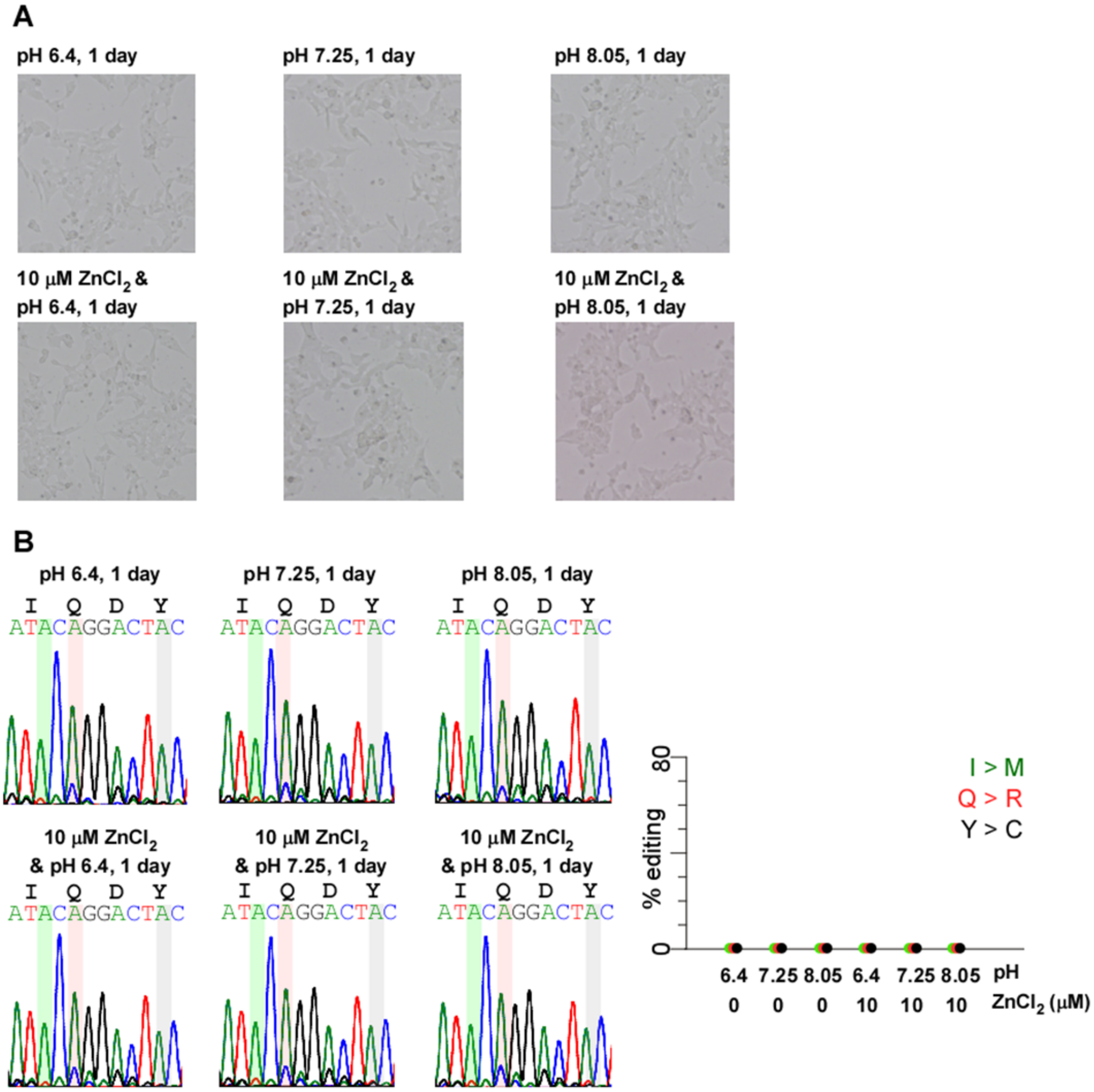

Figure 3.11 No RNA editing of Ca$_V$1.3 IQ motif with exposure to zinc at different pH. *A*, No morphological changes in mouse insulinoma MIN6 cells with exposure to media culture buffered at different pH and 10 μM zinc chloride for 24 h. *B*, No RNA editing of Ca$_V$1.3 IQ motif in MIN6 cells cultured in media buffered at different pH and 10 μM zinc chloride. Left panel, direct DNA sequencing of RT-PCR products from MIN6 cells exposed to different pH and 10 μM zinc chloride. Right panel, percent editing at three locations (I > M, Q > R and Y > C), as calculated by measuring electropherograms heights for adenosine versus guanosine. *Error bars* reflect S.E.M. ($n = 3$).

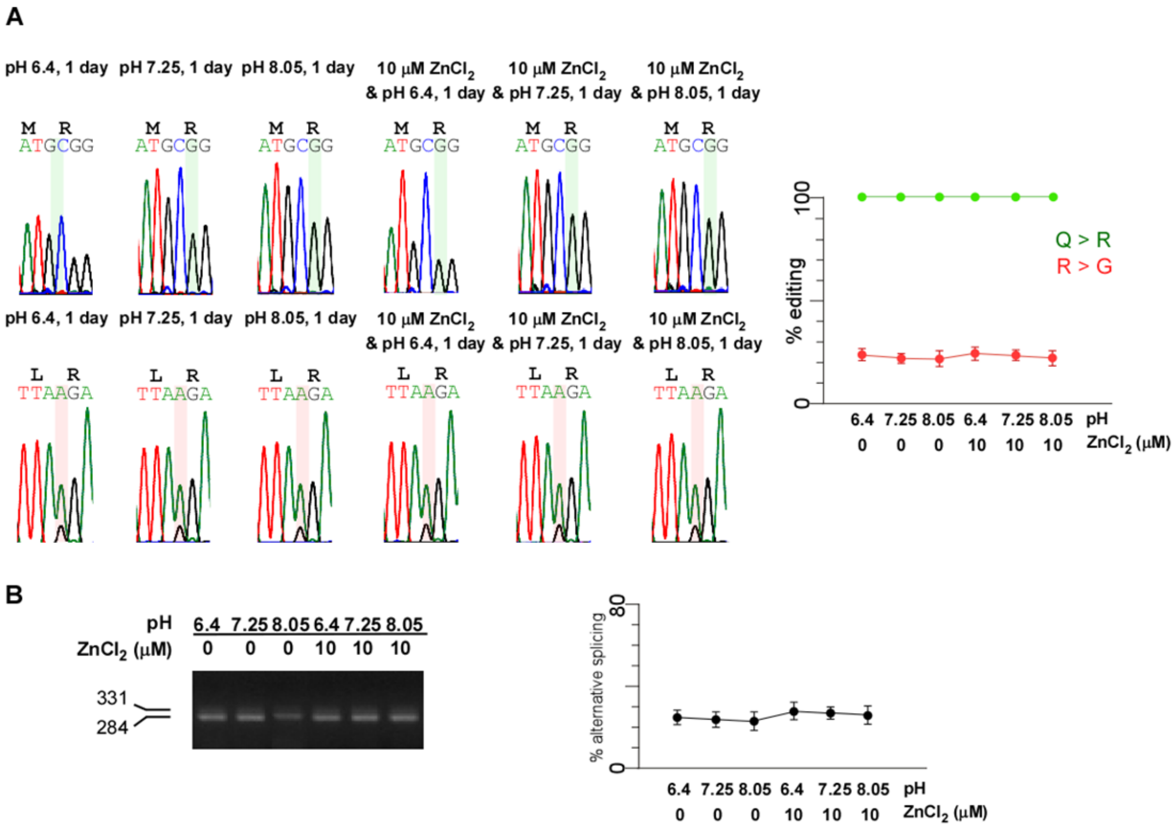

Figure 3.12 No change in RNA editing activity with exposure to zinc at different pH. *A*, No change in RNA editing of GluR-B in mouse insulinoma MIN6 cells with exposure to media culture buffered at different pH and 10 µM zinc chloride for 24 h. Left panel, direct DNA sequencing of RT-PCR products from MIN6 cells cultured in media buffered at different pH and 10 µM zinc chloride. Right panel, percent editing at two locations (Q > R and R > G), as calculated by measuring electropherograms heights for adenosine versus guanosine. *Error bars* reflect S.E.M. (*n* = 3). *B*, Increased in ADAR2 deaminase activity in INS-1e with glucose stimulation. Left panel, exemplar PCR products (284 bp and 331 bp) from RT-PCR analysis of MIN6 cells cultured in media buffered at different pH and 10 µM zinc chloride. Data are representative of three independent experiments. Right panel, percent alternative splicing at intron 1 – exon 2 boundary, as calculated by measuring peak area for 331 bp versus 284 bp. *Error bars* reflect S.E.M. (*n* = 3).

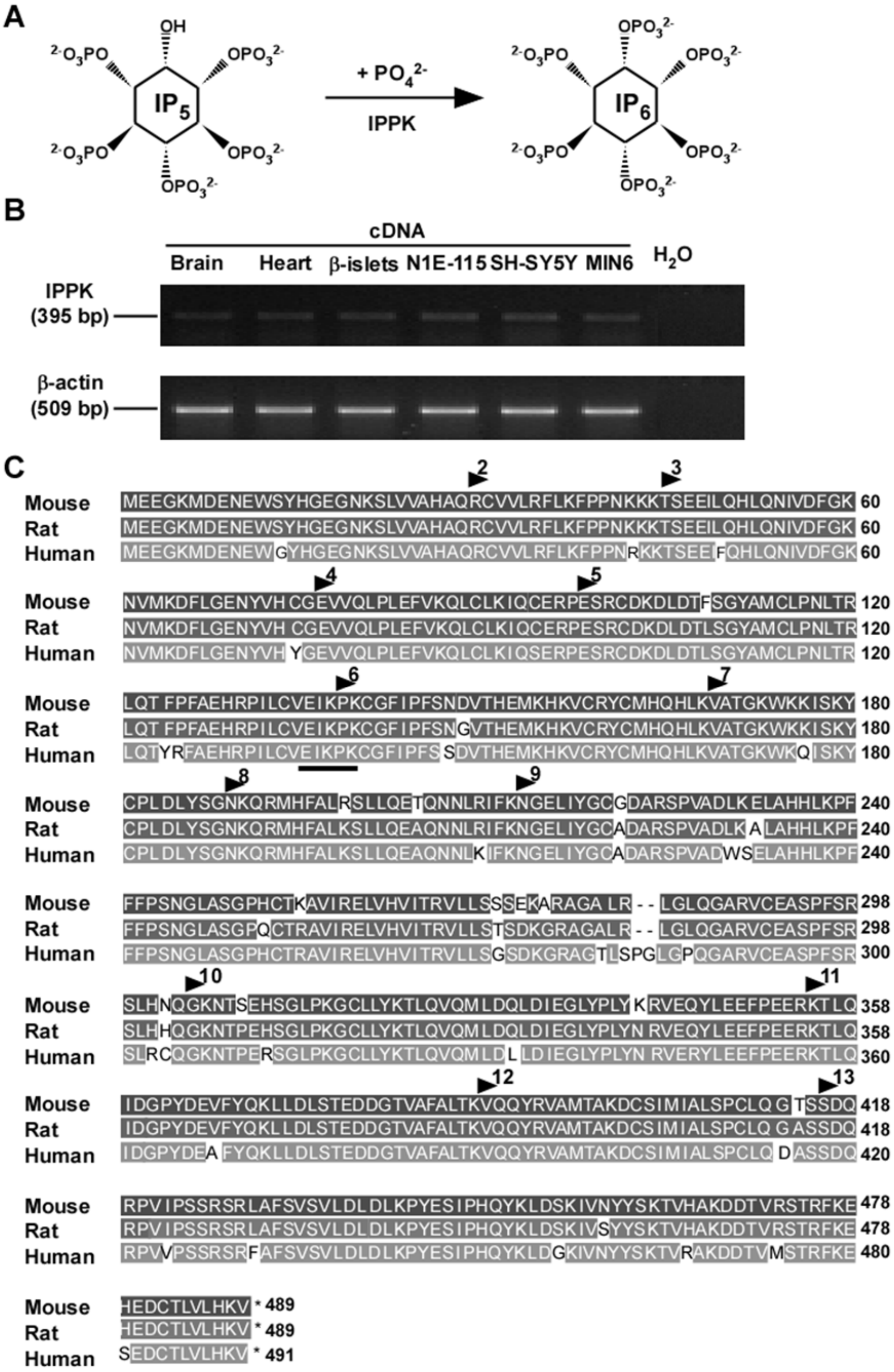

Figure 3.13 No difference in sequence and mRNA expression levels of IPPK in various tissues and cell lines. *A*. Diagram depicts phosphorylation site in inositol 1,3,4,5,6-pentakisphosphate (IP_5) that is acted upon by enzyme inositol 1,3,4,5,6-pentakisphospahte 2-kinase (IPPK), forming inositol 1,2,3,4,5,6-hexakisphosphate (IP_6). *B*. Exemplar PCR products (IPPK: 395 bp and β-actin: 509 bp) from RT-PCR analysis of mouse brain, heart and β-islet mRNA, neuroblastoma cell lines N1E-115 and SH-SY5Y, and insulinoma cell line INS-1e. *C*. Alignment of mouse, rat and human IPPK amino acid sequences. Amino acid sequences are according to GenBank Accession Numbers: mouse IPPK: NP_951011, rat IPPK: NP_001008556, and human IPPK: NP_073592. Grey-shaded areas indicate regions of sequence homology. ADAR exon boundaries are denoted by black triangles. The underlined motif EXKPK is conserved in inositol-pentakisphosphate 2-kinases of both family 1 and 2.

Overexpression of ADAR2 in insulinoma MIN6 cells

Immunoblot analysis of nuclear extracts from MIN6 cells showed a low expression level of endogenous ADAR2, which was increased with transfection of pRK5-ADAR2 (Fig 3.14A). Protein levels in MIN6 cells increased linearly with the amount of ADAR2 transfected. Transfected ADAR2 showed a predominantly nuclear expression, concentrated mainly in the nucleoli (Fig 3.14B, green staining). Despite the increase in self-editing of ADAR2 and editing of GluR-B at the R > G location with ADAR2 transfection (Fig 3.14D-E), $Ca_V1.3$ remained unedited (Fig 3.14C).

In vivo, A-to-I editing has been categorized into two types – hyper-editing of multiple adenosines and site-selective editing of adenosines in the imperfect double-stranded RNA duplexes that are formed via base-pairing between the edited site and editing-site complementary site (ECS). The ECS is usually located in the neighbouring introns. The putative ECS of mouse $Ca_V1.3$ was predicted via analysis of the genomic sequences and predicted RNA structures using Mfold software. The RNA duplex structure (Fig 3.15A) is conserved in human and rat (data not shown). The pRK5-gIQECS construct was generated by a colleague. A ~4.9 kb sequence, consisting of the edited site in exon 41 and ~4.49 kb of upstream intron with the 58 bp intronic ECS 3792 bp upstream of the first edited adenosine, was synthesized by overlapping PCR and subcloned into the pRK5 vector (Fig 3.15A). In MIN6 cells, co-expression of pRK5-gIQECS with either ADAR1 or ADAR2 family caused editing of adenosines at the I > M and Y > C loci, but not so in expression of pRK5-gIQECS alone or with just ADAR3 (Fig 3.15B). Indeed, percent editing at these two sites (I > M: 81.94 ± 2.56%; Y > C: 84.44 ± 1.78%) exceeded that in adult mouse brain (Fig 2.5A). This data suggests that both the secondary structure of RNA substrate and expression levels of ADAR is crucial for RNA editing of $Ca_V1.3$ at the IQ motif.

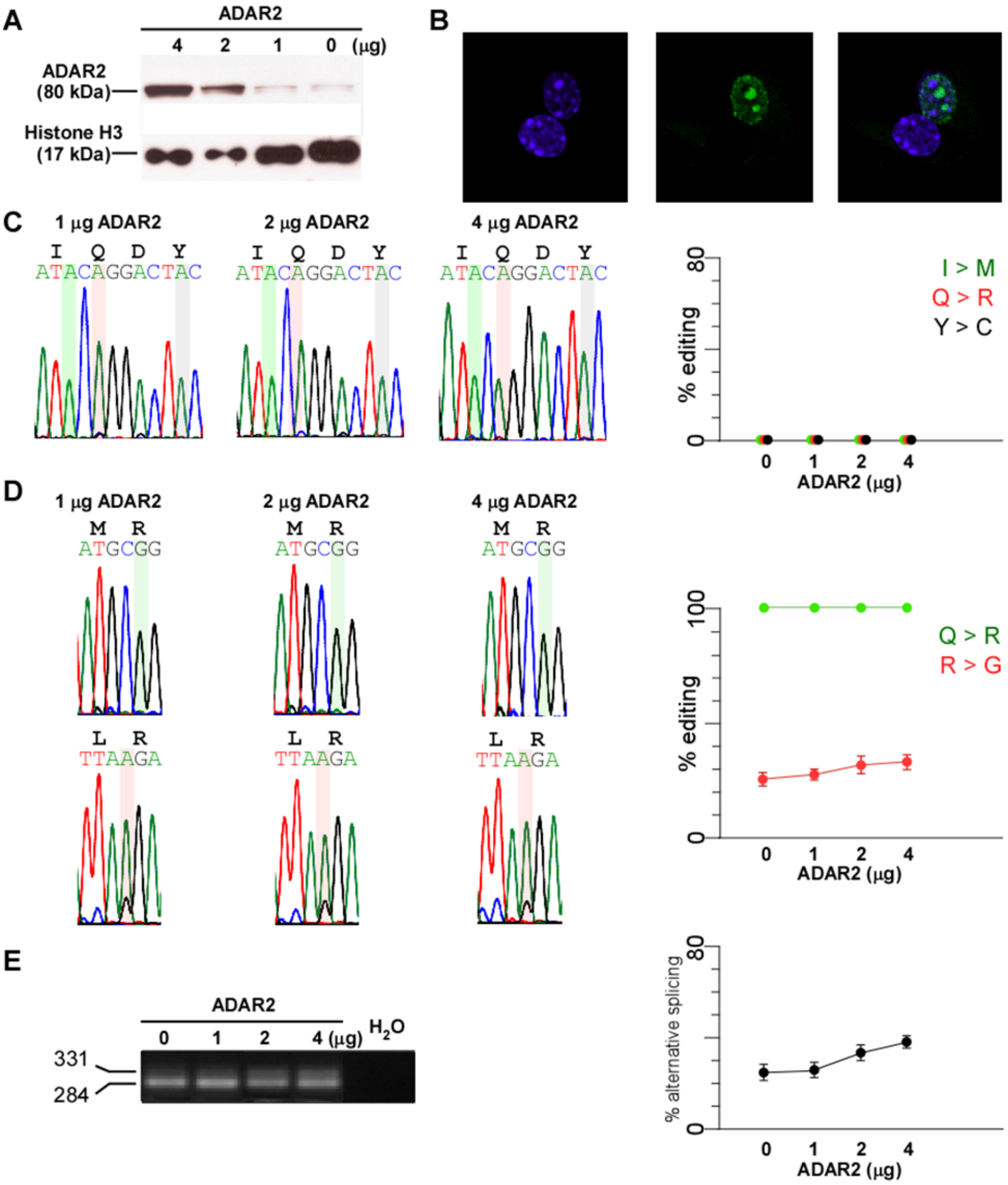

Figure 3.14 No RNA editing of Ca$_V$1.3 at IQ motif with overexpression of ADAR2 in MIN6 cells. *A*, Increase in ADAR2 protein expression in MIN6 cells with ADAR2 transfection. *Top*, Immunoblots of nuclear extracts from MIN6 cells transfected with different among of ADAR2 (0, 1, 2 and 4 µg) probed with anti-ADAR2 antibody. *Bottom*, same as top, but probed with anti-histone H3 antibody (loading control). *B*, MIN6 cells were assayed localization of transfected ADAR2 by indirect immunofluorescence using anti-FLAG antibody (green). DAPI stained the nucleus. *C*, No RNA editing of Ca$_V$1.3 IQ motif in MIN6 cells cultured in media buffered at different pH and 10 µM zinc chloride. *Left panel*, direct DNA sequencing of RT-PCR products from MIN6 cells transfected with ADAR2. *Right panel*, percent editing at three locations (I > M, Q > R and Y > C), as calculated by measuring electropherograms heights for adenosine versus guanosine. *Error bars* reflect S.E.M. ($n = 3$). *D*, Modest increase in RNA editing of GluR-B with overexpression of ADAR2 in MIN6 cells. *Left panel*, direct DNA sequencing of RT-PCR products from MIN6 cells transfected with ADAR2. *Right panel*, percent editing at two locations (Q > R and R > G), as calculated by measuring electropherograms heights for adenosine versus guanosine. *Error bars* reflect S.E.M. ($n = 3$). *E*, Increase in ADAR2 deaminase activity in MIIN6 cells with overexpression of ADAR2. Left panel, exemplar PCR products (284 bp and 331 bp) from RT-PCR analysis of MIN6 cells transfected with ADAR2. Data are representative of three independent experiments. Right panel, percent alternative splicing at intron 1 – exon 2 boundary, as calculated by measuring peak area for 331 bp versus 284 bp. *Error bars* reflect S.E.M. ($n = 3$).

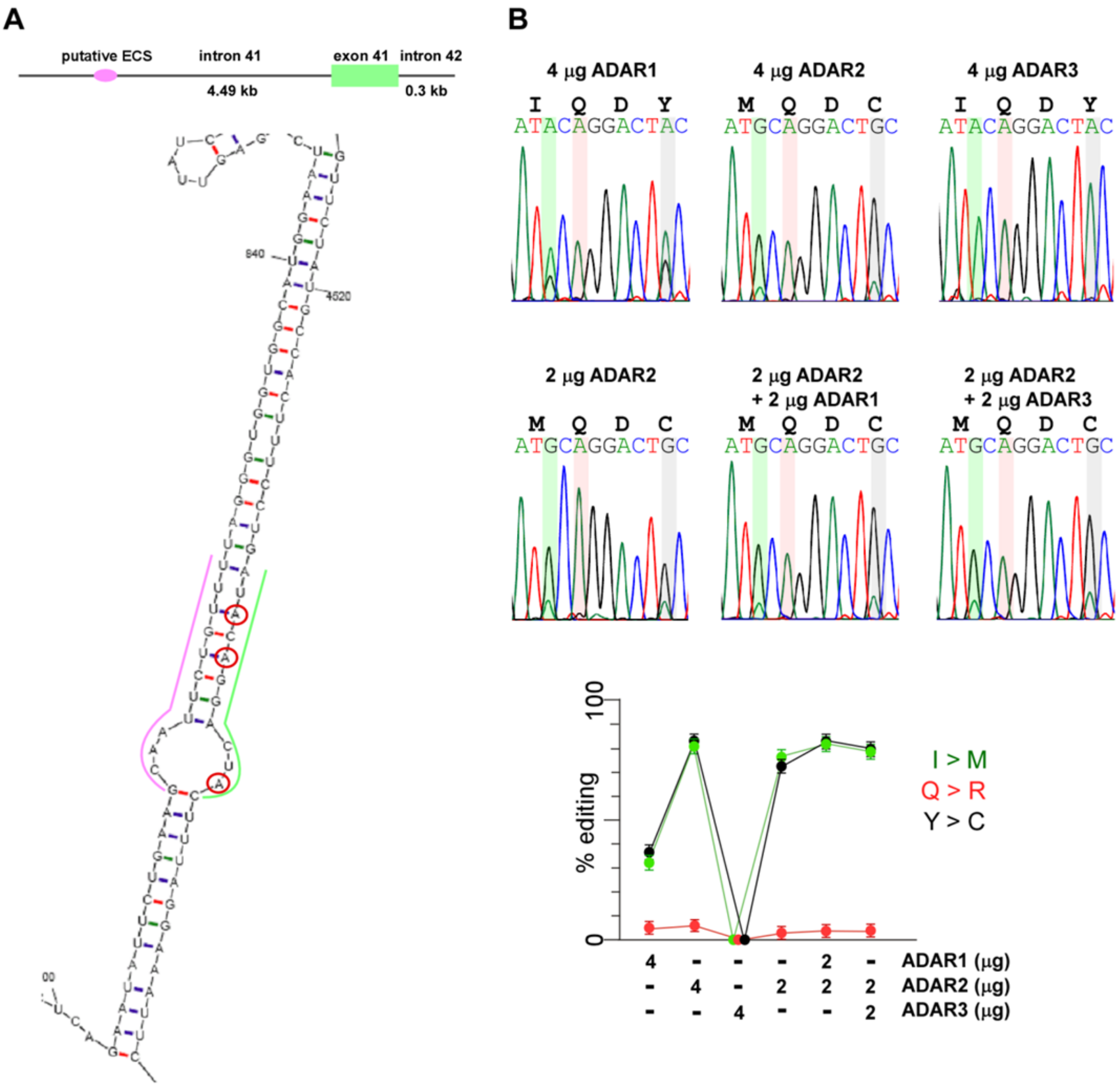

Figure 3.15 Minigene construct gIQECS is edited by both ADAR1 and ADAR2 in MIN6 cells. *A*, Minigene construct named pRK5-gIQECS was generated by subcloning a 4952 bp mouse genomic Ca_V1.3 sequence spanning the putative editing-site complementary sequence (ECS), intermediate intronic sequence and edited exon 41 into pRK5 vector. *Top*, Diagram shows the sequence of mouse Ca_V1.3 consisting of the exon 41(green box) and upstream intron of ~4 kb and the predicted location of editing site complementary sequence (ECS) (pink circle) (GenBank Accession No: NT_039606). *Bottom*, Diagram of double-stranded structure formed between a 58 bp intronic sequence, 3792 bp upstream of the first edited site in mouse RNA. Output is derived by input of gIQECS sequence into Mfold webserver (http://mfold.bioinfo.rpi.edu/cgi-bin/rna-form1.cgi), using default setting. The intronic ECS is denoted by a pink line and exonic IQ motif by a green line, and the edited adenosines are highlighted in red. *B*, Editing of IQ motif in pRK5-gIQECS occurs together with overexpression of ADAR1 and ADAR2 in MIN6 cells, but not with ADAR3. *Top*, direct DNA sequencing of RT-PCR products from MIN6 cells transfected with pRK5-gIQECS and ADAR family members (ADAR1-3). *Bottom*, percent editing at three locations (I > M, Q > R and Y > C), as calculated by measuring electropherograms heights for adenosine versus guanosine. *Error bars* reflect S.E.M. ($n = 3$).

3.4 Discussion and Conclusion

Beside the IQ motif of $Ca_V1.3$ mRNA, editing of most selectively edited substrates is regulated during development, showing a non-linear increase with age. The editing of recoding targets is under tight control, and the deregulation of RNA editing in space and/or time is correlated with various human disease phenotypes (Niswender et al., 2001; Gurevich et al., 2002; Paz et al., 2007; Cenci et al., 2008). The specific molecular mechanisms that govern intracellular RNA editing levels remain largely unknown, and in this study, we aimed to isolate and identify factors that control developmental and CNS-specific editing of $Ca_V1.3$ at the IQ motif.

Despite the ubiquitous expression of ADAR2, the presence of ADAR2 mRNA rarely correlates with the observed intracellular RNA editing activity. However, ADAR2 expression and localization studies in conjunction with developmental and cell-type specific modulation of RNA editing have demonstrated multiple and complex patterns of regulation on the transcriptional, post-transcriptional, translational and post-translational levels (Nishikura, 2010). ADAR2 proteins are expressed in several alternative splice forms that differ with respect to their enzymatic activity. In our studies, we observed higher ADAR2 catalytic activity in developing brains that could partially explain for the increase in $Ca_V1.3$ RNA editing. In addition, percent splicing of ADAR2 in intron 1 and exon 5a is more frequent in rat brain and is equated with greater ADAR2 deaminase activity.

Nuclear RNA editing activity of ADAR2 can be regulated through the controlled nuclear import of the proteins. Within the nucleus, ADAR2 proteins are shuttled between the nucleoli and nucleoplasm, which could further regulate its editing activity. Immunoblot and immunofluorescence analysis of ADAR2 show nuclear localization in the various cell lines examined, predominantly in the nucleoli. However, this appears to be insufficient for RNA editing of $Ca_V1.3$ at the IQ motif.

Although ADAR2 seem to be fully functional without the requirement of essential cofactors, the sitting of zinc atom and IP_6 at its catalytic center may be essential for structural stability and deaminase activity. Modulation of zinc availability in the cell lines at different pH did not affect RNA editing of $Ca_V1.3$, though the additional 10 μM zinc modestly increased ADAR2 editing activity. Despite the isoleucine to valine change observed in ~8% of heart ADAR2 coding mRNA near the first zinc coordination residue, both amino acids have similar biophysical properties and the catalytic center of translated ADAR2 should be functional. In the rat brain and heart, the expression levels and splice combination of ippk were similar and hence, IP_6 is similarly expressed. Hence it appears that cofactors of ADAR2 are adequately expressed, and not responsible for CNS-specific editing of $Ca_V1.3$.

In this study, we have also eliminated glucose metabolism and neural differentiation, as well as expression of ADAR family members as modulators of $Ca_V1.3$ RNA editing in the cell lines. Although increased glucose metabolism, prolonged neural differentiation and elevated ADAR2 expression could augment self-editing of ADAR2 pre-mRNA as well as editing levels of other ADAR2 substrates, the IQ motif in $Ca_V1.3$ remains unedited.

In light of the editing of gIQECS at two adenosine sites in conjunction with ADAR1 and ADAR2 overexpression, it appears that the dsRNA structure formed by intronic ECS and exon 41 of $Ca_V1.3$ is sufficient for site-specific RNA editing. Furthermore, it appears that the endogenous ADAR2 expressed in the cell lines alone is inadequate. C/D small nucleolar RNA might play a role in regulating RNA editing, as shown by the identification of a brain-specific small RNA, MBII-52 that specifically decreases the efficiency of ADAR2 editing at the C-site within 5-HT$_{2C}$ pre-mRNA (Vitali et al., 2005). Therefore, there might also be a tissue-specific inhibitor that blocks access of ADAR2 to editing sites in Ca$_V$1.3, which could not bind to the shorter dsRNA structure formed by gIQECS in the cell lines.

Chapter 4

Splicing of carboxyl-terminus of $Ca_V1.3$

4.1 Background and Objectives

Alternative splicing in the carboxyl-terminus (C-terminus) of L-type calcium channels regulate their biophysical properties. Auto-inhibitory control of Ca$_V$1.2 channel function was proposed to be based on a binding interaction between a pair of exposed arginine residues and negatively charged residues in α-helical motifs in a proximal (PCRD) and a distal (DCRD) conserved region of the C-terminus, respectively (Hulme et al., 2006). In Ca$_V$1.4 channels, activation, voltage-dependent inactivation (VDI) and calcium-dependent inactivation (CDI) are controlled by an intrinsic C-terminal modulator (CTM) (Singh et al., 2006).

In human Ca$_V$1.3, alternative splicing in the α_1 subunit C-terminus gives rise to a long form (Ca$_V$1.3$_{42}$) and a short form (Ca$_V$1.3$_{42a}$), with more pronounced activation of calcium current at negative voltages and faster inactivation observed in Ca$_V$1.3$_{42a}$ channels due to enhanced CDI (Singh et al., 2008). In the same study, CTM activity was restricted to the last 116 a.a. of the C-terminus, which was spliced out in the Ca$_V$1.3$_{42a}$ channels. 39 residues (1626-1664) that made up the conserved domain in PCRD confer modulation, as well as interact with CTM-containing peptides. Neutralization of the two conserved positive charges in PCRD did not inhibit intramolecular protein interaction, suggesting presence of other essential motifs in this 39-residue PCRD domain. In addition, the two conserved negative charges in DCRD are essential for binding of CTM-containing peptides to PCRD. The diminished CDI in human Ca$_V$1.3$_{42}$ clone was not observed in the rat clones (Yang et al., 2006), which was attributed to a single valine-to-alanine amino acid switch within Ca$_V$1.3 channel's distal C-terminus (Liu et al., 2010).

Several proteins have been reported to bind to interaction domains in the C-terminus of $Ca_V1.3_{42}$. Erbin binds to the type 1 PDZ-binding motif formed by the last four amino acids (ITTL) of neuronal $Ca_V1.3_{42}$ and thereby relieves the auto-inhibitory effect on VDF (Calin-Jageman et al., 2007). Selective association of Shank protein to the C-terminus of $Ca_V1.3_{42}$ channels is necessary for their synaptic targeting (Zhang et al., 2005), while that of RIM-binding protein to proline-rich motif in $Ca_V1.3$ C-terminus could affect the strength of synaptic transmission (Hibino et al., 2002).

Within rat auditory hair cells, alternative splicing of $Ca_V1.3$ channels at exon 41 results in deletion of the CaM-binding IQ motif, and hence abolition of CDI (Shen et al., 2006). Although the C-terminus of $Ca_V1.3$ channels contains several motifs important for modulation of its biophysical properties and localization, only three splice variants have been reported. We propose that the $Ca_V1.3$ gene is likely to exhibit extensive alternative splicing, especially in the C-terminus.

To address this gap in knowledge, we undertook to systematically screen for these splice variants in the C-terminus of $Ca_V1.3$ in the rat brain and identified four new loci of alternative splicing, in addition to that at exon 42/exon 42a. In the light of enhanced CDI with C-terminus truncation, and the delimitation of C-terminus, we also analysed the changes in the biophysical properties of splice variants in heterologous HEK293 cells via patch-clamp electrophysiology. In addition, sequencing of rat $Ca_V1.3_{42}$ clone in our lab as well as rat brain cDNA showed that the valine-to-alanine switch between the human and rat clones could be a cloning error. Hence, we corrected this mistake and characterized this new rat $Ca_V1.3_{42}$ clone via patch-clamp electrophysiology. Finally, since binding of proteins such as Erbin and Shank to C-terminus of $Ca_V1.3_{42}$ channels could facilitate synaptic targeting, alternative splicing of C-terminus may delete this binding motif and affect their subcellular localization. Thus, we constructed HA-tagged $Ca_V1.3$ splice variant clones and studied their expression patterns in primary hippocampal neurons via immunocytochemistry.

4.2 Materials and Methods

Nomenclature for describing alternatively spliced exon variants

Various suffixes and a prefixed applied an exon number are used to describe the type of alternative splicing that occurred at that exon locus (Table 1.1, Figure 1.3). An exon that was skipped in the course of alternative splicing is prefixed with a "Δ". Exons that are lengthen or shortened by alternative splicing are prefixed with "+" or "-" respectively. In addition, "a" or "d" denotes if changes to exon length occurred at the acceptor or donor site, respectively. Retained introns are indicated by "i" and mutually exclusive exons by "x". "*" denotes a cassette exon.

Transcript-scanning method

The transcript scanning method has been described in detail by Mittman *et al.* (1999) and Soong *et al*. (2002) for the systematic identification of loci for alternative splicing of the following voltage-gated calcium channel genes: *CACNA1I*, *CACNA1G*, *CACNA1A* and *CACNA1C*. In this method, we first designed PCR primer-pairs that span at least two exons or four splice boundaries along the length of the C-terminus of $Ca_V1.3$ gene (Fig. 4.1B). Sufficient pairs of primers were made such that amplicons from overlapping segments along the C-terminus of $Ca_V1.3$ sequence. The primers, designed using Oligo Primer Analysis Software (Molecular Biology Insights, Inc., CO, USA), are listed in Table 4.1. PCR was performed using rat brain cDNA as template and *Taq* DNA polymerase. The PCR programs employed depends on the expected product length and the estimated annealing temperatures of the primer pair used. Each pair of primer produced amplicons of varying sizes that corresponded to different alternative splice variants. These were visualized as multiple bands when separated by agarose gel electrophoresis. Each band was extracted and ligated into pGEM®-T Easy vector. These transcript clones were then transformed into DH10B *E.coli*. For each band cloned, eight to thirty positive clones (indicated by blue/white colony selection) were picked and further PCR screened using primers specific to the cloned insert. Colonies yielding different sized PCR products were expanded and the plasmid DNAs extracted for DNA sequencing. The DNA sequences were analysed, by comparison with $Ca_V1.3$ genomic and cDNA sequences, to identify the type of alternative splicing that had occurred and to determine the exact location of the alternative exon-intron splice junctions as well as their adherence to the "*gt…ag*" rule.

Construction of cloned C-terminus $Ca_V1.3$ library

PCR was performed using rat brain and rat heart cDNA libraries (Marathon-Ready™ cDNA, catalogue numbers: 639412 and 639416) as template and Elongase DNA polymerase (Invitrogen). Full-length PCR was performed using Adaptor Primer (AP) 1 (Clontech) and rat $Ca_V1.3$-specific primers situated in the 3'-untranslated regions (UTRs) of $Ca_V1.3_{42}$ isoform and $Ca_V1.3_{42a}$ isoform – 1D42a320L23 and 1D7563L23 respectively. A second nested PCR was performed to amplify $Ca_V1.3$ from IVS6 to end of C-terminus, using 1D4745F21 as sense primer and 1D42a518L21 and 1D7383L20 as anti-sense primers for $Ca_V1.3_{42}$ isoform and $Ca_V1.3_{42a}$ isoform, respectively. The resultant $Ca_V1.3$ C-terminus amplicons were sub-cloned into pGEM®-T Easy vector and transformed into DH10B *E.coli* cells. The positive transformants were then picked and grown in 96-well plates. A few clones from each plate were picked at random to verify that they were $Ca_V1.3$ clones. The picked clones were first expanded by growing in LB broth and the plasmid DNAs extracted and sent for sequencing analysis.

Table 4.1 Primers used for amplification of rat Ca$_V$1.3 α_1-subunit. Ta represents the annealing temperature. Region denotes the exons that the sense-anti-sense primers sit on.

	Primer name	Primer (5' → 3')	Ta (°C)	Region
Sense	AP1F27	CCATCCTAATACGACTCACTATAGGGC	61	1-49
Anti-Sense	1D7563L23	CTGACCGTCTGAGTGATGTTCTC		
Anti-sense	1D42a320L21	CTCACTGAGTCTCTGGCTTGG	61	1-42
Sense	1D4745F21	TGTGTGACCCGGACTCAGATT	55	37-49
Anti-sense	1D7383L20	CCAGCGAGCGTCTGATATGC		
Anti-sense	1D42a518L21	GTCTGCCTTACACAGGTCTGC	55	37-42a
Sense	1D4745F21	TGTGTGACCCGGACTCAGATT	52	36-41
Anti-sense	1D5343R21	CAAGAAGCGGAAAGAGCAAGG		
Sense	1D5148F22	ACGGACGGCTCTCAAGATCAAG	53	39-43
Anti-sense	1D5765R21	CCAATATGTCCAAAGCTGCCC		
Sense	1D5475F22	AGATGACGAACCAGAAGACTCC	52	42-46
Anti-sense	1D6082R21	TACAACAGGTACCCAGGCAGC		
Sense	1D6001F24	GGGGAGCAGGAATATTTCAGTAGC	52	45-48
Anti-sense	1D6492F24	TCGCTCAGAGTCTATGGACCAGGT		
Sense	1D6164F22	ACTCTCCCATTGGCTATGACTC	52	46-49
Anti-sense	1D6765R20	CATAGACGAGATGGAGAGCG		

Screening C-terminus library to determine abundance of splice variants

Pairs of primers were selected (from the list in Table 4.1) that flanks exons shown by transcript scanning to have alternatively spliced exons. The clones in the C-terminus library were then screened using each selected pair of primers by PCR. The clones that produced PCR products and migrated with the expected sizes (wild-type or splice variants) on the 5% agarose were counted. Clones were picked at random for sequencing to verify the validity of the screen. The quantity of alternatively spliced exon variants were expressed as a percentage of the total number of clones counted.

Construction of $Ca_V1.3$ α-subunits with C-terminal splice variants

To characterize the functional properties of $Ca_V1.3$ C-terminus splice variants, PCR fragments with the correct splice variation were substituted into full-length wild-type $Ca_V1.3_{42}$ (kindly provided by Prof Diane Lipscombe, GenBank accession number AF_370010) via restriction digest and ligation. The exon-combination of parental full-length rat $Ca_V1.3_{42}$ is 1-49. Large-scale plasmid DNA preparations of $Ca_V1.3_{42}$ and constructed splice variants were performed using PureLink™ HiPure Plasmid Filter Midiprep Kit (Invitrogen). Small-scale plasmid DNA preparations of $Ca_V1.3$ splice variants cloned into pGEM®-T Easy vector (Promega) were performed using Wizard® Plus SV Minipreps DNA Purification System (Promega). DNA purification from agarose gels were performed using QIAquick Gel Extraction Kit (Qiagen, Germany). All restriction enzymes were obtained from New England Biolabs (MA, USA) or Roche Applied Science (IN, USA).

Cloning of $Ca_V1.3_{\Delta 41}$

PCR fragment with splice variation of Δ41 amplified from adult rat brain was substituted into $Ca_V1.3_{42}$ using the restriction enzymes *Bam*HI and *Not*I. The PCR product was ligated into pGEM®-T Easy cloning vector and transformed into DH10B *E.coli*. The correct clone was identified by DNA sequencing and analysis against rat $Ca_V1.3$ mRNA sequence (GenBank accession number NM_017298). Plasmid extracted from the correct clone and rat $Ca_V1.3_{42}$ clone were similarly digested, purified after gel electrophoresis, ligated and transformed into DH10B *E.coli*. The full-length rat $Ca_V1.3$ subunit splice variant was named $Ca_V1.3_{\Delta 41}$. The $Ca_V1.3_{\Delta 41}$ (deleted exon 41) has exon 41 alternatively spliced out, thus generating a truncated protein that is different from $Ca_V1.3_{42}$ (contains exon 41).

Cloning of $Ca_V1.3_{43i}$

PCR fragment with splice variation of 43i amplified from adult rat brain was substituted into $Ca_V1.3_{42}$ using the restriction enzymes *Bst*EII and *Kpn*I. The PCR product was ligated into pGEM®-T Easy cloning vector and transformed into DH10B *E.coli*. The correct clone was identified by DNA sequencing and analysis against rat $Ca_V1.3$ mRNA sequence (GenBank accession number NM_017298). Plasmid extracted from the correct clone and rat $Ca_V1.3_{42}$ clone were similarly digested, purified after gel electrophoresis, ligated and transformed into DH10B *E.coli*. The full-length rat $Ca_V1.3$ subunit splice variant was named $Ca_V1.3_{43i}$. The $Ca_V1.3_{43i}$ (spliced out "intron" in exon 43) contains an exon, which is subjected to alternative splicing at the region used after PCRD, thus generating a truncated protein that has intact PCRD.

Cloning of $Ca_V1.3_{\Delta 44}$

PCR fragment with splice variation of Δ44 amplified from adult rat brain was substituted into $Ca_V1.3_{42}$ using the restriction enzymes *Bst*EII and *Kpn*I. The PCR product was ligated into pGEM®-T Easy cloning vector and transformed into DH10B *E.coli*. The correct clone was identified by DNA sequencing and analysis against rat $Ca_V1.3$ mRNA sequence (GenBank accession number NM_017298). Plasmid extracted from the correct clone and rat $Ca_V1.3_{42}$ clone were similarly digested, purified after gel electrophoresis, ligated and transformed into DH10B *E.coli*. The full-length rat $Ca_V1.3$ subunit splice variant was named $Ca_V1.3_{\Delta 44}$. The $Ca_V1.3_{\Delta 44}$ (deleted exon 44) has exon 44 spliced out, generating an in-frame protein that lacks exon 44.

Cloning of $Ca_V1.3_{48a-}$

PCR fragment with splice variation of 48a- amplified from adult rat brain was substituted into $Ca_V1.3_{42}$ using the restriction enzymes *Bgl*II and *Eco*RV. The PCR product was ligated into pGEM®-T Easy cloning vector and transformed into DH10B *E.coli*. The correct clone was identified by DNA sequencing and analysis against rat $Ca_V1.3$ mRNA sequence (GenBank accession number NM_017298). Plasmid extracted from the correct clone and rat $Ca_V1.3_{42}$ clone were similarly digested, purified after gel electrophoresis, ligated and transformed into DH10B *E.coli*. The full-length rat $Ca_V1.3$ subunit splice variant was named $Ca_V1.3_{48a-}$. The $Ca_V1.3_{48a-}$ construct (alternative 3' splice acceptor site in exon 48) has a portion of exon 48 spliced out, generating an in-frame protein that lacks the first 45 a.a. of exon 48.

Correction of cloning error in $Ca_V1.3_{42}$ clone

Sequencing of PCR fragment amplified with primers 1D6164F22 and 1D6765R20 using Elongase *Taq* (Invitrogen) showed G*T*C (coding for valine) in both adult rat brain and rat heart cDNA, instead of G*C*C (coding for alanine at position 2123) in $Ca_V1.3_{42}$ clone. The PCR product was ligated into pGEM®-T Easy (Promega) cloning vector and transformed into DH10B *E.coli*. The correct clone was identified by DNA sequencing and analysis against rat $Ca_V1.3$ mRNA sequence (GenBank accession number NM_017298) to ensure no further PCR errors. Plasmid extracted from the correct clone was digested with *Xho*I and *Kpn*I (Roche Applied Science) and substituted into $Ca_V1.3_{42}$. The corrected full-length rat $Ca_V1.3$ subunit splice variant was named $Ca_V1.3_{A2123V}$.

Transient expression of calcium channels in HEK 293 cells

HEK 293 cells were maintained in a growth media comprising of DMEM and 10% FBS, buffered with 20.71 mM sodium bicarbonate and 5.04 mM HEPES, and grown in a water-saturated 5% CO_2 incubator at 37 °C. Cultures were passaged at a split ratio of 1:5 upon reaching ~80% confluency. For transfection, HEK293 cells were harvested at ~80% confluency, counted and seeded onto poly-$_D$-lysine coated glass coverslips placed in 35 mm tissue culture dishes. The cells were seeded at a density of approximately 1×10^4 cells/cm^2 to ensure that isolated cells were available after transfection for whole-cell patch-clamp. The cells were then incubated for 16-24 h to allow the cells to adhere to the coverslips. About 1 h prior to transfection, fresh growth media without antibiotics was introduced. Approximately equi-molar ratios of α-subunit, β_{2a}-subunit, $\alpha_2\delta$-subunit DNA constructs as well as the T-antigen construct were co-transfected into the cells using calcium phosphate precipitation method (Huang et al., 2005). 1.75 μg of α-, 1.25 μg of β_{2a}-, 1.25 μg of $\alpha_2\delta$-subunits and 0.2 μg of T-antigen plasmids were mixed into 75 μl of 2.5 M $CaCl_2$ solution. 75 μl of 2x HBS (HEPES-buffered saline; 280 mM NaCl, 50 mM HEPES, 1.5 mM $NaPO_4$) was added and the mixture was mixed by pipetting. The mixture was incubated at r.t. for 10-15 min to allow precipitate formation. The DNA/$CaCl_2$ mixture was added dropwise over HEK 293 cells and gently mixed, and returned to incubator for 5-8 h. Transfection media was replaced with fresh growth media and cells were incubated for at least 36 h before patch-clamp recordings (Patil et al., 1998; Peterson et al., 1999). The rat β and rat $\alpha_2\delta$ subunit clones were kindly provided by Dr Terry P. Snutch (University of British Columbia, Vancouver, British Columbia, Canada).

Electrophysiological recordings and data analysis

Whole-cell patch-clamp recordings were performed on transfected cells between 36-72 h after transfection. Outward K^+ currents were blocked by Cs^+ in the internal and external solutions. For whole-cell patch-clamp recording, the internal solution (patch-pipette solution) contained the following (in mM): 138 Cs-$MeSO_3$, 5 CsCl, 0.5 EGTA, 10 HEPES, 1 $MgCl_2$, 2 mg/ml Mg-ATP, pH 7.3 (adjusted with CsOH), 290 mOsm with glucose. The external solution contained the following (in mM): 10 HEPES, 140 tetraethylammonium methanesulfonate, 10 $BaCl_2$, or 10 $CaCl_2$ (pH adjusted to 7.4 with CsOH and osmolarity to 290-310 with glucose). Pipettes of resistance 1.5-2 MΩ were used. Whole-cell currents, obtained under voltage clamp with an Axopatch 200B amplifier (Molecular Devices, Union City, CA), were filtered at 1-5 kHz and sampled at 5-50 kHz, and the series resistance was typically <5MÙ after >70% compensation. A P/4 protocol was used to subtract on-line the leak and capacitive transients.

Data were acquired using the software pClamp9 (Molecular Devices) and were analysed and fitted using Graphpad Prism IV software (San Diego, CA) and Microsoft (Seattle, WA) Excel. Data are expressed as mean values ± SE. Statistical analysis was performed using paired or unpaired Student's *t* test.

To assess the current-voltage (*I-V*) curve relationship of the channels, transfected cells were depolarized to a family of test potentials of -70 to 60 mV, in steps of 10 mV increments, from a holding potential of -90 mV. The peak current evoked by each voltage was normalized to the maximal current obtained for each cell recorded and fitted with the following equation:

$$I = G_{\mathrm{max}}(V\text{-}E_{\mathrm{rev}})/(1+\exp[(V\text{-}V_{1/2\mathrm{act}})/k_{\mathrm{act}}]);$$

where G_{max} is the maximum conductance of the cell, E_{rev} is the reversal potential, $V_{1/2act}$ is the voltage for half-maximal activation, k_{act} is the slope.

Steady-state inactivation properties were determined by comparing the test current obtained after a long depolarising pulse to an initial pre-pulse. For the -90 mV holding potential, a pre-pulse current was evoked by stepping to 10 mV for 30 ms. This was followed by a family of 15 sec-long depolarizing pulses ranging from -100 to 60 mV. Next, a test-pulse current was evoked by stepping the cell to 10 mV for 100 ms. The peak current evoked by each test pulse was divided by the peak current evoked by the pre-pulse to obtain the normalized current. The values were fitted with a single Boltzmann equation:

$$I_{relative} = I_{min} + (I_{max} - I_{min})/[1 + \exp(V_{1/2act} + V)/k_{inact});$$

where $I_{relative}$ is the normalized current, $V_{1/2act}$ is the potential for half-inactivation and k_{inact} is the slope value.

The strength of calcium dependent inactivation (CDI) exhibited by the channel is expressed by the f-value (Mori et al., 2004). To determine the f-value, the current amplitude that remained a given time point (i.e. 30, 50, 100, 200, 300, 400 and 500 ms) after depolarization was first measured and normalized against the peak current to obtain the residual current (i.e. r_{30} and r_{300} for 30 and 300 ms, respectively). Next, the f-value was calculated by subtracting the residual I_{Ba} with the residual I_{Ca}. An f-value of 0 indicates no CDI, while the maximal f-value of 1 indicates complete CDI. For comparison between channels, we compared the f-values obtained from currents evoked by depolarization to 10 mV. The presence of CDI may also be seen in the profile of the residual I_{Ca} evoked by a family of voltages. When plotted against voltage, the ‘U’-shaped dependence of residual I_{Ca} values on voltage is a tell-tale trait of CDI.

For voltage-dependent inactivation (VDI), cells were placed in the external solution with Ba^{2+} as the charge carrier and depolarized to V_{max}, from a holding potential of -90 mV. As time elapsed, the current evoked by V_{max} decayed and the amplitude was measured at different time points. These were subtracted from the peak current evoked to obtain the inactivated current. This was then expressed as a percentage of the peak current (percentage inactivation).

For steady-state activation, we analysed the tail currents (G) obtained at the end of a short depolarizing pulse. Cells were held at -90 mV before depolarizing to a family of voltages, ranging from -80 to 80 mV, in steps of 10 mV increments, for 20 ms. Following which, a repolarization to -50 mV for 10 ms evokes the tail currents that are measured. The peak of each tail current was normalized to the maximum obtained for each cell recording and fitted with a single Boltzmann equation:

$$G/G_{\mathrm{max}} = G_{\mathrm{min}} + (G_{\mathrm{max}} - G_{\mathrm{min}})/\{1+\exp[(V_{1/2\ \mathrm{act}} - V)/k_{\mathrm{act}}]\};$$

where G is the tail current, G_{max} is the tail current evoked by a depolarization to +120 mV, V is the membrane potential of the test pulse, k_{act} is the slope factor and $V_{1/2\mathrm{act}}$ was calculated when $G=0.5G_{\mathrm{max}}$.

Fractional recovery from inactivation was determined using a two-pulse protocol whereby following a 2 sec depolarizing pre-pulse to V_{max} (determined from the *I-V* properties of the transfected cell), a test-pulse is applied after a certain time period, ΔT, has elapsed. The peak I_{Ba} measured during the test pulse was expressed as a fraction of peak I_{Ba} obtained at the beginning of the pre-pulse to obtain the fraction of recovery. This was plotted against *ΔT*. The curve was obtained by fitting the values with a double exponential equation:

$$Y = Y_{\min} + A_f[1\text{-}\exp(\text{-}t/\tau_f)] + A_s[1\text{-}\exp(\text{-}t/\tau_s)];$$

where Y is the fraction of recovery, A_f and A_s are the maximum values of the fast and slow components, and τ_f and τ_s are their time constants, respectively.

Construction of HA-tagged Ca$_V$1.3 C-terminus splice variants

The generation of Ca$_V$1.3$_{HA}$ construct has been described by Zhang *et al* (2006). Briefly the HA tag and the flanking sequences were inserted into extracellular S5-S6 loop of domain II of rat Ca$_V$1.3$_{42}$ plasmid between amino acids Q693 and T694. The resulting sequence is 687FNFDETQ*TRH***YPYDVPDYA***VTF*DEMQTKRSTFD694 (HA sequence is in bold, added sequence is in italics) The HA-tag and flanking sequences were inserted by polymerase chain reaction (PCR) followed by ligation using *Ale*I (658) and *Bam*HI (2756) sites and verified by sequencing. Splice variant clones - Ca$_V$1.3$_{\Delta 41}$, Ca$_V$1.3$_{43i}$, Ca$_V$1.3$_{\Delta 44}$ and Ca$_V$1.3$_{48a-}$, were then substituted into Ca$_V$1.3$_{HA}$ via restriction digests using *Nhe*I and *Bam*HI, DNA purification from agarose gels, ligation and transformation into DH10B *E.coli*.

Hippocampal neuron culture and transfection.

Low-density dissociated-cell culture of hippocampal neurons rat embryonic 18 (E18) rat was prepared, according to established protocol (Kaech and Banker, 2006). The neurons were cultured on poly-D-lysine-treated coverslips, which were suspended above an astrocyte feeder layer and maintained in serum-free B27/neurobasal medium supplemented with insulin, apo-transferrin, superoxide dismutase and MITO+ serum extender, in a 24-well plate format. The culturing media had to be optimized in order to facilitate neuronal survival to DIV 18-20, in order for synaptic targeting of proteins to occur. Hippocampal cultures have been used widely for visualizing the subcellular localization of endogenous or expressed proteins for imaging protein trafficking. Preparation of glial feeder cultures begun at least 2 weeks in advance, and approximately 5 days was needed to prepare coverslips as a substrate for neuronal growth. Dissection of hippocampus from rat fetuses and plating of hippocampal neurons takes 2-3 hours. For targeting experiments, primary hippocampal neuronal cultures at DIV 5-7 were transfected with HA-$\text{Ca}_V1.3_{\Delta 41}$, HA-$\text{Ca}_V1.3_{\Delta 43B}$, HA-$\text{Ca}_V1.3_{44-}$, HA-$\text{Ca}_V1.3_{\Delta 48}$, HA-$\text{Ca}_V1.3_{42}$ or HA-$\text{Ca}_V1.3_{42a}$ (1.7 μg) and rat β_{2a} (1.25 μg) and rat $\alpha_2\delta$ (1.25 μg), using 0.5 μl of PLUS Reagent and 1 μl of Lipofectamine LTX (Invitrogen, Carlsbad, CA). Cells were incubated in DNA/Lipofectamine LTX mixture for 5 h in 37 °C incubator, before coverslips were returned into conditioned medium.

Immunocytochemistry and confocal imaging

For the primary hippocampal neurons, cells were immunostained and analyzed 11-14 days after transfection. For staining of surface-expressed HA-$\text{Ca}_V1.3$, living neurons were incubated with the rat anti-HA antibody (used at 1:100, 12CA5, Roche) for 30 min at 37°C. Then the cultures were rinsed in Hank's buffered saline, fixed in 4% paraformaldehyde/4% sucrose for 10 min and blocked with 5% normal goat serum in PBS, 0.2% bovine serum albumin, and 0.2% Triton X-100 (PBS/BSA/Triton) for 1 h. Second primary antibodies (MAP2/synapsin) were applied in PBS/BSA/Trixton at 4 °C overnight and then incubated with the fluorochrome-conjugated secondary antibodies for 1 h. Coverslips were then washed and mounted in ProLong® Gold Antifade Reagent with DAPI (Invitrogen) to retard photobleaching. Preparations were analyzed using a Zeiss LSM-510 META confocal microscope using a 63x 1.4

numerical aperture (NA) oil immersion objective in the inverted configuration. Image brightness/contrast adjustments were performed on the Zeiss LSM Image Browser software, version 4.0.0.157. Images were then recorded and exported as tiff formats.

4.3 Results

Identification of novel $Ca_V1.3$ C-terminus splice variants in rat brain

To determine the different alternatively spliced exons in the $Ca_V1.3$ C-terminus, we employed the transcript scanning strategy previously described (Mittman et al., 1999; Soong et al., 2002). Transcript scanning is a straightforward and comprehensive method to systematically identify the various alternatively spliced exons in a gene using PCR and sequence analysis. Briefly, overlapping segments of the C-terminus of $Ca_V1.3$ gene was PCR amplified, using primer pairs spanning at least two exons or four splice boundaries (Fig 4.1B). The amplification of each segment increases the copy numbers, and therefore, the odds of discovering splice variations in that region. Based on the understanding that alternative splicing often results in a change in exon sizes (with few exceptions), the presence of different-sized PCR amplicons from each primer-pair indicate the presence of different population of splice variants.

As $Ca_V1.3$ is predominantly expressed in the brain (Hell et al., 1993), we used rat brain cDNA as the PCR template. In order to scan the combination of exons in C-terminus of $Ca_V1.3$, we first amplified the entire C-terminus, before generating at least five overlapping amplicons (Fig 4.1B). The products derived from PCR were separated by electrophoresis on an agarose gel (Fig 4.1C). Multiple bands were observed in some lanes and these may correspond to different populations of alternatively spliced $Ca_V1.3$ transcripts. Bands from the first round of PCR were extracted, cloned into pGEMT$^{®}$-T Easy vectors and transformed into DH10B *E.coli*, and the resultant bacteria colonies were individually PCR-screened to isolate clones containing different splice variations. Figure 4.1D shows examples of different-sized

PCR products obtained from different splice variant clones. Clones were selected for DNA sequencing to identify the exons that were alternatively spliced as well as to exclude clones derived from non-specific amplicons. The exact identity and mechanism of alternative splicing, in terms of the new exon-intron boundaries and their adherence to the "*gt…ag*" canonical splice junction (Sharp and Burge, 1997) was determined by analysis of the DNA sequence in comparison with the $Ca_V1.3$ genomic sequence (NW_047469, GI:62662350).

Transcript scanning of $Ca_V1.3$ from rat brain cDNA revealed alternative splicing in five loci on the C-terminus (Fig 4.2 – 4.3), of which some may undergo more than one mode of splicing with some adjacent exons alternatively spliced in tandem. Altogether there are three alternative splice acceptor sites, two exon-skippings, one cassette exon and one intron retention. In all cases, use of the canonical "*gt…ag*" splice junctions in the alternative forms were preserved (Fig 4.3). The types of alternative splicing in the C-terminus of $Ca_V1.3$ are as follows:

(1) Exon 41a-. The alternative use of splice acceptor site on exon 41 junction resulted in the removal of the IQ motif. This led to a frame-shift, resulting in an extension of 27 unrelated a.a. after exon 40 before a pre-mature stop codon. This alternative splicing has already been reported and denoted as $Ca_V1.3_{\Delta IQ}$ (Shen et al., 2006).

(2) Δ41. Skipping of exon 41 resulted in the removal of the IQ motif, and a frame-shift with a subsequent stop codon seven a.a. after exon 40. Its full length construct is denoted as $Ca_V1.3_{\Delta 41}$.

(3) Exon 42a*. Alternative splicing of cassette exon 42a resulted in a premature stop in $Ca_V1.3$, just six a.a. after exon 41. This alternative splicing was previously reported

and characterized as $Ca_V1.3_{42a}$ (Xu and Lipscombe, 2001; Singh et al., 2008; Liu et al., 2010).

(4) Exon 43a-. The splicing of exon 42 to an alternative acceptor site in exon 43 led to a frame-shift with stop codon after 13 a.a. This alternative splicing has previously been identified (Shen, 2006).

(5) Exon 43i. This novel alternative splicing in the middle portion of exon 43 resulted in a frame-shift in the remainder 3' half of exon 43, adding on 179 unrelated a.a. before a stop codon. The excised portion may have been a previously unidentified intron, and inclusion of this "intron" is constitutive. Alternative splicing of exon 43i follows the canonical "*gt...ag*" rule. Its full length construct is denoted as $Ca_V1.3_{43i}$.

(6) Δ44. The skipping of exon 44 removed the nine a.a. encoded, but did not cause a frame-shift. Hence, the resultant protein still retains the distal C-terminal regulatory domain (DCRD) and the C-terminal type I PDZ-domain ITTL. Its full length construct is denoted as $Ca_V1.3_{\Delta 44}$.

(7) Exon 48a-. The use of alternative splice acceptor site on exon 48 results in the deletion of 44 a.a. in exon 48, but does not result in frame-shifting. In addition, as this alternative splicing site occurs before DCRD, the resultant protein retains the DCRD and the C-terminal type I PDZ-domain ITTL. Its full length construct is denoted as $Ca_V1.3_{48a-}$.

It is important to establish the frequency of occurrence of the alternative splice variants. Sequence alternations due to alternative splicing may alter the channel's properties. The net behaviour of $Ca_V1.3$ in a cell (i.e. neuron) would therefore be a collective of the individual functional behaviour of each population of alternatively spliced and WT $Ca_V1.3$ channels. The abundance of each splice variant, no doubt, influences its degree of contribution to the net $Ca_V1.3$ properties.

As transcript scanning strategy is a robust method that allows us to detect sparsely occurring splice variants; moreover in transcript scanning, because only a portion of the $Ca_V1.3$ transcript was amplified, the frequency of the splice variants that we are able to quantify, i.e. by counting the number of clones that display exon-size variations, may not be a good estimate of the actual population of these splice variants in complete C-terminus of $Ca_V1.3$ transcripts. Therefore to determine the frequency of splice variants that better reflect the expressed $Ca_V1.3$ found in cells, we created a library of $Ca_V1.3$ clones with complete C-terminus. To do this, we designed primers that reside in exon 36 and 3' UTR (untranslated region) of the $Ca_V1.3$ gene and perform long PCR amplification using a proof-reading polymerase and rat brain cDNA as template. The resultant ~3 kb amplicons were sub-cloned into pGEM®-T Easy vector and transformed into DH10B bacteria. The positive white transformants were then picked and grown in 96-well plates for colony screening. Using primer-pairs that target alternatively spliced loci, the $Ca_V1.3$ C-terminus clones from the library were PCR-screened for the various splice variations. Clones producing PCR product size alterations that tallied with the expected changes (like the examples shown in Fig 4.1D), calculated based on the splice mechanisms previously determined, were counted and expressed as a percentage of the total population. Clones were selected at random for DNA sequencing to confirm the fidelity of the PCR screen. In summary, the results are (expressed as a percentage of the total population, n = no of clones screened): exon 41a- – 13.5%, n =237; Δ41 – 4.6%, n =237; exon 43a- – 44.7%, n =237; exon 43i – 5.1%, n = 237; Δ44 – 9.7%, n =237; and exon 48a- – 6.3%, n =237.

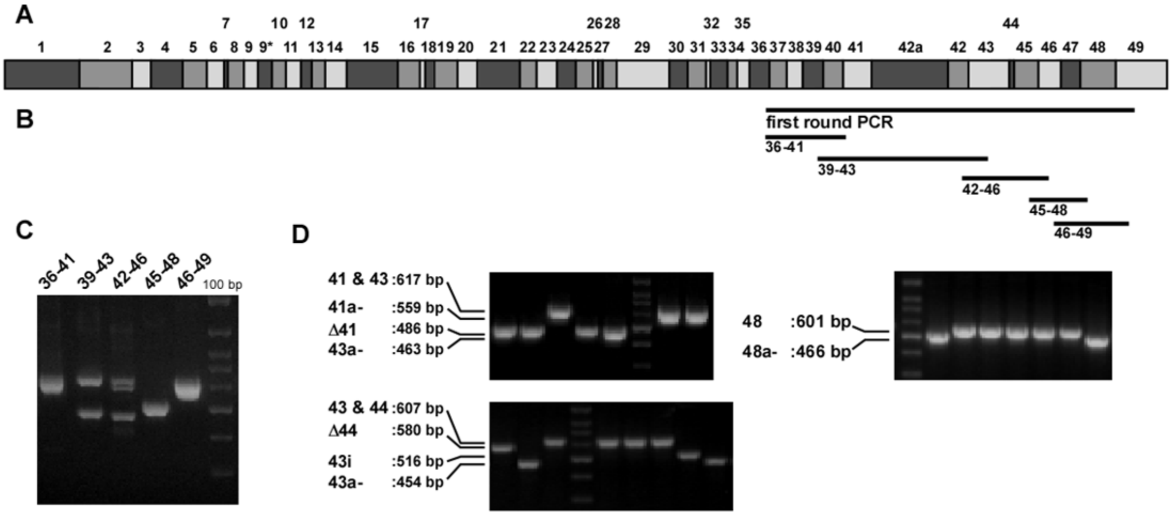

Figure 4.1 Schematic representation of rat L-type voltage-gated calcium channel, $Ca_V1.3$ subunit and transcript scanning PCRs used to detect splice variations. *A*, schematic representations of the $Ca_V1.3$ gene divided into 49 exons. The width of the exons shown here are relative to their actual nt lengths. *B*. Locations of the scanning reactions to detect splice variations. The lines represent the PCR-amplicons produced by primer-pairs that span at least two exons. The amplicons are spaced at overlapping intervals along exon 36 to exon 49 of the gene, and thus scans the entire C-terminus diagram of the $Ca_V1.3$ transcript for alternative splicing of exons. Amplicon sizes were restricted by considerations to (1) enable gel resolution of splice variants, (2) facilitate ligation into cloning vector, and (3) length of coverage by DNA sequencing per reaction. *C*, Transcript scanning of PCR products separated by electrophoresis on an agarose gel. Labelled above each lane are the exons spanned and amplified as shown in B. multiple bands are shown in some of the lanes, which may correspond to the different populations of transcripts with alterative splicing that altered exon sizes. Bands from each lane are extracted and cloned. D, Analysis of PCR products amplified from $Ca_V1.3$ clones containing alternatively spliced exons using selected primer-pairs that flank the splice loci. Changes in exon size from alternative splicing are reflected in the different sizes of PCR products. The exact exon sizes are calculated by analysis of DNA sequencing data. Sizes of the PCR products are indicated to the left of each gel image.

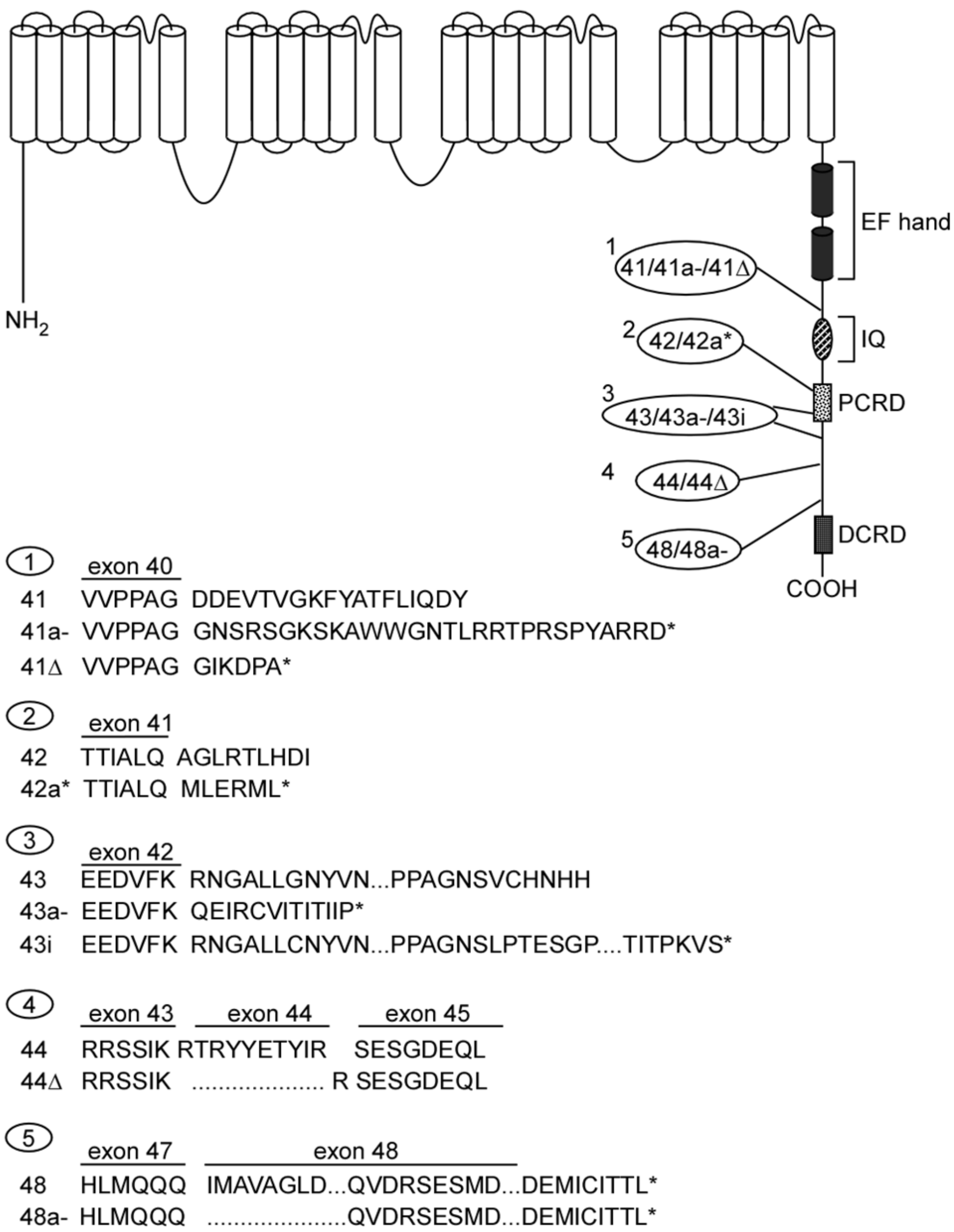

Figure 4.2 Five loci of Ca$_V$1.3 splice variations detected in the C-terminus by transcript scanning. The postulated schematic diagram (*top*) shows a more detailed secondary structure of Ca$_V$1.3, along with loci of splice variation (*1-5*), labelled according to transcript variant names. Modulatory domains important for channel activation and inactivation in the C-terminus are shown. *EF*, EF-hand; *IQ*, IQ-like CaM interaction domain; *PCRD*, proximal C-terminal regulatory domain; *DCRD*, distal C-terminal regulatory domain. Detailed changes in amino acid composition resulting from splice variation at each of five loci are shown below. At *locus 1* and *3*, alternative splicing at exon 41 and 43 removes the IQ motif and portions of exon 43 respectively, resulting in frame-shifts and premature truncations of Ca$_V$1.3 channel proteins.

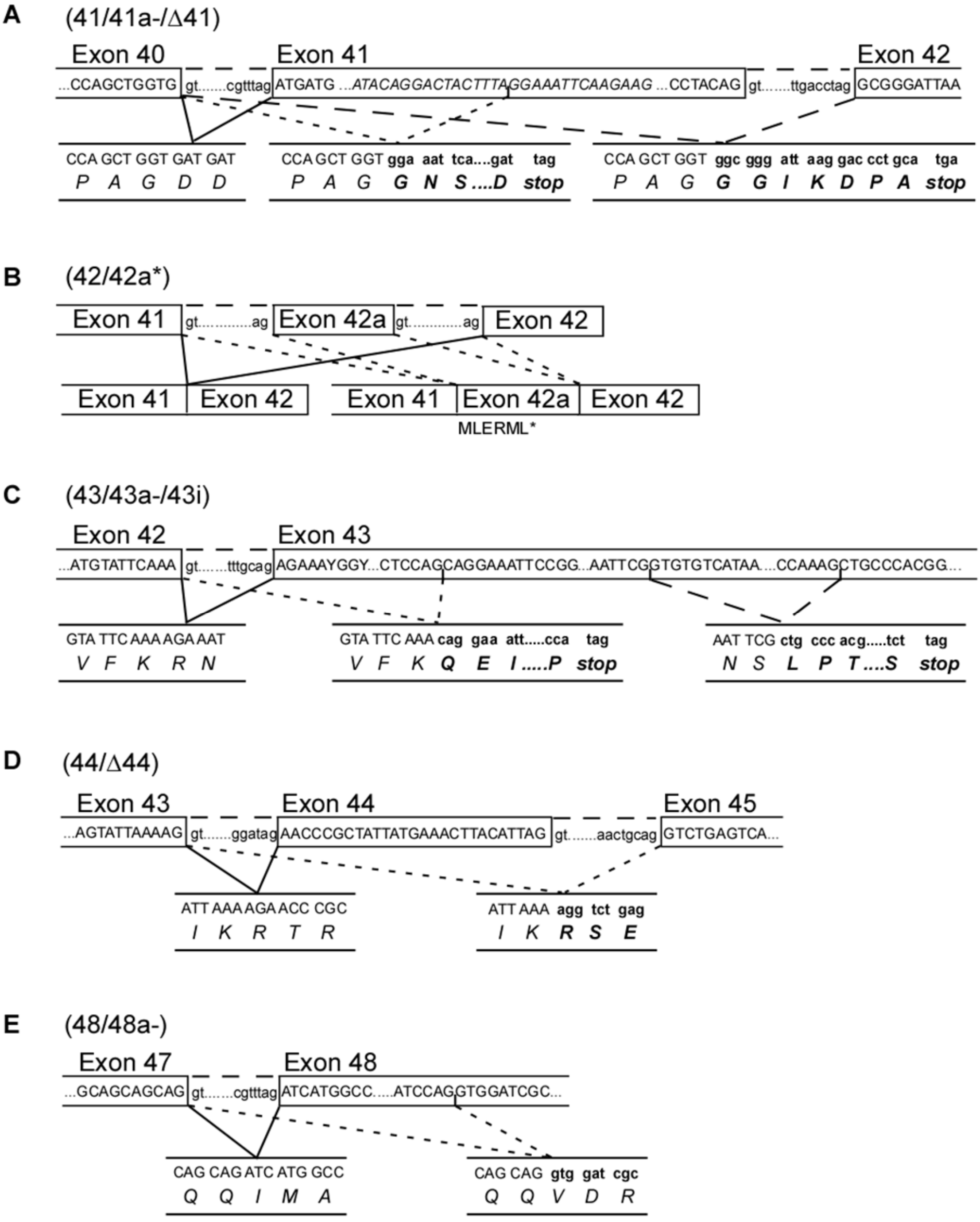

Figure 4.3 Postulated mechanisms underlying splice variation of Ca$_V$1.3. *A-E*, *Top row*, nucleotide sequence of relevant exon-intron boundaries. *Bottom row*, resultant transcript and encoded amino acid of each variant. Mechanism for splicing were alternate acceptor sites (*A* and *C*), exon skipping (*A* and *D*), cassette exon (*B*) and intron retention (C).

Modulation of channel biophysical properties by correction to $Ca_V1.3_{A2123V}$

In human $Ca_V1.3$, alternative splicing in the α_1 subunit C terminus gives rise to a long form ($Ca_V1.3_{42}$) and a short form ($Ca_V1.3_{42a}$), with more pronounced activation of calcium current at negative voltages and faster inactivation observed in $Ca_V1.3_{42a}$ channels due to enhanced CDI (Singh et al., 2008). However, this diminished CDI of $Ca_V1.3_{42}$ isoform was not replicated in the rat clones, and was attributed to a single valine-to-alanine amino acid switch within $Ca_V1.3$ channel's CDI-inhibiting molecule (ICDI) (Fig 4.4A) (Liu et al., 2010). Sequencing of PCR fragment amplified with primers flanking exons 48-49 revealed G*T*C (coding for valine) in both rat brain (Fig 4.4B) and rat heart cDNA (data not shown), instead of G*C*C (coding for alanine) at position 2123 in rat $Ca_V1.3_{42}$ clone (Fig 4.4B). The PCR product was ligated into pGEM®-T Easy (Promega) cloning vector and transformed into DH10B *E.coli*. The correct clone was identified by DNA sequencing and blasted against rat $Ca_V1.3$ mRNA sequence (GenBank accession number NM_017298) to ensure no further PCR errors.

To assess the current-voltage (*I-V*) relationship of the channels, transfected cells were depolarized to a family of test potentials of -70 to 60 mV, in steps of 10 mV increments, from a holding potential of -90 mV (Figure 4.4C). The current trace profile for $Ca_V1.3_{42a}$ displayed a slower inactivating I_{Ba} compared to the corrected clone $Ca_V1.3_{A2123V}$ (Fig 4.4D, grey traces), but showed an early and much pronounced inactivation of I_{Ca} (Fig 4.4D, black traces). In the *I-V* curves, $Ca_V1.3_{42a}$ displayed a pronounced shift in the hyperpolarized direction, indicating a more negatively activating channel in both Ba^{2+} and Ca^{2+} (Figure 4.4E-H). This was also reflected in a pronounced hyperpolarized shift in voltage for half-maximal activation, $V_{½\ act}$, by 11.22 mV in Ba^{2+} ($Ca_V1.3_{A2123V}$: -24.33 ± 0.49 mV, $n = 17$; $Ca_V1.3_{42a}$: -35.55 ± 0.53

mV, $n = 13$; Table 4.2) and 10.87 mV in Ca^{2+} ($Ca_V1.3_{A2123V}$: -12.28 ± 0.53 mV, $n = 14$; $Ca_V1.3_{42a}$: -23.15 ± 0.39 mV, $n = 13$; Table 4.3) with respect to $Ca_V1.3_{A2123V}$ (both $p < 0.0001$; unpaired *t*-test). This negative shift was because of the significant decrease in slope of activation, k_{act}, by 2.43 mV in Ba^{2+} ($Ca_V1.3_{A2123V}$: -8.03 ± 0.32 mV, $n = 17$; $Ca_V1.3_{42a}$: -5.60 ± 0.40 mV, $n = 13$; Table 4.2) and 2.57 mV in Ca^{2+} ($Ca_V1.3_{A2123V}$: -9.39 ± 0.30 mV, $n = 14$; $Ca_V1.3_{42a}$: -6.82 ± 0.27 mV, $n = 13$; Table 4.3).

Rapid inactivation of activated channels due to Ca^{2+} is a phenomenon displayed by many high-voltage activated channels. In contrast, with Ba^{2+} as the charge carrier, these channels inactivate more slowly by virtue of voltage (voltage-dependent inactivation or VDI). The mechanism of CDI involves the Ca^{2+}-sensing apparatus, comprising of the EF-hand and IQ motifs that reside in the cytosolic proximal C-terminus region of the Ca_V α_1 subunit, together with the calcium-binding protein, calmodulin (CaM), tethered there. Upon binding of Ca^{2+} to CaM, the conformational changes in the channel hasten closure of the inactivation gate. In the human $Ca_V1.3$, the CTM domain in DCRD interacts with the calcium-sensing apparatus and greatly subdues CDI (Singh et al., 2008). From the profiles of the exemplary traces in Figure 4.4D, it is clear that calcium inactivation in the corrected $Ca_V1.3_{A2123V}$ clone is slower than $Ca_V1.3_{42a}$ clone. To quantify the degree of CDI exhibited by the channels, the fraction of current that remain at a given time point after depolarization (residual current; i.e. r_{30} and r_{300} for 30 and 300 ms, respectively; Figure 4.5A-J) to different voltages are determined. The difference between the residual current of Ba^{2+} and Ca^{2+} is a measure of CDI strength (*f*-value). Here, we calculate the *f*-value obtained at 0 mV (f_0; Figures 4.5A-J)

For the corrected $Ca_V1.3_{A2123V}$ channel, the residue current for Ca^{2+} was smaller than Ba^{2+} (Figure 4.5A-B). This became more evident with residual currents measured at longer depolarization time (Figure 4.5C-E), indicating inactivation by Ca^{2+} (f_0, 30 ms, 0.14 ± 0.03; 50 ms, 0.19 ± 0.04; 100 ms, 0.25 ± 0.04; 200 ms, 0.31 ± 0.04; 300 ms, 0.35 ± 0.04). In contrast, short variant $Ca_V1.3_{42a}$ exhibited 2-fold greater f_0 (0.71 ± 0.03) at 300 ms. Even as early as 30 ms, CDI was already very much pronounced with $f_0 = 0.60 \pm 0.02$ (4.3-fold greater than $Ca_V1.3_{A2123V}$). The residual current of $Ca_V1.3_{42a}$ in Ca^{2+} exhibits a U-shaped dependence on voltage (Figure 4.5F-J) that is distinctive of CDI. Because more inactivation occurs when more Ca^{2+} enters the cell, the trough of the U-shape would correspond closely to its *I-V* curve.

Hence, correction of alanine-to-valine in amino acid position 2123 in rat $Ca_V1.3_{42}$ clone was sufficient to replicate the diminished CDI observed in human $Ca_V1.3_{42}$. This would suggest that the valine residue is crucial for interaction of the CTM with the calcium-sensing apparatus in the proximal C-terminus and could greatly repress the CDI of $Ca_V1.3$ channels.

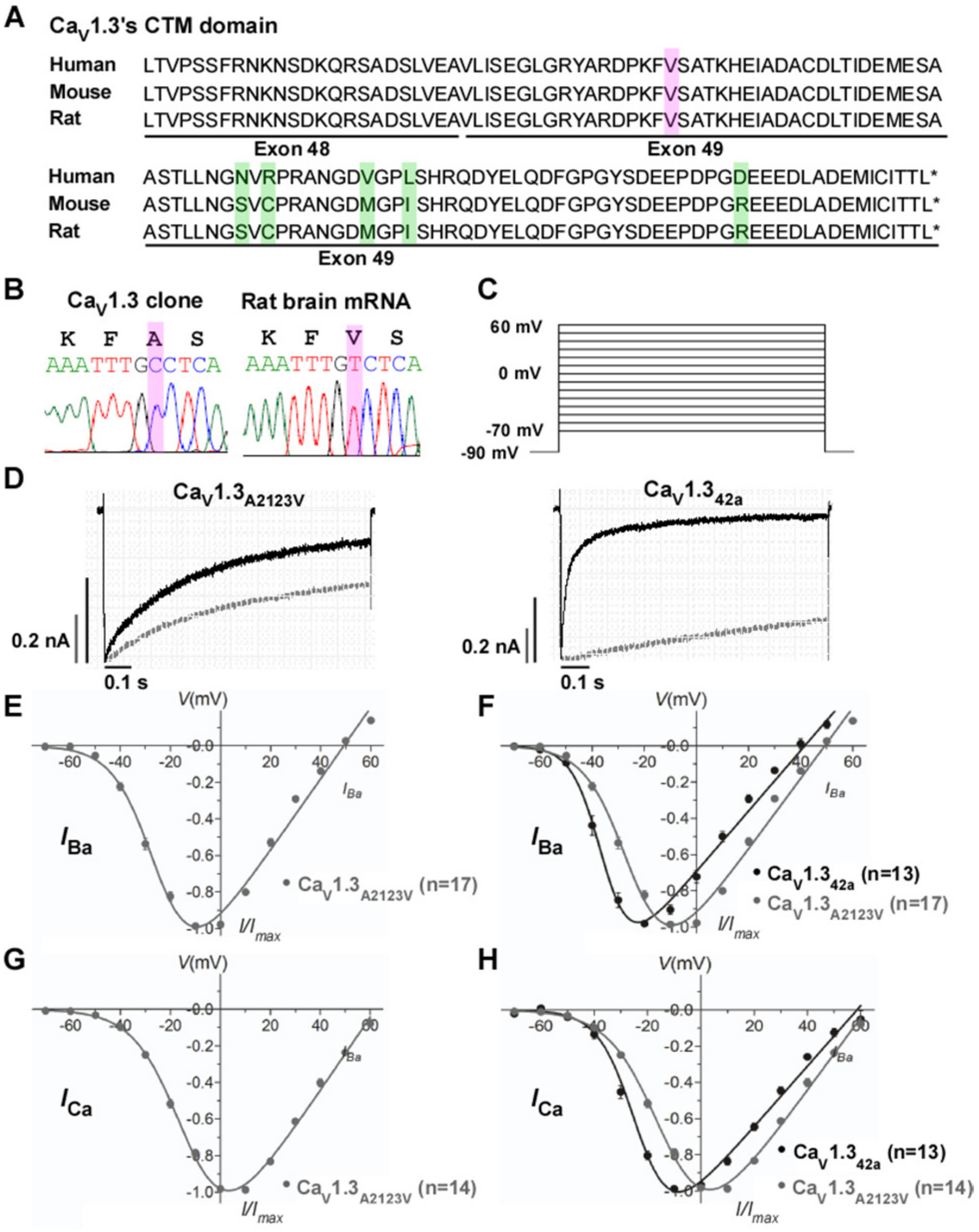

Figure 4.4. Correction of cloning error in original $Ca_V1.3_{42}$ clone to $Ca_V1.3_{A2123V}$. *A*, Amino-acid alignments of CTM region for long variants of human, mouse and rat $Ca_V1.3$ (GenBank Accession numbers: human: NM_000720, mouse: NM_028981, rat: NM_017298). Positions of exons 48 and 49 are given. Highlighted green residues mark the differences between these variants. Highlighted purple residues mark the position whereby alanine is observed in position 2123 in rat $Ca_V1.3_{42}$ clone (GenBank Accession number D38101) instead of valine. *B*, *left*, direct sequencing results of rat clone $Ca_V1.3_{42}$ clone. Peptide combination is listed in black; *right*, direct sequencing results of RT-PCR amplified from rat brain. Highlighted purple residues mark the position of cloning error. *C-H*, current-voltage relationship of corrected $Ca_V1.3_{A2123V}$ and splice variant $Ca_V1.3_{42a}$. *C*, Voltage protocol for determining *I-V* relationship: 400 ms depolarisations to potentials ranging, in 10 mV increments, from -70 to 60 mV (holding potential -90 mV). *D*, representative I_{Ba} (grey) and I_{Ca} (black) traces during depolarization to 10 mV. The I_{Ba} and I_{Ca} traces were scaled to enable comparison between the two profiles. Current scales were drawn for both I_{Ba} (grey) and I_{Ca} (black). The time scales for each I_{Ba} and I_{Ca} pair are the same. *E-F*, normalized *I-V* plots for I_{Ba} of $Ca_V1.3_{A2123V}$ and $Ca_V1.3_{42a}$, respectively. The curves were fitted with the equation described in methods. In paratheses are the number of cells recorded. *G-H*, same as *E-F*, but for I_{Ca}.

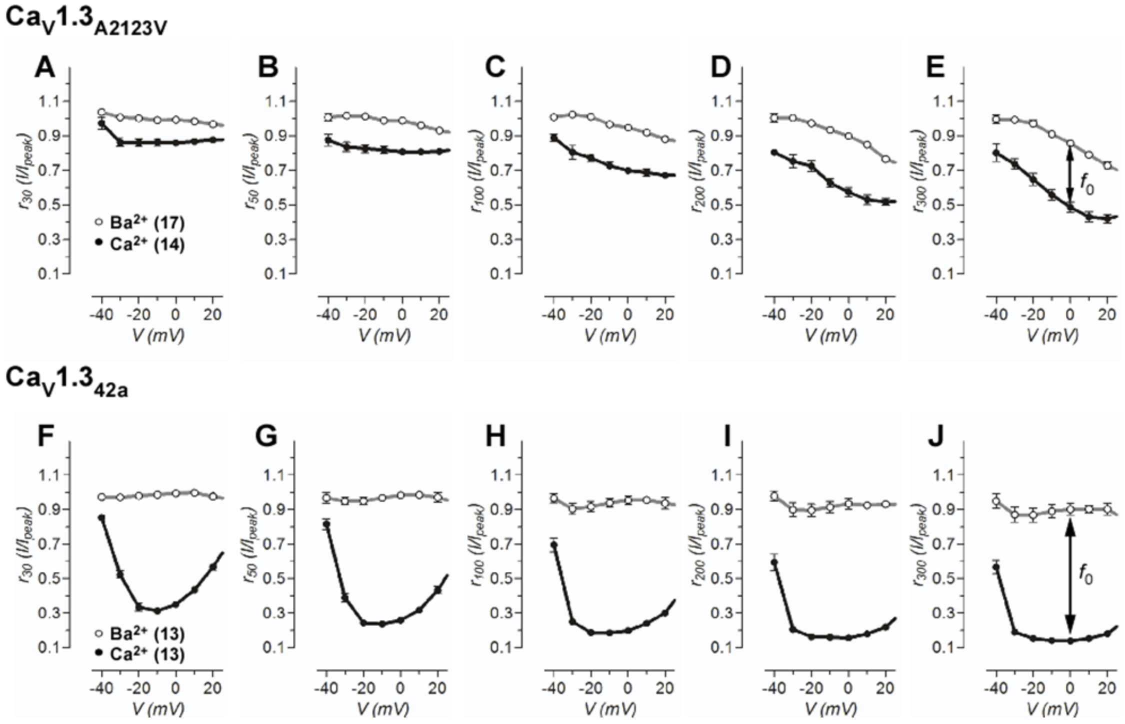

Figure 4.5 Calcium-dependent inactivation of current through Ca$_V$1.3$_{A2123V}$ and Ca$_V$1.3$_{42a}$. *A-E*, the fraction of peak current, I_{peak}, that remained at different time intervals of 30-, 50-, 100, 200- and 300-ms upon depolarization to the indicated voltages for Ca$_V$1.3$_{A2123V}$ channels. The difference between the remaining current for I_{Ba} and I_{Ca}, *f*-value, indicates the strength of calcium-dependent inactivation, CDI. The presence of CDI is also marked by "U"-shaped dependence of I_{Ca} on voltage (i.e. Ca$_V$1.3$_{42a}$, black curves). The curves are visual fits of the values plotted to facilitate comparison. The number of cells recorded is given in parentheses. *F-J*, the fraction of peak current, I_{peak}, that remained at different time intervals of 30-, 50-, 100, 200- and 300-ms upon depolarization to the indicated voltages for Ca$_V$1.3$_{42a}$ channels.

Modulation of channel biophysical properties by alternative splicing of the C-terminus

Alternative splicing occurs at five loci on the C-terminus of $Ca_V1.3$, resulting in at least eight splice variants, namely $Ca_V1.3_{42}$, $Ca_V1.3_{42a}$, $Ca_V1.3_{\Delta IQ}$, $Ca_V1.3_{\Delta 41}$, $Ca_V1.3_{43a-}$, $Ca_V1.3_{43i}$, $Ca_V1.3_{\Delta 44}$ and $Ca_V1.3_{48a-}$. Of these eight, $Ca_V1.3_{\Delta IQ}$ and $Ca_V1.3_{43a-}$ had been previously characterized by a previous graduate student in the laboratory (Shen, 2006), while the two predominant isoforms $Ca_V1.3_{42}$ and $Ca_V1.3_{42a}$ have been reported (Singh et al., 2008). We attempt to characterize the remainder four novel splice variants, which alters the C-terminus of $Ca_V1.3$ (Figure 4.6A). $Ca_V1.3_{\Delta 41}$ deletes exon 41 and truncates the C-terminus beyond the EF-hand, while $Ca_V1.3_{43i}$ deletes the constitutive “intron” in exon 43 and removes the DCRD of $Ca_V1.3_{42}$. Length altering $Ca_V1.3_{\Delta 44}$ and $Ca_V1.3_{48a-}$ splice variants shortened the length between PCRD and DCRD, and may hence remove the secondary structures critical for CTM interaction with the proximal C-terminus. All four splice variants may modulate CTM function and affect inactivation properties of the channel. In order to characterize these splice variants, the sequence alterations in these exons were genetically engineered into the C-terminus sequence of $Ca_V1.3_{42}$ constructs, and compared against this predominant isoform.

To assess the *I-V* relationship of the channels, transfected cells were similarly depolarized to a family of test potentials of -70 to 60 mV, in steps of 10 mV increments, from a holding potential of -90 mV (Figure 4.6B). The current trace profile for $Ca_V1.3_{43i}$ displayed a slower inactivating I_{Ba} compared to $Ca_V1.3_{A2123V}$ (Figure 4.4D, grey traces) or the other three splice variants (Figure 4.6C, grey traces), but showed an early and much pronounced inactivation of I_{Ca} (Figure 4.4D and 4.6C, black traces).

All splice variants except for $Ca_V1.3_{\Delta 41}$ activated at more negative potentials as observed by the hyperpolarized shift in $V_{½\ act}$ in both Ba^{2+} ($Ca_V1.3_{43i}$, by 8.01 mV; $Ca_V1.3_{\Delta 44}$, by 9.45 mV; $Ca_V1.3_{48a-}$, by 11.22 mV; Table 4.2) and Ca^{2+} ($Ca_V1.3_{43i}$, by 7.07 mV; $Ca_V1.3_{\Delta 44}$, by 12.29 mV; $Ca_V1.3_{48a-}$, by 10.32 mV; Table 4.3) with respect to $Ca_V1.3_{A2123V}$ ($p < 0.01$; unpaired *t*-test). This shift is predominantly caused by a decrease in the slope of activation k_{act} (Ba^{2+}: $Ca_V1.3_{43i}$, 2.74; $Ca_V1.3_{\Delta 44}$, by 1.83; $Ca_V1.3_{48a-}$, by 2.92; Table 4.2; Ca^{2+}: $Ca_V1.3_{43i}$, 1.67; $Ca_V1.3_{\Delta 44}$, by 1.19; $Ca_V1.3_{48a-}$, by 1.29; Table 4.3). $Ca_V1.3_{\Delta 41}$ displayed a slight, although statistically significant ($p <$ 0.001; unpaired *t*-test), depolarized shift in $V_{½\ act}$ by 3.96 mV in Ba^{2+} and 0.91mV in Ca^{2+}, with a slight increase in the slope of activation (k_{act}, increased by 0.66 in Ba^{2+}).

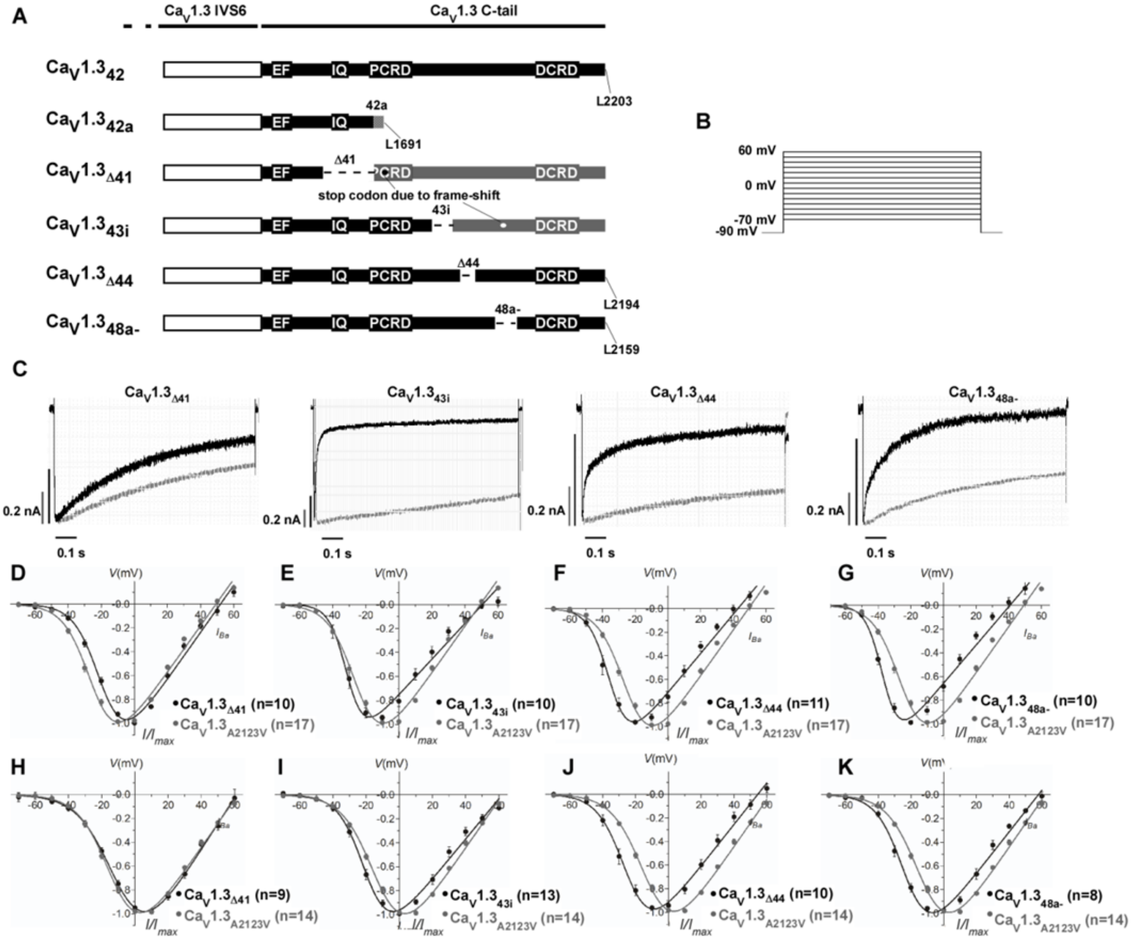

Figure 4.6 Current-voltage relationships of Ca$_V$1.3 alternatively spliced variants. *A*, schematic representation of alternatively spliced variant constructs. The channel backbone consists of Ca$_V$1.3 (GenBank Accession number: D38101, white box) while the cytosolic tail consist of Ca$_V$1.3 long form (Ca$_V$1.3$_{42}$), or alternatively spliced variants Δ41, 43i, Δ44 and 48a- (black). The stop codons for Δ 41 and 43i are indicated by black and white filled circles, respectively. Numberings follow the Ca$_V$1.3 amino acid sequence. *B*, voltage protocol for determining *I-V* relationship. 400 ms depolarisations to potentials ranging, in 10 mV increments, from -80 to 60 mV (holding potential -90 mV). *C*, representative I_{Ba} (grey) and I_{Ca} (black) traces during depolarization to 10 mV. The I_{Ba} and I_{Ca} traces were scaled to enable comparison between the two profiles. Current scales were drawn for both I_{Ba} (grey) and I_{Ca} (black). The time scales for each I_{Ba} and I_{Ca} pair are the same. *D-G*, normalized *I-V* plots for I_{Ba} of alternatively spliced constructs Δ41, 43i, Δ44 and 48a-. The curves were fitted with the equation described in methods. In paratheses are the number of cells recorded. *H-K*, same as *D-G*, but for I_{Ca}.

42a, 43i, Δ44 and 48a- splice variant showed narrowing and pronounced negative shift in window current

In the *I-V* curves, $Ca_V1.3_{42a}$ displayed a pronounced shift in the hyperpolarized direction, indicating a more negatively activating channel than $Ca_V1.3_{A2123}$. The four novel splice variants also resulted in *I-V* shifts. To enable a more accurate assessment of the voltage activation of these channels, we analysed the tail currents (*G*) obtained at the end of a short depolarizing pulse to various potentials (Figure 4.7A). In addition, to determine the inactivation properties of the channels under steady-state conditions, transfected cells were held at various potentials for 15-sec and currents evoked before and after the inactivating pulse were compared (Figure 4.7B). The data obtained are displayed in Figure 4.7 and Table 4.2.

Compared to $Ca_V1.3_{A2123V}$, the voltage of half-maximal activation in $Ca_V1.3_{42a}$ was shifted by -19.94 mV ($V_{½\ act}$, $Ca_V1.3_{A2123V}$, -10.50 ± 0.95 mV, $n = 8$; $Ca_V1.3_{42a}$, -30.44 ± 0.84, $n = 5$; $p < 0.001$, unpaired *t*-test). The slope of $Ca_V1.3_{42a}$ was steeper, reflected by the decrease in k_{act} ($Ca_V1.3_{42}$: 15.13 ± 0.91; $Ca_V1.3_{42a}$: 8.57 ± 0.74; $p < 0.001$, unpaired *t*-test). Splicing of exon 42a caused a minor but significant shift in the voltage for half-maximal steady-state inactivation ($V_{½\ inact}$, $Ca_V1.3_{A2123V}$, -44.24 ± 0.47 mV, $n = 7$; $Ca_V1.3_{42a}$, -40.70 ± 0.79, $n = 7$; $p < 0.001$, unpaired *t*-test) but gave rise to a slightly steeper SSI slope, decreasing the k_{inact} by 1.12 ($k_{\ inact}$, $Ca_V1.3_{A2123V}$, 5.90 ± 0.40, $n = 7$; $Ca_V1.3_{42a}$, -4.79 ± 0.71, $n = 6$; $p < 0.001$, unpaired *t*-test). Put together, $Ca_V1.3_{42a}$ resulted in a window current that is more hyperpolarized than $Ca_V1.3_{A2123V}$ (Figure 4.7D). The large negative shift in $V_{½\ act}$ coupled with a minute change in $V_{½\ inact}$ also resulted in a narrowing of the window current.

Just as in the *I-V* analyses, the novel splice variants displayed a hyperpolarized shift in $V_{½\ \mathrm{act}}$ of the tail current analyses compared to $\mathrm{Ca_V1.3_{A2123V}}$. The changes observed here were also significant ($V_{½\ \mathrm{act}}$, $\mathrm{Ca_V1.3_{\Delta41}}$, -12.68 ± 0.57, $n = 7$; $\mathrm{Ca_V1.3_{43i}}$, -32.24 ± 0.57, $n = 5$; $\mathrm{Ca_V1.3_{\Delta44}}$, -28.75 ± 0.88, $n = 7$; $\mathrm{Ca_V1.3_{48a-}}$, -28.72 ± 0.65, $n = 9$; $p < 0.001$ unpaired *t*-test). The activation slope factors for the splice variants were significantly smaller than $\mathrm{Ca_V1.3_{A2123V}}$ (k_{act}, $\mathrm{Ca_V1.3_{\Delta41}}$, 10.72 ± 0.51; $\mathrm{Ca_V1.3_{43i}}$, 7.59 ± 0.50; $\mathrm{Ca_V1.3_{\Delta44}}$, 10.23 ± 0.78; $\mathrm{Ca_V1.3_{48a-}}$, 9.19 ± 0.65, $p < 0.001$, unpaired *t*-test). In addition, all four splice variants had small shifts in $V_{½\ \mathrm{inact}}$ ($\mathrm{Ca_V1.3_{\Delta41}}$, -41.05 ± 0.63 mV; $\mathrm{Ca_V1.3_{43i}}$, -42.02 ± 0.31; $\mathrm{Ca_V1.3_{\Delta44}}$, -46.57 ± 1.10; $p < 0.05$; $\mathrm{Ca_V1.3_{48a-}}$, -45.80 ± 0.69; $p < 0.001$; compared to $\mathrm{Ca_V1.3_{A2123V}}$, unpaired *t*-test)

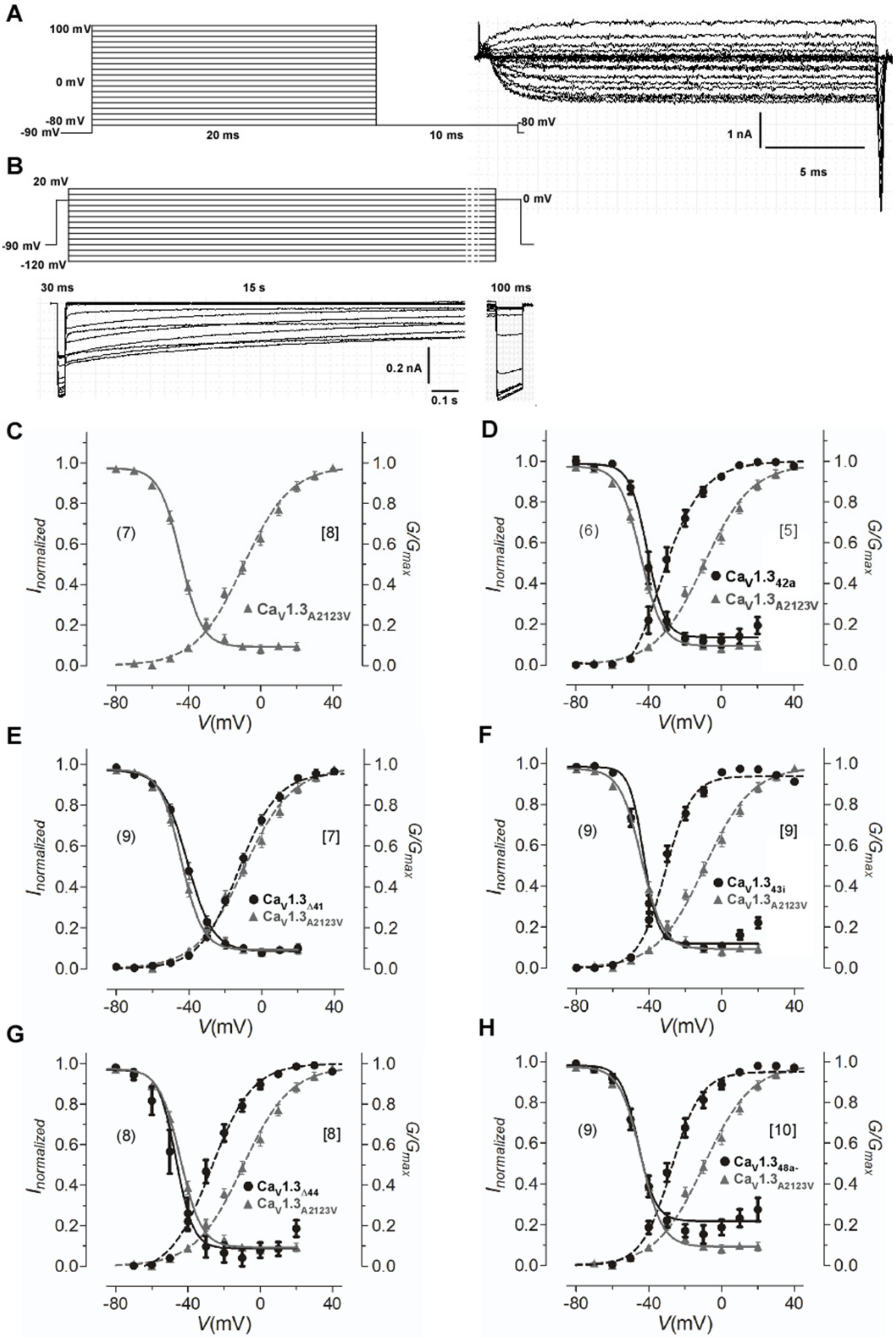
A
100 mV
0 mV
-80 mV
-90 mV
20 ms
10 ms
-80 mV
1 nA
5 ms
B
20 mV
-90 mV
-120 mV
0 mV
30 ms
15 s
100 ms
0.2 nA
0.1 s
C
(7)
[8]
Ca$_V$1.3$_{A2123V}$
D
(6)
[5]
Ca$_V$1.3$_{42a}$
Ca$_V$1.3$_{A2123V}$
E
(9)
[7]
Ca$_V$1.3$_{\Delta41}$
Ca$_V$1.3$_{A2123V}$
F
(9)
[9]
Ca$_V$1.3$_{43i}$
Ca$_V$1.3$_{A2123V}$
G
(8)
[8]
Ca$_V$1.3$_{\Delta44}$
Ca$_V$1.3$_{A2123V}$
H
(9)
[10]
Ca$_V$1.3$_{48a-}$
Ca$_V$1.3$_{A2123V}$
$I_{normalized}$
G/G_{max}
0.0
0.2
0.4
0.6
0.8
1.0
-80
-40
0
40
V(mV)

Figure 4.7 Activation and steady-state inactivation properties of $Ca_V1.3$ alternatively spliced variants. *A*, voltage protocol used for determining activation properties and an exemplar current trace ($Ca_V1.3_{A2123V}$). Tail currents were measured after 20 ms depolarisation to potentials ranging from -80 to 100 mV, in 10 mV steps. *B*, voltage protocol used for determining steady-state inactivation, SSI, properties and an exemplar current trace ($Ca_V1.3_{A2123V}$). Currents evoked at 10 mV test potentials were measured before and after 15 s depolarisations to potentials ranging from -120 to 20 mV, in 10 mV steps. A holding potential of -90 mV was maintained for all experiments. *C-H*, normalized plots for activation (dashed lines) and SSI (solid lines) for long form ($Ca_V1.3_{A2123V}$), short form ($Ca_V1.3_{42a}$), and alternatively spliced constructs Δ41, 43i, Δ44 and 48a-. For SSI, peak currents obtained after the 15 s inactivating pulse were normalized to that obtained before inactivation and plotted against voltage. The curves are fitted with the Boltzmann relationship. For the activation plots, the peak of the tail currents (G) were normalized against the largest peak and plotted against voltage. The curves were fitted using the equation given in methods. The number of cells recorded are given in paratheses; "( )" for SSI and "[ ]" for activation. Plots of long form ($Ca_V1.3_{A2123V}$) were redrawn in each graph for comparison.

Table 4.2 Comparison of I_{Ba} electrophysiological properties of $Ca_V1.3$ channels containing long form ($Ca_V1.3_{A2123V}$), short form ($Ca_V1.3_{42}$), and splice variants Δ41, 43i, Δ44 and 48a-.

Construct	*I - V*			*G - V*		*SSI*	
	V_{rev} (mV)	$V_{1/2\ act}$ (mV)	k_{act}	$V_{1/2\ act}$ (mV)	k_{act}	$V_{1/2\ inact}$ (mV)	k_{inact}
$Ca_V1.3_{A2123V}$	49.29 ± 0.61	-24.33 ± 0.49	-8.03 ± 0.49	-10.50 ± 0.95	15.13 ± 0.91	-44.24 ± 0.47	5.90 ± 0.40
$Ca_V1.3_{42a}$	41.59 ± 0.79^{c}	-35.55 ± 0.53^{c}	-5.60 ± 0.40^{c}	-30.44 ± 0.84^{c}	8.57 ± 0.74^{c}	-40.7 ± 0.79^{c}	4.79 ± 0.71^{c}
$Ca_V1.3_{\Delta41}$	52.85 ± 0.61^{c}	-20.37 ± 0.48^{c}	-7.37 ± 0.33^{c}	-12.68 ± 0.57^{c}	10.72 ± 0.51^{c}	-41.05 ± 0.63^{c}	-7.03 ± 0.55^{c}
$Ca_V1.3_{43i}$	48.20 ± 1.22^{b}	-32.34 ± 0.61^{c}	-4.82 ± 0.47^{c}	-32.24 ± 0.57^{c}	7.59 ± 0.50^{c}	-43.02 ± 0.31^{c}	3.89 ± 0.23^{c}
$Ca_V1.3_{\Delta44}$	41.59 ± 0.81^{c}	-33.78 ± 0.60^{c}	-5.64 ± 0.45^{c}	-28.75 ± 0.88^{c}	10.23 ± 0.78^{c}	-46.57 ± 1.10^{c}	-4.83 ± 0.88^{c}
$Ca_V1.3_{48a-}$	42.04 ± 0.74^{c}	-35.39 ± 0.49^{c}	-5.34 ± 0.37^{c}	-28.72 ± 0.65^{c}	9.19 ± 0.65^{c}	-45.80 ± 0.69^{c}	-4.82 ± 0.57^{c}

^{a} $p < 0.05$, ^{b} $p < 0.01$, ^{c} $p < 0.001$, compared to $Ca_V1.3_{A2123V}$ (unpaired *t* test). Values shown are mean ± SEM.

Table 4.3 Comparison of I_{Ca} electrophysiological properties of $Ca_V1.3$ channels.

Construct	*I - V*		
	V_{rev} (mV)	$V_{1/2\ act}$ (mV)	k_{act}
$Ca_V1.3_{A2123V}$	62.12 ± 0.72	-12.28 ± 0.53	-9.39 ± 0.30
$Ca_V1.3_{42a}$	58.61 ± 0.73^{c}	-23.15 ± 0.39^{c}	-6.82 ± 0.27^{c}
$Ca_V1.3_{\Delta41}$	62.21 ± 0.90	-11.37 ± 0.71^{c}	-9.61 ± 0.40
$Ca_V1.3_{43i}$	57.89 ± 1.18	-22.60 ± 0.74^{c}	-8.1 ± 0.48^{c}
$Ca_V1.3_{\Delta44}$	62.12 ± 0.72^{c}	-12.28 ± 0.53^{c}	-9.39 ± 0.30^{c}
$Ca_V1.3_{48a-}$	58.61 ± 0.73^{c}	-23.15 ± 0.39^{c}	-8.10 ± 0.48^{c}

^{a} $p < 0.05$, ^{b} $p < 0.01$, ^{c} $p < 0.001$, compared to $Ca_V1.3_{A2123V}$ (unpaired *t* test). Values shown are mean ± SEM.

Table 4.4 Comparison of the kinetics of recovery from inactivation in Ba^{2+}.

Construct	τ_f (s)	τ_s (ms)
$Ca_V1.3_{A2123V}$	0.61 ± 0.12	7.74 ± 2.97
$Ca_V1.3_{42a}$	0.76 ± 0.22^{c}	20.84 ± 7.45^{c}
$Ca_V1.3_{\Delta41}$	0.63 ± 0.11^{c}	7.65 ± 2.42^{c}
$Ca_V1.3_{43i}$	0.44 ± 0.09^{c}	7.08 ± 2.86^{c}
$Ca_V1.3_{\Delta44}$	0.40 ± 0.09^{c}	24.07 ± 10.05^{c}
$Ca_V1.3_{48a-}$	0.53 ± 0.12^{c}	8.51 ± 3.69^{c}

^{a} $p < 0.05$, ^{b} $p < 0.01$, ^{c} $p < 0.001$, compared to $Ca_V1.3_{A2123V}$ (unpaired *t* test). Values shown are mean ± SEM.

Calcium-dependent inactivation (CDI) is augmented by 42a, 43i, Δ44 and 48a-splicing

From the profiles of the exemplary traces in Figure 4.6C, it is clear that all four novel splice variants are functional and exhibit CDI, although $Ca_V1.3_{\Delta 41}$ may have very much diminished CDI as compared to $Ca_V1.3_{42a}$. To quantify the degree of CDI exhibited by the channels, the fraction of current that remained at a given time point after depolarization (residual current; i.e. r_{30} and r_{300} for 30 and 300 ms, respectively; Figure 4.8A-T) to different voltages was determined for all four constructs. The difference between the residual current at 0 mV (f_0; Figures 4.8Q-T) was obtained as a measure of CDI strength.

As expected, deletion of exon 41 in $Ca_V1.3_{\Delta 41}$, which removed the entire IQ motif, resulted in very small degree of inactivation by Ca^{2+} even at 300 ms (f_0, 30 ms, 0.03 ± 0.01; 50 ms, 0.04 ± 0.02; 100 ms, 0.09 ± 0.02, 200 ms, 0.14 ± 0.03, 300 ms, 0.17 ± 0.03).

Surprisingly, alternative splicing of exon 43 in $Ca_V1.3_{43i}$, which caused a frame-shift and incorporation of 179 unrelated a.a. after the splice junction, exhibited a very pronounced CDI, comparable to that of $Ca_V1.3_{42a}$ (Figure 4.9). Furthermore, for $Ca_V1.3_{\Delta 44}$ and $Ca_V1.3_{48a-}$, like $Ca_V1.3_{42a}$, the residual currents at time points measured for Ca^{2+} exhibited a U-shaped dependence on voltage (Figure 4.8C-D, 4.8G-H, 4.8K-L, 4.8O-P, and 4.8S-T). However, $Ca_V1.3_{\Delta 44}$ and $Ca_V1.3_{48a-}$ had a smaller f_0 than $Ca_V1.3_{42a}$ (Figure 4.9). It is plausible that the secondary structures changes brought about by these splice variants may affect the efficacy of interaction between the DCRD and the calcium-sensing apparatus.

Voltage-dependent inactivation (VDI) remained suppressed with C-terminal alternative splicing

An appreciable degree of slow inactivation in the absence of Ca^{2+} is apparent in the current trace profiles in Figure 4.4D as well as the residual current plots in Figure 4.5A for $Ca_V1.3_{A2123V}$. We now consider if voltage-dependent inactivation (VDI) may be modulated by alternative splicing in the C-terminus. Figure 4.10 shows the percentage inactivation of peak I_{Ba} evoked at V_{max}, as it decays over various time points. Inactivation of I_{Ba} through $Ca_V1.3_{A2123V}$ increased steadily over time; displaying 2.65 ± 3.53% inactivation at 30 ms after depolarization, 4.97 ± 1.25% at 100 ms and reaching 10.80 ± 2.07% by the end of 300 ms. Inactivation of I_{Ba} through $Ca_V1.3_{\Delta 41}$ occurred at a similar pace (Fig 4.10) and was statistically indistinguishable from $Ca_V1.3_{A2123V}$ ($p > 0.05$, Kruskal-Wallis test). Effect of truncation of the distal C-terminus by 42a and 43i splicing on VDI could not be determined as the percentage inactivation of peak I_{Ba} relative to $Ca_V1.3_{A2123V}$ differs at the various time points, and were statistically indistinguishable. However, the general trend of increased percentage inactivation with prolonged depolarization was conserved in all splice variants, albeit at different rates (Fig 4.10).

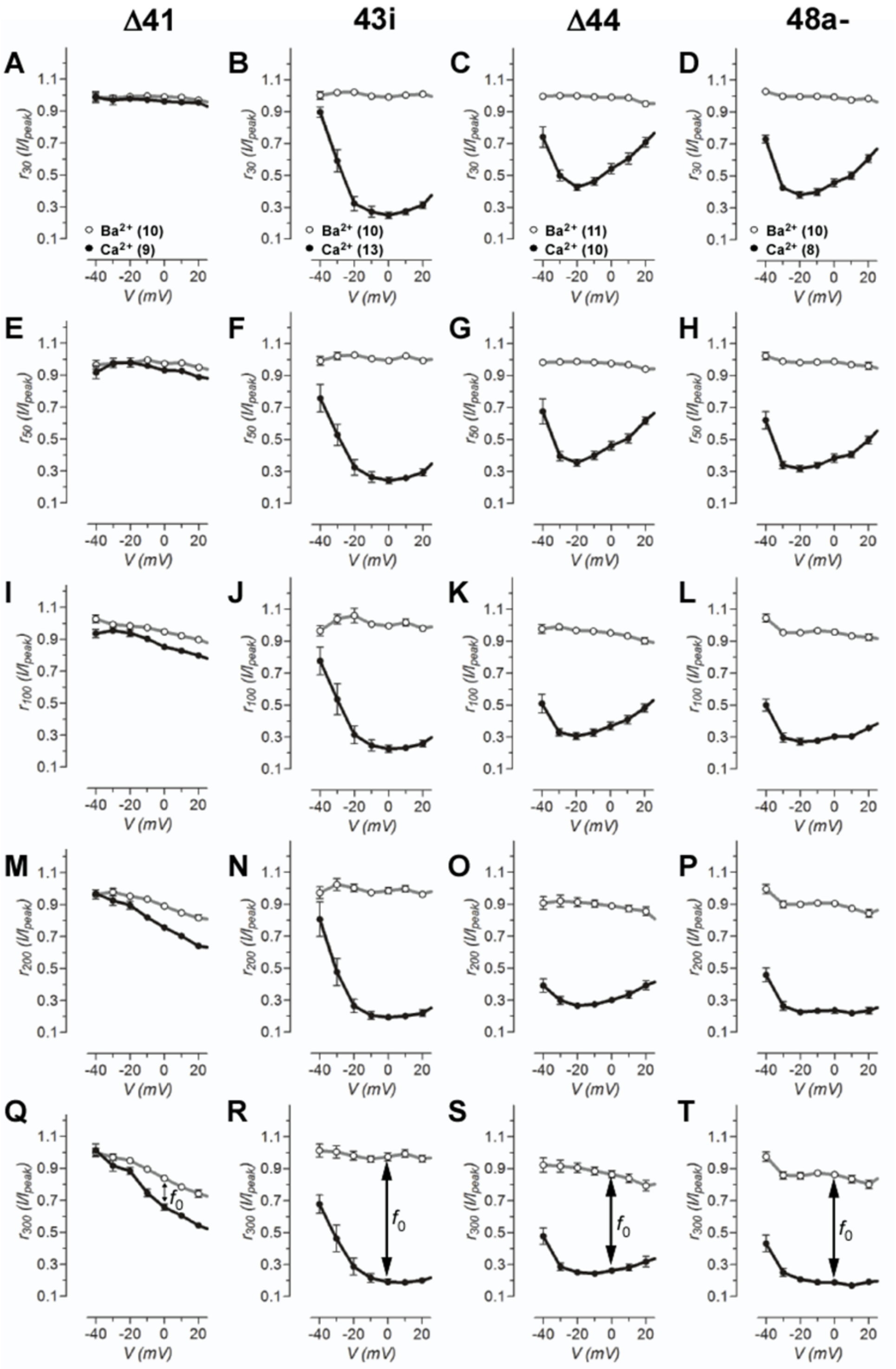

Figure 4.8 Calcium-dependent inactivation of current through Ca$_V$1.3 splice variants Δ41, 43i, Δ44 and 48a-. *A-D*, the fraction of peak current, I_{peak}, that remained at 30 ms upon depolarisation to the indicated voltages, r_{30}. The difference between the remaining current for I_{Ba} and I_{Ca}, f-value, indicates the strength of calcium-dependent inactivation, CDI. The curves are visual fits of the values plotted to facilitate comparison. The number of cells recorded is given in parentheses. *E-H*, the fraction of peak current, I_{peak}, that remained at 50 ms upon depolarisation to the indicated voltages, r_{50}. *I-L*, the fraction of peak current, I_{peak}, that remained at 100 ms upon depolarisation to the indicated voltages, r_{100}. *M-P*, the fraction of peak current, I_{peak}, that remained at 200 ms upon depolarisation to the indicated voltages, r_{200}. *Q-T*, the fraction of peak current, I_{peak}, that remained at 300 ms upon depolarisation to the indicated voltages, r_{300}.

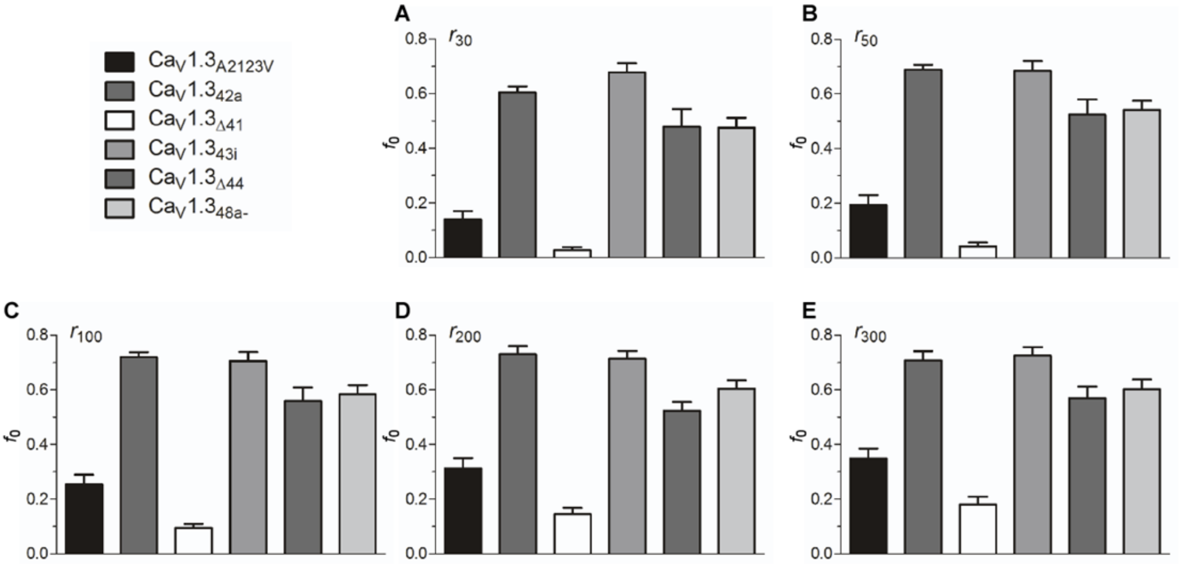

Figure 4.9 Strength of calcium-dependent inactivation in Ca$_V$1.3$_{A2123V}$, Ca$_V$1.3$_{42a}$ and splice variants Δ41, 43i, Δ44 and 48a-. A quantifier for the amount of CDI exhibited by each channel is represented by f_{10}, the difference in levels of remaining I_{Ba} and I_{Ca} currents evoked by 10 mV. *A-E*, f_{10} for r_{30}, r_{50}, r_{100}, r_{200}, and r_{300}, respectively.

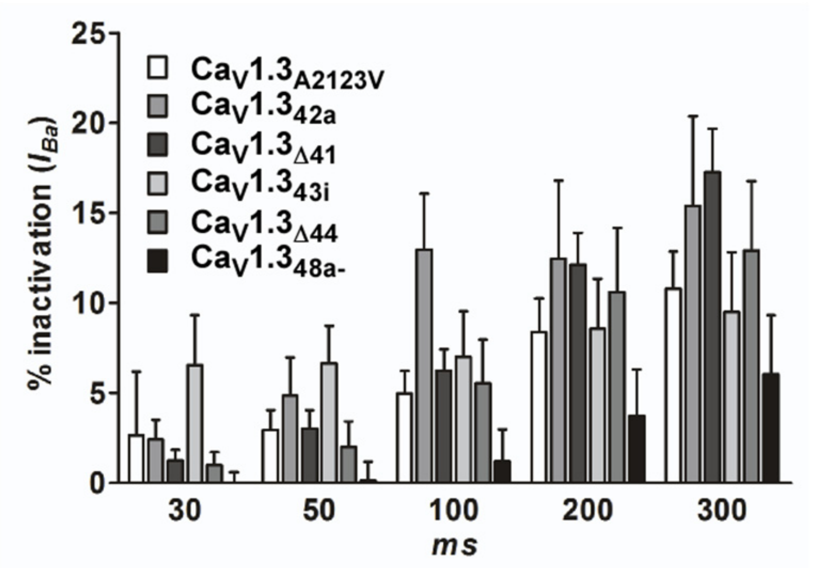

Figure 4.10 Voltage-dependent inactivation of current through Ca$_V$1.3$_{A2123V}$, Ca$_V$1.3$_{42a}$ and splice variants Δ41, 43i, Δ44 and 48a-. The level of voltage-independent inactivation of the channel is represented as a percentage of I_{Ba} inactivation during depolarization to V_{max} in the time course indicated. The numbers of cells recorded are Ca$_V$1.3$_{A2123V}$: 17, Ca$_V$1.3$_{42a}$: 13, Ca$_V$1.3$_{43i}$:17, Ca$_V$1.3$_{\Delta 44}$: 14, Ca$_V$1.3$_{48a-}$: 17. *, $p < 0.05$ (compared to Ca$_V$1.3$_{A2123V}$) (Kruskal-Wallis test followed by Dunn's multiple-comparison post-test).

Rapid recovery from inactivation maintained in C-terminal splice variants

The recovery of the channels were determined using a two-pulse protocol whereby a conditioning pre-pulse of 2-sec was followed by a test-pulse after a given time interval (*ΔT*) has elapsed (Figure 4.11A). Recovery was expressed as the dependence of the maximal current obtained the test-pulse, as a fraction of the maximal current at pre-pulse, on the time-interval between the pulses (Figure 4.11C).

The recovery of the channels, here, may be described as occurring in two-phases: a fast recovery phase ($\Delta T \approx$ 0-40 ms) and a slow recovery phase ($\Delta T \approx$ 60 ms onwards). In $Ca_V1.3_{A2123V}$, recovery began rapidly and about 56% of the channels recovered by 20 ms, near the beginning of the slow phase. However, the subsequent rate of recovery was decreased and only ~82% of channels recovered at the end of 2-sec (Figure 4.11C). Increasing the time interval up to 4 s still could not bring about a complete recovery of all the channels (~85% recovered; data not shown). $Ca_V1.3_{42a}$ exhibited a slower rate of recovery compared to $Ca_V1.3_{A2123V}$ (Figure 4.11C. τ_f, $Ca_V1.3_{A2123V}$, 7.74 ± 2.97 ms; $Ca_V1.3_{42a}$, 20.84 ± 7.45 ms; $p = 0.06$, unpaired *t* test). About 60% of $Ca_V1.3_{42a}$ channels had recovered by the early part of the slow phase at 100 ms. At 2-sec, the late part of the slow phase saw only ~71% recovery in $Ca_V1.3_{42a}$ while ~82% of $Ca_V1.3_{A2123V}$ had already recovered. The plot of the recovery data at the slow phase of $Ca_V1.3_{42a}$ fitted into a slightly more gentle slope than $Ca_V1.3_{A2123V}$ (τ_s, $Ca_V1.3_{A2123V}$, 0.61 ± 0.12 s; $Ca_V1.3_{42a}$, 0.76 ± 0.22 s; $p = 0.28$, unpaired *t* test).

$Ca_V1.3_{\Delta 41}$ displayed a similar recovery profile as $Ca_V1.3_{A2123V}$ (Figure 4.11D), reflected in the similar slope values of the fast and slow phase (Table 4.4).

$Ca_V1.3_{43i}$, like $Ca_V1.3_{A2123V}$, began with rapid recovery at the early part of the slow phase, where ~66% of the channels had recovered by 100 ms (Figure 4.11E).

Despite the slightly more gentle slope than $Ca_V1.3_{A2123V}$ at the late slow phase, ~81% of channels recovered by 2-sec.

$Ca_V1.3_{\Delta 44}$ started with rapid recovery near the early part of the slow phase, reaching ~60% recovery of channels by 20 ms, respectively (Figure 4.11F). It has a steeper slope than $Ca_V1.3_{A2123V}$ in the fast phase (τ_f, $Ca_V1.3_{A2123V}$, 7.74 ± 2.91 ms; $Ca_V1.3_{\Delta 44}$, 24.07 ± 10.05 ms; $p = 0.06$, unpaired t test) and a gentler slope in the slow phase (τ_s, $Ca_V1.3_{A2123V}$, 0.61 ± 0.12 s; $Ca_V1.3_{\Delta 44}$, 0.40 ± 0.09 s; $p = 0.10$, unpaired t test). Recovery of $Ca_V1.3_{\Delta 44}$ channels reached ~87% by 2-sec in the slow phase, which slightly greater than the ~82% recovery of $Ca_V1.3_{A2123V}$ channels.

$Ca_V1.3_{48a\text{-}}$, like $Ca_V1.3_{A2123V}$, began with rapid recovery at the early part of the slow phase, where ~63% of the channels had recovered by 100 ms (Figure 4.11G). Despite the slightly more gentle slope than $Ca_V1.3_{A2123V}$ at the late slow phase, ~86% of channels recovered by 2-s, which is slightly greater than that of $Ca_V1.3_{A2123V}$ channels.

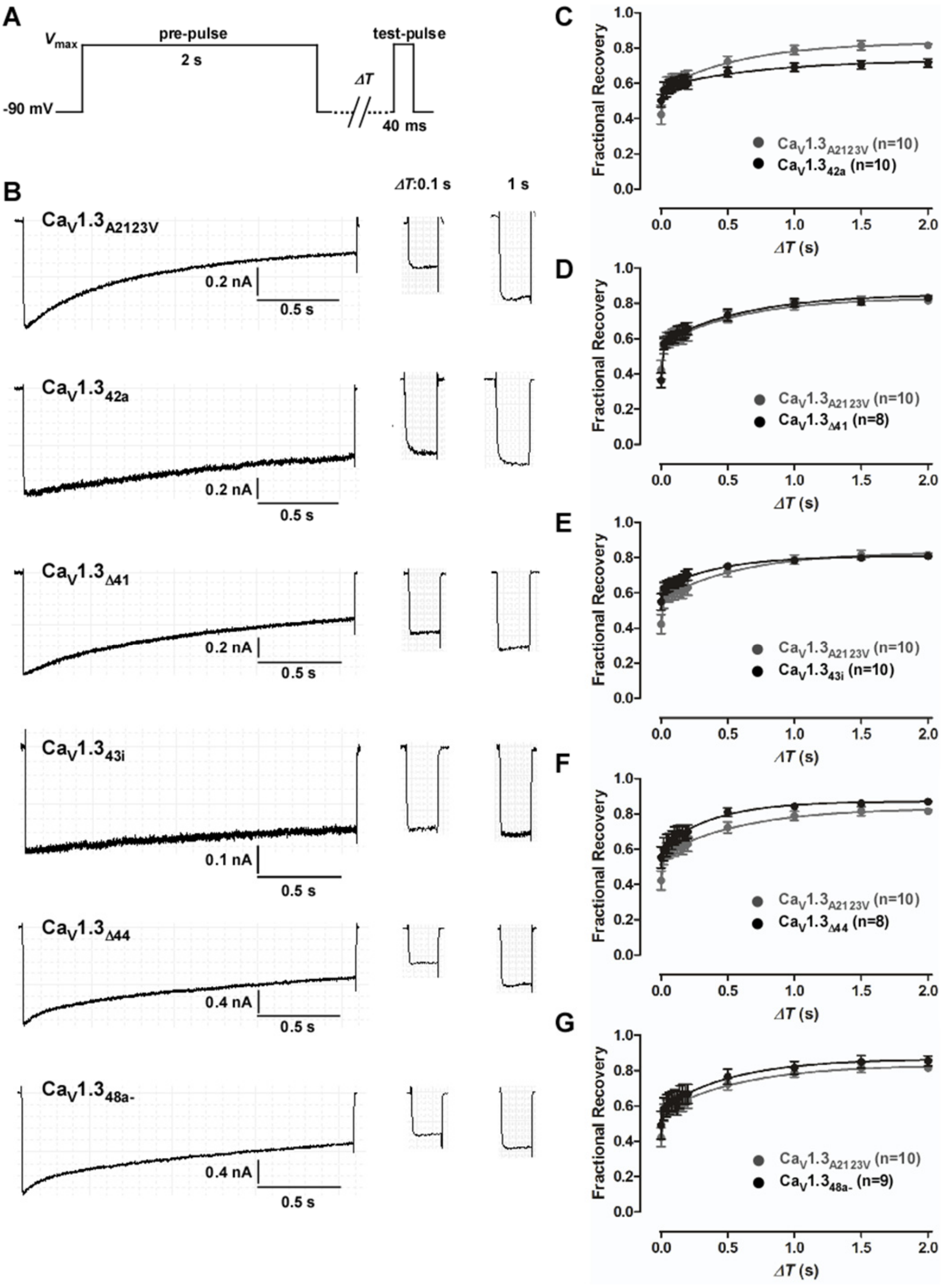

Figure 4.11 Recovery from inactivation in Ca$_V$1.3$_{A2123V}$, Ca$_V$1.3$_{42a}$ and splice variants Δ41, 43i, Δ44 and 48a-. *A*, two-pulse protocol whereby following a 2 sec depolarising pre-pulse to V_{max} (from -90 mV holding potential), a test-pulse is applied after a certain time period, *ΔT*, has elapsed. Peak I_{Ba} measured during the test pulse was expressed as a fraction of peak I_{Ba} obtained at the beginning of the pre-pulse to determine fractional recovery. *B*, representative current traces evoked by the two-pulse protocol. The traces for the test-pulse shown are those obtained with *ΔT* = 0.1 and 1 s. *C*-*G*, fractional recovery plotted as a function of *ΔT* for Ca$_V$1.3$_{A2123V}$, Ca$_V$1.3$_{42a}$ and splice variants Δ41, 43i, Δ44 and 48a-, respectively. The curve for Ca$_V$1.3$_{A2123V}$ was redrawn for all plots for comparison. In parentheses are the numbers of cells recorded. Curves were fitted as described in methods.

Δ41 splice variant mediates 3-fold smaller current density

Previous reports of LTCC with C-terminus deletions had described gross increase in current density as a result ($Ca_V1.2$: Wei et al., (1994); $Ca_V1.1$: Morrill and Cannon (2000); $Ca_V1.3$: Singh et al., (2008)). We hence measured the current density from the novel $Ca_V1.3$ C-terminus splice variants and compared against $Ca_V1.3_{A2123V}$. Figure 4.12 showed that $Ca_V1.3_{42a}$ exhibits a much larger current density compared to the other channels. When evoked at 20 mV, the current density of $Ca_V1.3_{42a}$ was 2.8 times greater than $Ca_V1.3_{A2123V}$ ($Ca_V1.3_{A2123V}$: 88.39 ± 12.48 pA/pF, $Ca_V1.3_{42a}$: 246.81 ± 52.44 pA/pF; $p < 0.001$, Kruskal-Wallis test, followed by Dunn's multiple-comparison post-test). Even when depolarized to -40 mV, the current density was already significantly larger ($Ca_V1.3_{A2123V}$: 8.15 ± 1.29 pA/pF, $Ca_V1.3_{42a}$: 45.89 ± 18.82 pA/pF; $p < 0.01$, Kruskal-Wallis test, followed by Dunn's multiple-comparison post-test). $Ca_V1.3_{\Delta 44}$ and $Ca_V1.3_{48a-}$ also displayed small increases in current density to $Ca_V1.3_{A2123V}$, but these were not statistically significant.

In contrast, the current density of $Ca_V1.3_{\Delta 41}$ was 3.3 times smaller than $Ca_V1.3_{A2123V}$ ($Ca_V1.3_{A2123V}$: 88.39 ± 12.48 pA/pF, $Ca_V1.3_{\Delta 41}$: 26.53 ± 4.22 pA/pF; $p <$ 0.001, Kruskal-Wallis test, followed by Dunn's multiple-comparison post-test). Even when depolarized to -40 mV, the current density was also significantly smaller ($Ca_V1.3_{A2123V}$: 8.15 ± 1.29 pA/pF, $Ca_V1.3_{\Delta 41}$: 2.06 ± 0.30 pA/pF; $p < 0.001$, Kruskal-Wallis test, followed by Dunn's multiple-comparison post-test). $Ca_V1.3_{43i}$ also displayed small, but not statistically significant decrease in current density compared to $Ca_V1.3_{A2123V.}$

Differences observed in current densities could reflect differences in the properties of individual channels including channel open probability and conductance, or might be indicative of differences in the rates of trafficking to or removal from plasma membrane for the Ca$_V$1.3 C-terminal splice variant isoforms. Single-channel electrophysiological would allow us to investigate the biophysical changes in Ca$_V$1.3 splice isoforms at single channel level. Immunohistochemical staining of brain slices using splice-variant-specific antibodies of Ca$_V$1.3$_{42}$ and Ca$_V$1.3$_{42a}$ demonstrated similar staining patterns of these two splice variants. Quantitative real-time PCR of mouse brain and different sub-regions showed that Ca$_V$1.3$_{42}$ was the predominant mRNA isoform, although significant expression of Ca$_V$1.3$_{42a}$ was also observed (cerebellum: 17.1 ± 2.5%; nucleus accumbens: 13.3 ± 1.5%; whole brain: 11.0 ± 0.6%) (Singh et al., 2008). It would be interesting to check if this translates to differences in protein expression, using the splice-variant-specific antibodies.

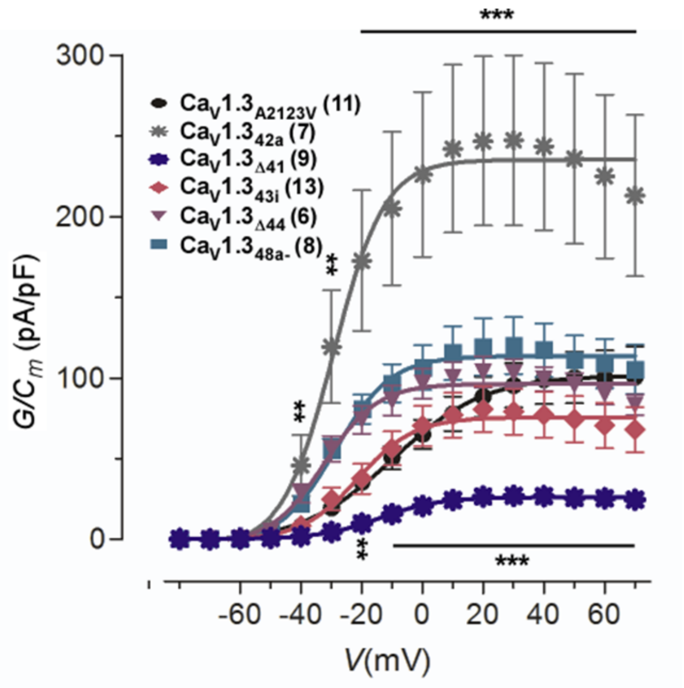

Figure 4.12 Density of Ba^{2+}-currents through Ca$_V$1.3$_{A2123V}$, Ca$_V$1.3$_{42a}$ and splice variants Δ41, 43i, Δ44 and 48a-. The peak of tail currents measured at the end of short depolarising pulses evoked at different potentials were normalized against the membrane capacitance (C$_m$) of the recorded cell to obtain current density. The number of cells recorded in the parentheses. **, $p < 0.01$; ***, $p < 0.001$ (compared to Ca$_V$1.3$_{A2123V}$) (Kruskal-Wallis test followed by Dunn's multiple-comparison post-test).

Soma-dendritic localization maintained in C-terminus splice variants

Immunostaining analysis of primary hippocampal neurons transfected with HA-tagged $Ca_V1.3_{42}$ showed that the channels are mainly localized in the cell bodies and proximal dendrites (Fig 4.13A and Figure 4.14A; green staining), consistent with previous studies (Hell et al., 1993; Zhang et al., 2006). HA-tagged $Ca_V1.3_{42}$ staining observed in the dendrites were fairly diffused, with some cluster formations along the dendrites. In addition, partial co-localization of $Ca_V1.3_{42}$ was observed with synapsin clusters (Fig 4.13A; red staining) and MAP2 (Fig 4.14A; red staining). Shank association with the class I PDZ domain-binding C-terminus motif ITTL in $Ca_V1.3_{42}$ channels is important for its synaptic targeting (Zhang et al., 2005).

Alternative splicing in the C-terminus of $Ca_V1.3$ results in the premature truncations in all the splice variants except $Ca_V1.3_{\Delta 44}$ and $Ca_V1.3_{48a-}$, which also retained the ITTL-motif of $Ca_V1.3_{42}$ channels. To examine if the subcellular localization of the C-terminus splice variants would be affected, they were sub-cloned into the surface epitope-tagged $Ca_V1.3_{42}$ rat plasmid. Both splice variants with intact ITTL-motif, $Ca_V1.3_{\Delta 44}$ and $Ca_V1.3_{48a-}$, a predominantly soma-dendritic localization was observed in the hippocampal neurons (Fig 4.13E-F and Fig 4.14E-F; green staining). In addition, synaptic targeting was maintained as observed by the partial co-localization of HA-tagged channels with synapsin (Fig 4.13E-F, red staining). Surprisingly, truncations of C-terminus that remove the ITTL-motif did not affect membrane expression of splice variants $Ca_V1.3_{42a}$, $Ca_V1.3_{\Delta 41}$ and $Ca_V1.3_{43i}$ at the soma-dendritic regions (Fig 4.13B-D and Fig 4.14B-D; green) Partial co-localization with synapsin clusters and MAP2 was also maintained (Fig 4.13B-D and Fig 4.14B-D; red). This could suggest that additional motifs in the neuronal $Ca_V1.3$ are involved in membrane expression and synaptic target, besides the ITTL motif.

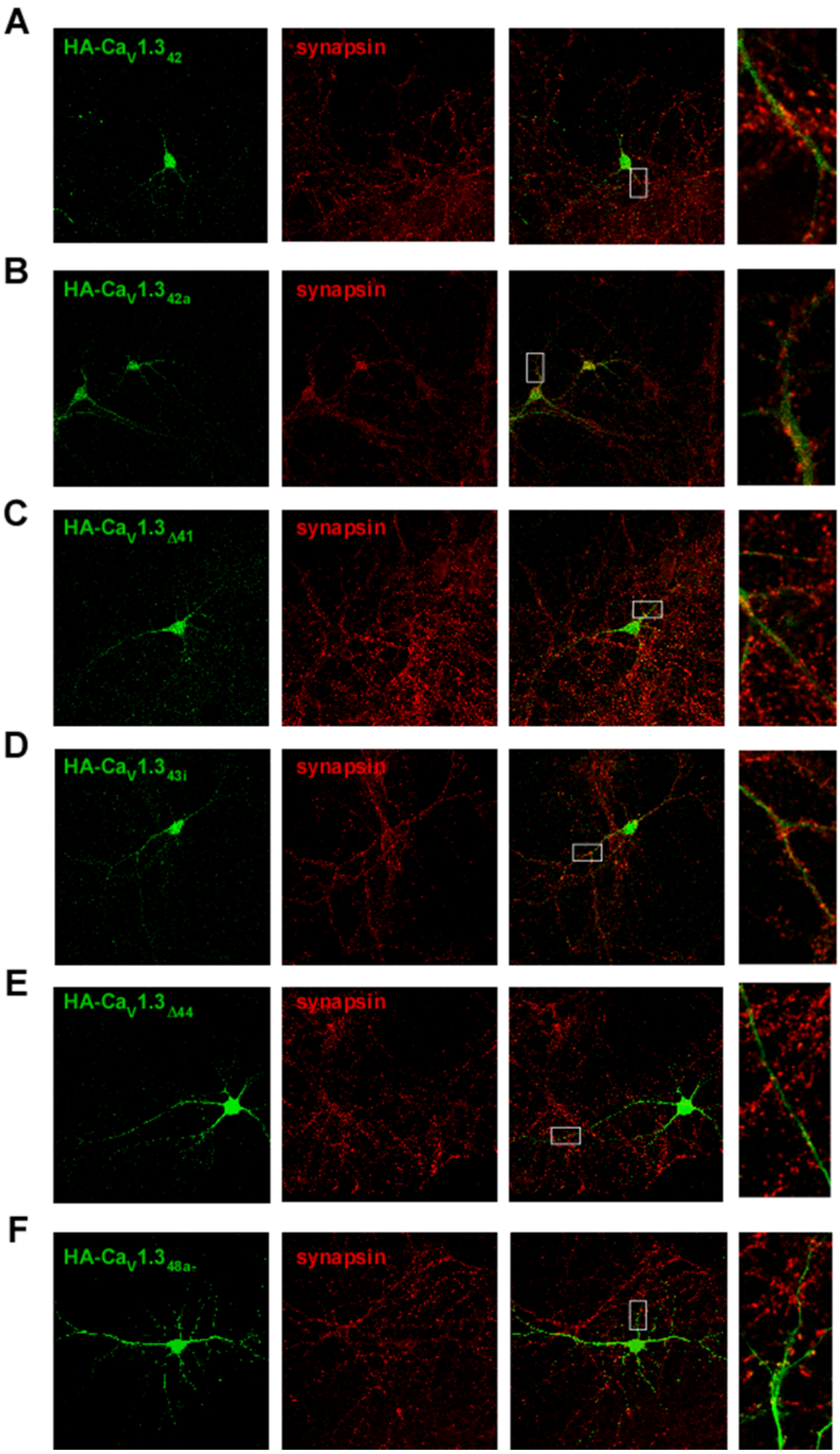

Figure 4.13 Surface localization of HA-tagged Ca$_V$1.3$_{42}$, Ca$_V$1.3$_{42a}$ and splice variants Δ41, 43i, Δ44 and 48a- in hippocampal neurons. *A-F*, synaptic targeting of recombinant HA-tagged Ca$_V$1.3 channels in hippocampal neurons. Hippocampal neurons were transfected with HA-tagged constructs together with β_{2a} and $\alpha_2\delta$ auxiliary subunits at 6-8 DIV and analysed 11-14 days after transfection by anti-HA antibody surface labelling (green) and anti-synapsin (red) immunostaining. *A*, Ca$_V$1.3$_{42}$. *B*, Ca$_V$1.3$_{42a}$. *C*, Ca$_V$1.3$_{\Delta41}$. *D*, Ca$_V$1.3$_{43i}$. *E*, Ca$_V$1.3$_{\Delta44}$. *F*, Ca$_V$1.3$_{48a-}$. The data are representative of three independent transfection experiments with HA-Ca$_V$1.3 constructs.

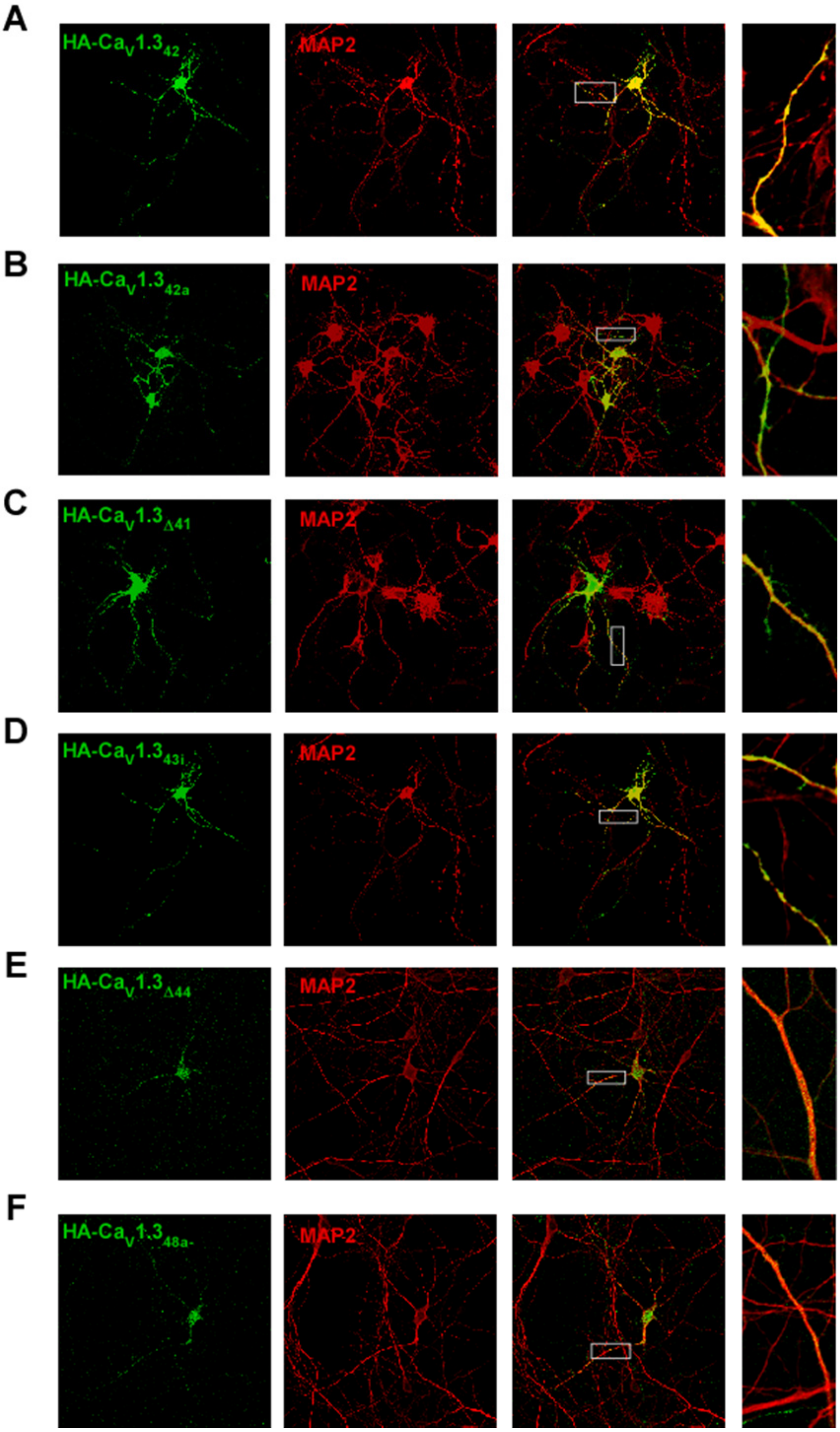

Figure 4.14 Surface localization of HA-tagged Ca$_V$1.3$_{42}$, Ca$_V$1.3$_{42a}$ and splice variants Δ41, 43i, Δ44 and 48a- in hippocampal neurons. *A-F*, synaptic targeting of recombinant HA-tagged Ca$_V$1.3 channels in hippocampal neurons. Hippocampal neurons were transfected with HA-tagged constructs together with β_{2a} and $\alpha_2\delta$ auxiliary subunits at 6-8 DIV and analysed 11-14 days after transfection by anti-HA antibody surface labelling (green) and anti-MAP2 (red) immunostaining. *A*, Ca$_V$1.3$_{42}$. *B*, Ca$_V$1.3$_{42a}$. *C*, Ca$_V$1.3$_{\Delta41}$. *D*, Ca$_V$1.3$_{43i}$. *E*, Ca$_V$1.3$_{\Delta44}$. *F*, Ca$_V$1.3$_{48a-}$. The data are representative of three independent transfection experiments with HA-Ca$_V$1.3 constructs.

4.4 Discussion and Conclusion

Alternative splicing is a pre-mRNA post-transcriptional mechanism that has the potential to expand the proteome exponentially, and is important for modifications in ion channels in response to neuronal input changes. As shown in this study, alternative splicing in the C-terminus of $Ca_V1.3$ alone is extensive, with at least five loci and eight splice variant isoforms identified in rat brain. Correction of the valine-to-alanine cloning error in the rat $Ca_V1.3_{42}$ clone is sufficient to replicate the diminished CDI observed in the human clone (Liu et al., 2010), demonstrating the importance of this conserved residue in the DCRD for CTM function.

Alternative splicing of the C-terminus at exon 41, which removes the IQ motif of the calcium-sensing apparatus, leads to abolishment of CDI, a slight rightward shift in inactivation kinetics and a significant decrease in current density. Alternative splicing in both exons 44 and 48 shortens the distance between the PCRD and DCRD of $Ca_V1.3$ C-terminus, and alters their secondary protein structure via adding or shortening the stretches of alpha helices. Altered efficiency in the interaction between these two domains, and hence CTM function, may cause the slight reduction in CDI in $Ca_V1.3_{\Delta 44}$ and $Ca_V1.3_{48a-}$. Furthermore, a larger inactivation shift and a small activation shift in the hyperpolarizing direction leads to a narrowing of the window current for both splice isoforms relative to $Ca_V1.3_{42}$. No shift in activation was observed between $Ca_V1.3_{42}$ and $Ca_V1.3_{\Delta 44}$ was mentioned briefly in the study by Singh *et al* (2008), possibly due to the human $Ca_V1.3$ clone or the different auxiliary subunits, β_3 used. Truncation of the entire DCRD in $Ca_V1.3_{43i}$ splice isoforms results in CDI of similar intensity as the short variant $Ca_V1.342_a$, as a result of the elimination of CTM function. In all splice variants, the small VDI of $Ca_V1.3$ is maintained, together with the general trend of small increase in VDI with prolonged depolarization.

In addition, alternative splicing in exons 41, 42a, and 43 causes frame shift and premature truncations of the $\mathrm{Ca_V}1.3$ channel protein, thus eliminating the type 1 PDZ-binding motif (ITTL) that is present in the $\mathrm{Ca_V}1.3_{42}$, $\mathrm{Ca_V}1.3_{\Delta 44}$ and $\mathrm{Ca_V}1.3_{½48}$ channels. Selective binding of Shank proteins to the ITTL-motif in neuronal $\mathrm{Ca_V}1.3_{42}$ channels were shown to be critical for its synaptic targeting (Zhang et al., 2005). However, our study of subcellular localization of the splice variants in primary neuronal culture showed that removal of the type 1 PDZ-binding motif did not affect the predominant soma-dendritic expression of $\mathrm{Ca_V}1.3$ channels, or its synaptic targeting. A possible reason could be the different auxiliary subunits used, β_{2a} versus β_3 used in the study by Zhang *et al* (2005), which could affect membrane trafficking and possibly subcellular localization (Arikkath and Campbell, 2003). Furthermore, primary neurons in this study were allowed to differentiate and form mature dendritic spines and synapses, before fixing on DIV 18-21, as compared to the neurons fixed on DIV 12-13 in the study by Zhang et al (2005), which could explain for the differential synaptic clustering results observed.

Chapter 5

Conclusion & Future Studies

5.1 Conclusion

In this thesis, two post-transcriptional events – RNA editing and alternative splicing, in the carboxyl-terminus of L-type calcium channel $Ca_V1.3$ were studied. Firstly, by sequencing analysis of both cDNA and genomic DNA of $Ca_V1.3$, we identified three RNA editing sites in the IQ motif. We confirmed the protein expression of the edited peptides via targeted HPLC-mass chromatography as well as the surface localization in primary neurons via immunocytochemistry. In addition, we identified the enzyme responsible as ADAR2 via sequencing analysis of $ADAR2^{-/-}$ knockout mice. Examination of tissue regions with $Ca_V1.3$ expression, namely the brain, heart, pancreatic islets and cochlea demonstrated that RNA editing of $Ca_V1.3$ is specific to the central nervous system. Furthermore, RNA editing of $Ca_V1.3$ in the brain is developmentally regulated, first appearing in post-natal rodents at P1 and increasing to adult levels by approximately P7.

Secondly, in order to examine the mechanism for tissue-specific and developmentally-regulated RNA editing of $Ca_V1.3$, we utilized cell lines with $Ca_V1.3$ expression for easier manipulation and testing of isolated conditions. Through these studies, we showed that while the ADAR2's catalytic activity and editing levels of GluR-B at R > G site were elevated with glucose metabolism, neuronal differentiation, zinc concentration and ADAR2 overexpression, they were insufficient to cause RNA editing of $Ca_V1.3$. While the higher percent splicing in intron 1 and exon 5a in developing mice could partially explain for the increased editing of $Ca_V1.3$, it could not explain for the tissue-specificity. Expression of essential cofactor IP_6 was similar in both tissues and cell culture systems. A possible mechanism appears to be expression of tissue-specific inhibitors of ADAR2 binding with $Ca_V1.3$

mRNA, as shown by editing of adenosine residues in the synthetic gIQECS construct with overexpression of both ADAR1 and ADAR2 in cell lines.

The second post-transcriptional mechanism examined was alternative splicing. Previous studies of L-type calcium channels showed extensive alterative splicing along the entire channels, and at least three sites have been identified in the C-terminus of $Ca_V1.3$. In this study, we identified alternative splicing at five loci in the C-terminus of $Ca_V1.3$, and the resulting eight splice isoforms, including wild-type variant $Ca_V1.3_{42}$. Biophysical properties of the splice variants were examined by electrophysiological recordings of transfected HEK293 cells. We demonstrated that truncation of the distal C-terminus via alternative splicing removes its modulatory effect, resulting in robust CDI and smaller window current ($Ca_V1.3_{42a}$ and $Ca_V1.3_{43i}$). However, decreasing the length between the PCRD and DCRD only dampens CDI slightly ($Ca_V1.3_{\Delta 44}$ and $Ca_V1.3_{48a-}$). Elimination of the IQ motif in calcium-sensing apparatus abolishes CDI and results in a much smaller current density. In addition, correction of valine-to-alanine mutation in the rat $Ca_V1.3_{42}$ clone is sufficient for replicating the diminished CDI in the human clone, proving that the conserved residue is critical for interaction between PCRD and DCRD. Immunocytochemical analysis of transfected primary neurons showed that splicing of C-terminus and removal of the PDZ-binding motif does not alter the soma-dendritic localization of $Ca_V1.3$, particularly at the synapses.

5.2 Future studies

Through numerous studies, several important criteria for selective A-to-I RNA editing have been delineated – namely, the imperfect fold-back dsRNA structure formed between ECS and editing site, the homo-dimerization of ADAR, and cofactors such as zinc and IP_6 that stabilizes ADAR2's catalytic core, the mechanism for developmental regulation and tissue-specificity of ADAR2 substrates remains uncertain.

Co-expression of pRK5-gIQECS and ADAR2 in mouse insulinoma cells and the resultant RNA editing of its IQ motif suggest that a *cis*-element close to the ECS may bind proteins in a developmentally-regulated and neuron-specific manner. To test this hypothesis, we could use RNA affinity chromatography, a tool for isolating RNA-binding proteins. As sequence-specific RNA-binding proteins often bind their targets with high affinity, we could modify the pRK5-gIQECS to generate a shorter plasmid for *in vitro* transcription, purify the RNA-binding proteins using RNA affinity chromatography and identify them via mass spectrometry. Hence, we could identify RNA-binding proteins that compete and prevent or enhance RNA editing of $Ca_V1.3$ IQ motif.

The A-to-I editing of certain substrates such as GluR-B and $5\text{-}HT_{2C}$ receptor RNA must occur before or simultaneously with splicing, since the dsRNA structure essential for editing mechanism is formed between the exonic editing site and downstream intron sequence (Higuchi et al., 1993; Lomeli et al., 1994). Post-transcriptional processing of most pre-mRNAs requires several common steps, such as 5'-end capping, 3'-end processing and splicing, which have been proposed to be carried out within large nuclear ribonucleoprotein (lnRNP) particles, and isolation of ADAR2 from these particles suggest that editing mechanism in lnRNP complexes may constitute the natural pre-mRNA processing machinery (Raitskin et al., 2001). Hence, splicing and editing may influence on each activity. Using bioinformatics, we could identify possible splicing factors that may bind upstream of the ECS in $Ca_V1.3$

and test whether co-expression of the splicing factors may modulate the level of editing.

Due to the interaction of alternative splicing and editing mechanisms, in the context of extensive alternative splicing in the C-terminus of $Ca_V1.3$ and editing in its IQ motif, it would be wise to characterize the combination and frequency of these two events together. The predominant combination of splicing and editing could narrow down the region of $Ca_V1.3$ C-terminus crucial for these post-transcriptional changes.

$Ca_V1.3$ currents feature prominently in the spontaneous action potentials and Ca^{2+} spikes in the SCN neurons that underlie circadian rhythms (Pennartz et al., 2002; Jackson et al., 2004). In our laboratory, we have demonstrated that in SCN neurons of ADAR2$^{-/-}$/GluR-B$^{R/R}$ mice (Higuchi et al., 2000), both Na^+ spikes and Ca^{2+} spikes fired at lower frequencies, with decreased depolarization rates between Na^+ spikes and shorter half widths of Ca^{2+} spikes, as compared to ADAR2$^{+/+}$/GluR-B$^{R/R}$ control. Furthermore, role of $Ca_V1.3$ channels in driving repetitive activity was shown by the abolishment of Ca^{2+} spikes with nimodipine application. These results suggest that RNA editing of the $Ca_V1.3$ IQ motif diminishes channel CDI, which in turn impacts SCN spike frequency and thereby the central biological clock underlying circadian rhythms. However, one drawback of the ADAR2$^{-/-}$ knockout mice is that ADAR2 targets a wide range of target such as $K_V1.1$ and GluR, which could confound the results observed. In addition, Ca^{2+} entry through LTCCs in DA neurons of the SNc elevate cellular vulnerability to toxins used to create animal models of Parkinson's disease (Chan et al., 2007). In these models, blockage of $Ca_V1.3$ channels underlies the neuroprotective therapeutic effects of DHP antagonist. Hence, it would be interesting to investigate the biophysical impact of RNA editing of $Ca_V1.3$ IQ motif on the SNc DA neurons. Therefore, we propose to identify the important structure determinant such as the ECS, and to generate transgenic ECS$^{-/-}$ mice with abolished editing specifically in the IQ motif of Ca$_V$1.3. This would allow us to investigate the impact of non-editing in Ca$_V$1.3 IQ motif on neurophysiology.

In this study, we have examined alternative splicing of the Ca$_V$1.3 C-terminus in the whole brain. We know that Ca$_V$1.3 channels could have diverse roles in different brain regions, such as modulation of fear, anxiety and depression (McKinney and Murphy, 2006; Busquet et al., 2010) which are often associated with the hippocampus and amygdala. It would be prudent to identify the expression patterns of Ca$_V$1.3 splice variants in specific brain regions, which could drastically affect the channel properties and thus, the firing patterns of neurons in this regions.

References

Arikkath J, Campbell KP (2003) Auxiliary subunits: essential components of the voltage-gated calcium channel complex. Curr Opin Neurobiol 13:298-307.

Baig SM, Koschak A, Lieb A, Gebhart M, Dafinger C, Nurnberg G, Ali A, Ahmad I, Sinnegger-Brauns MJ, Brandt N, Engel J, Mangoni ME, Farooq M, Khan HU, Nurnberg P, Striessnig J, Bolz HJ (2011) Loss of Ca(v)1.3 (CACNA1D) function in a human channelopathy with bradycardia and congenital deafness. Nat Neurosci 14:77-84.

Bass BL (2002) RNA editing by adenosine deaminases that act on RNA. Annu Rev Biochem 71:817-846.

Bezanilla F (2004) RNA editing of a human potassium channel modifies its inactivation. Nat Struct Mol Biol 11:915-916.

Bhalla T, Rosenthal JJ, Holmgren M, Reenan R (2004) Control of human potassium channel inactivation by editing of a small mRNA hairpin. Nat Struct Mol Biol 11:950-956.

Bichet D, Cornet V, Geib S, Carlier E, Volsen S, Hoshi T, Mori Y, De Waard M (2000) The I-II loop of the Ca2+ channel alpha1 subunit contains an endoplasmic reticulum retention signal antagonized by the beta subunit. Neuron 25:177-190.

Bohn G, Moosmang S, Conrad H, Ludwig A, Hofmann F, Klugbauer N (2000) Expression of T- and L-type calcium channel mRNA in murine sinoatrial node. FEBS Lett 481:73-76.

Brusa R, Zimmermann F, Koh DS, Feldmeyer D, Gass P, Seeburg PH, Sprengel R (1995) Early-onset epilepsy and postnatal lethality associated with an editing-deficient GluR-B allele in mice. Science 270:1677-1680.

Busquet P, Nguyen NK, Schmid E, Tanimoto N, Seeliger MW, Ben-Yosef T, Mizuno F, Akopian A, Striessnig J, Singewald N (2010) CaV1.3 L-type Ca2+ channels modulate depression-like behaviour in mice independent of deaf phenotype. Int J Neuropsychopharmacol 13:499-513.

Calin-Jageman I, Yu K, Hall RA, Mei L, Lee A (2007) Erbin enhances voltage-dependent facilitation of Ca(v)1.3 Ca2+ channels through relief of an autoinhibitory domain in the Ca(v)1.3 alpha1 subunit. J Neurosci 27:1374-1385.

Catterall WA (2000) Structure and regulation of voltage-gated Ca2+ channels. Annu Rev Cell Dev Biol 16:521-555.

Catterall WA, Perez-Reyes E, Snutch TP, Striessnig J (2005) International Union of Pharmacology. XLVIII. Nomenclature and structure-function relationships of voltage-gated calcium channels. Pharmacol Rev 57:411-425.

Cenci C, Barzotti R, Galeano F, Corbelli S, Rota R, Massimi L, Di Rocco C, O'Connell MA, Gallo A (2008) Down-regulation of RNA editing in pediatric astrocytomas: ADAR2 editing activity inhibits cell migration and proliferation. J Biol Chem 283:7251-7260.

Chan CS, Guzman JN, Ilijic E, Mercer JN, Rick C, Tkatch T, Meredith GE, Surmeier DJ (2007) 'Rejuvenation' protects neurons in mouse models of Parkinson's disease. Nature 447:1081-1086.

Chilibeck KA, Wu T, Liang C, Schellenberg MJ, Gesner EM, Lynch JM, MacMillan AM (2006) FRET analysis of in vivo dimerization by RNA-editing enzymes. J Biol Chem 281:16530-16535.

Cho DS, Yang W, Lee JT, Shiekhattar R, Murray JM, Nishikura K (2003) Requirement of dimerization for RNA editing activity of adenosine deaminases acting on RNA. J Biol Chem 278:17093-17102.

Christie BR, Schexnayder LK, Johnston D (1997) Contribution of voltage-gated Ca2+ channels to homosynaptic long-term depression in the CA1 region in vitro. J Neurophysiol 77:1651-1655.

Cloues RK, Sather WA (2003) Afterhyperpolarization regulates firing rate in neurons of the suprachiasmatic nucleus. J Neurosci 23:1593-1604.

Dawson TR, Sansam CL, Emeson RB (2004) Structure and sequence determinants required for the RNA editing of ADAR2 substrates. J Biol Chem 279:4941-4951.

Decher N, Streit AK, Rapedius M, Netter MF, Marzian S, Ehling P, Schlichthorl G, Craan T, Renigunta V, Kohler A, Dodel RC, Navarro-Polanco RA, Preisig-Muller R, Klebe G, Budde T, Baukrowitz T, Daut J (2010) RNA editing modulates the binding of drugs and highly unsaturated fatty acids to the open pore of Kv potassium channels. EMBO J 29:2101-2113.

Deisseroth K, Heist EK, Tsien RW (1998) Translocation of calmodulin to the nucleus supports CREB phosphorylation in hippocampal neurons. Nature 392:198-202.

Deisseroth K, Mermelstein PG, Xia H, Tsien RW (2003) Signaling from synapse to nucleus: the logic behind the mechanisms. Curr Opin Neurobiol 13:354-365.

Desterro JM, Keegan LP, Lafarga M, Berciano MT, O'Connell M, Carmo-Fonseca M (2003) Dynamic association of RNA-editing enzymes with the nucleolus. J Cell Sci 116:1805-1818.

Dong K (2007) Insect sodium channels and insecticide resistance. Invert Neurosci 7:17-30.

Ertel EA, Campbell KP, Harpold MM, Hofmann F, Mori Y, Perez-Reyes E, Schwartz A, Snutch TP, Tanabe T, Birnbaumer L, Tsien RW, Catterall WA (2000) Nomenclature of voltage-gated calcium channels. Neuron 25:533-535.

Felix R, Gurnett CA, De Waard M, Campbell KP (1997) Dissection of functional domains of the voltage-dependent Ca2+ channel alpha2delta subunit. J Neurosci 17:6884-6891.

Gallo A, Keegan LP, Ring GM, O'Connell MA (2003) An ADAR that edits transcripts encoding ion channel subunits functions as a dimer. EMBO J 22:3421-3430.

Gamelli AE, McKinney BC, White JA, Murphy GG (2009) Deletion of the L-type calcium channel Ca(V)1.3 but not Ca(V)1.2 results in a diminished sAHP in mouse CA1 pyramidal neurons. Hippocampus.

Gan Z, Zhao L, Yang L, Huang P, Zhao F, Li W, Liu Y (2006) RNA editing by ADAR2 is metabolically regulated in pancreatic islets and beta-cells. J Biol Chem 281:33386-33394.

Gerber A, O'Connell MA, Keller W (1997) Two forms of human double-stranded RNA-specific editase 1 (hRED1) generated by the insertion of an Alu cassette. RNA 3:453-463.

Gray AC, Raingo J, Lipscombe D (2007) Neuronal calcium channels: splicing for optimal performance. Cell Calcium 42:409-417.

Greger IH, Khatri L, Ziff EB (2002) RNA editing at arg607 controls AMPA receptor exit from the endoplasmic reticulum. Neuron 34:759-772.

Greger IH, Khatri L, Kong X, Ziff EB (2003) AMPA receptor tetramerization is mediated by Q/R editing. Neuron 40:763-774.

Gurevich I, Tamir H, Arango V, Dwork AJ, Mann JJ, Schmauss C (2002) Altered editing of serotonin 2C receptor pre-mRNA in the prefrontal cortex of depressed suicide victims. Neuron 34:349-356.

Gurnett CA, De Waard M, Campbell KP (1996) Dual function of the voltage-dependent Ca2+ channel alpha 2 delta subunit in current stimulation and subunit interaction. Neuron 16:431-440.

Guzman JN, Sanchez-Padilla J, Chan CS, Surmeier DJ (2009) Robust pacemaking in substantia nigra dopaminergic neurons. J Neurosci 29:11011-11019.

Hang PN, Tohda M, Matsumoto K (2008) Developmental changes in expression and self-editing of adenosine deaminase type 2 pre-mRNA and mRNA in rat brain and cultured cortical neurons. Neurosci Res 61:398-403.

Hell JW, Westenbroek RE, Warner C, Ahlijanian MK, Prystay W, Gilbert MM, Snutch TP, Catterall WA (1993) Identification and differential subcellular localization of the neuronal class C and class D L-type calcium channel alpha 1 subunits. J Cell Biol 123:949-962.

Helton TD, Horne WA (2002) Alternative splicing of the beta 4 subunit has alpha1 subunit subtype-specific effects on Ca2+ channel gating. J Neurosci 22:1573-1582.

Helton TD, Xu W, Lipscombe D (2005) Neuronal L-type calcium channels open quickly and are inhibited slowly. J Neurosci 25:10247-10251.

Hibino H, Pironkova R, Onwumere O, Vologodskaia M, Hudspeth AJ, Lesage F (2002) RIM binding proteins (RBPs) couple Rab3-interacting molecules (RIMs) to voltage-gated Ca(2+) channels. Neuron 34:411-423.

Higuchi M, Single FN, Kohler M, Sommer B, Sprengel R, Seeburg PH (1993) RNA editing of AMPA receptor subunit GluR-B: a base-paired intron-exon structure determines position and efficiency. Cell 75:1361-1370.

Higuchi M, Maas S, Single FN, Hartner J, Rozov A, Burnashev N, Feldmeyer D, Sprengel R, Seeburg PH (2000) Point mutation in an AMPA receptor gene rescues lethality in mice deficient in the RNA-editing enzyme ADAR2. Nature 406:78-81.

Hofmann F, Lacinova L, Klugbauer N (1999) Voltage-dependent calcium channels: from structure to function. Rev Physiol Biochem Pharmacol 139:33-87.

Hoopengardner B, Bhalla T, Staber C, Reenan R (2003) Nervous system targets of RNA editing identified by comparative genomics. Science 301:832-836.

Huang Z, Li G, Pei W, Sosa LA, Niu L (2005) Enhancing protein expression in single HEK 293 cells. J Neurosci Methods 142:159-166.

Hulme JT, Yarov-Yarovoy V, Lin TW, Scheuer T, Catterall WA (2006) Autoinhibitory control of the CaV1.2 channel by its proteolytically processed distal C-terminal domain. J Physiol 576:87-102.

Ishiuchi S, Tsuzuki K, Yoshida Y, Yamada N, Hagimura N, Okado H, Miwa A, Kurihara H, Nakazato Y, Tamura M, Sasaki T, Ozawa S (2002) Blockage of Ca(2+)-permeable AMPA receptors suppresses migration and induces apoptosis in human glioblastoma cells. Nat Med 8:971-978.

Jackson AC, Yao GL, Bean BP (2004) Mechanism of spontaneous firing in dorsomedial suprachiasmatic nucleus neurons. J Neurosci 24:7985-7998.

Johnson JM, Castle J, Garrett-Engele P, Kan Z, Loerch PM, Armour CD, Santos R, Schadt EE, Stoughton R, Shoemaker DD (2003) Genome-wide survey of human alternative pre-mRNA splicing with exon junction microarrays. Science 302:2141-2144.

Jurkat-Rott K, Lehmann-Horn F (2004) The impact of splice isoforms on voltage-gated calcium channel alpha1 subunits. J Physiol 554:609-619.

Kaech S, Banker G (2006) Culturing hippocampal neurons. Nat Protoc 1:2406-2415.

Kawahara Y, Ito K, Ito M, Tsuji S, Kwak S (2005) Novel splice variants of human ADAR2 mRNA: skipping of the exon encoding the dsRNA-binding domains, and multiple C-terminal splice sites. Gene 363:193-201.

Kawasaki F, Collins SC, Ordway RW (2002) Synaptic calcium-channel function in Drosophila: analysis and transformation rescue of temperature-sensitive paralytic and lethal mutations of cacophony. J Neurosci 22:5856-5864.

Keegan LP, Gallo A, O'Connell MA (2001) The many roles of an RNA editor. Nat Rev Genet 2:869-878.

Keegan LP, Brindle J, Gallo A, Leroy A, Reenan RA, O'Connell MA (2005) Tuning of RNA editing by ADAR is required in Drosophila. EMBO J 24:2183-2193.

Kim U, Wang Y, Sanford T, Zeng Y, Nishikura K (1994) Molecular cloning of cDNA for double-stranded RNA adenosine deaminase, a candidate enzyme for nuclear RNA editing. Proc Natl Acad Sci U S A 91:11457-11461.

Koschak A, Reimer D, Huber I, Grabner M, Glossmann H, Engel J, Striessnig J (2001) alpha 1D (Cav1.3) subunits can form l-type Ca2+ channels activating at negative voltages. J Biol Chem 276:22100-22106.

Krawczak M, Reiss J, Cooper DN (1992) The mutational spectrum of single base-pair substitutions in mRNA splice junctions of human genes: causes and consequences. Hum Genet 90:41-54.

Lai F, Drakas R, Nishikura K (1995) Mutagenic analysis of double-stranded RNA adenosine deaminase, a candidate enzyme for RNA editing of glutamate-gated ion channel transcripts. J Biol Chem 270:17098-17105.

Lai F, Chen CX, Carter KC, Nishikura K (1997a) Editing of glutamate receptor B subunit ion channel RNAs by four alternatively spliced DRADA2 double-stranded RNA adenosine deaminases. Mol Cell Biol 17:2413-2424.

Lai F, Chen CX, Lee VM, Nishikura K (1997b) Dramatic increase of the RNA editing for glutamate receptor subunits during terminal differentiation of clonal human neurons. J Neurochem 69:43-52.

Liang H, DeMaria CD, Erickson MG, Mori MX, Alseikhan BA, Yue DT (2003) Unified mechanisms of Ca2+ regulation across the Ca2+ channel family. Neuron 39:951-960.

Liao P, Yong TF, Liang MC, Yue DT, Soong TW (2005) Splicing for alternative structures of Cav1.2 Ca2+ channels in cardiac and smooth muscles. Cardiovasc Res 68:197-203.

Liao P, Yu D, Li G, Yong TF, Soon JL, Chua YL, Soong TW (2007) A smooth muscle Cav1.2 calcium channel splice variant underlies hyperpolarized window current and enhanced state-dependent inhibition by nifedipine. J Biol Chem 282:35133-35142.

Lipscombe D, Pan JQ, Gray AC (2002) Functional diversity in neuronal voltage-gated calcium channels by alternative splicing of Ca(v)alpha1. Mol Neurobiol 26:21-44.

Lipscombe D, Helton TD, Xu W (2004) L-type calcium channels: the low down. J Neurophysiol 92:2633-2641.

Liu G, Hilliard N, Hockerman GH (2004) Cav1.3 is preferentially coupled to glucose-induced [Ca2+]i oscillations in the pancreatic beta cell line INS-1. Mol Pharmacol 65:1269-1277.

Liu G, Dilmac N, Hilliard N, Hockerman GH (2003a) Ca v 1.3 is preferentially coupled to glucose-stimulated insulin secretion in the pancreatic beta-cell line INS-1. J Pharmacol Exp Ther 305:271-278.

Liu X, Yang PS, Yang W, Yue DT (2010) Enzyme-inhibitor-like tuning of Ca(2+) channel connectivity with calmodulin. Nature 463:968-972.

Liu Z, Ren J, Murphy TH (2003b) Decoding of synaptic voltage waveforms by specific classes of recombinant high-threshold Ca(2+) channels. J Physiol 553:473-488.

Lomeli H, Mosbacher J, Melcher T, Hoger T, Geiger JR, Kuner T, Monyer H, Higuchi M, Bach A, Seeburg PH (1994) Control of kinetic properties of AMPA receptor channels by nuclear RNA editing. Science 266:1709-1713.

Maas S, Patt S, Schrey M, Rich A (2001) Underediting of glutamate receptor GluR-B mRNA in malignant gliomas. Proc Natl Acad Sci U S A 98:14687-14692.

Macbeth MR, Lingam AT, Bass BL (2004) Evidence for auto-inhibition by the N terminus of hADAR2 and activation by dsRNA binding. RNA 10:1563-1571.

Macbeth MR, Schubert HL, Vandemark AP, Lingam AT, Hill CP, Bass BL (2005) Inositol hexakisphosphate is bound in the ADAR2 core and required for RNA editing. Science 309:1534-1539.

Mangoni ME, Couette B, Bourinet E, Platzer J, Reimer D, Striessnig J, Nargeot J (2003) Functional role of L-type Cav1.3 Ca2+ channels in cardiac pacemaker activity. Proc Natl Acad Sci U S A 100:5543-5548.

Marcantoni A, Vandael DH, Mahapatra S, Carabelli V, Sinnegger-Brauns MJ, Striessnig J, Carbone E (2010) Loss of Cav1.3 channels reveals the critical role of L-type and BK channel coupling in pacemaking mouse adrenal chromaffin cells. J Neurosci 30:491-504.

Marshall J, Dolan BM, Garcia EP, Sathe S, Tang X, Mao Z, Blair LA (2003) Calcium channel and NMDA receptor activities differentially regulate nuclear C/EBPbeta levels to control neuronal survival. Neuron 39:625-639.

McKinney BC, Murphy GG (2006) The L-Type voltage-gated calcium channel Cav1.3 mediates consolidation, but not extinction, of contextually conditioned fear in mice. Learn Mem 13:584-589.

Melcher T, Maas S, Herb A, Sprengel R, Seeburg PH, Higuchi M (1996a) A mammalian RNA editing enzyme. Nature 379:460-464.

Melcher T, Maas S, Herb A, Sprengel R, Higuchi M, Seeburg PH (1996b) RED2, a brain-specific member of the RNA-specific adenosine deaminase family. J Biol Chem 271:31795-31798.

Mermelstein PG, Bito H, Deisseroth K, Tsien RW (2000) Critical dependence of cAMP response element-binding protein phosphorylation on L-type calcium channels supports a selective response to EPSPs in preference to action potentials. J Neurosci 20:266-273.

Mittman S, Guo J, Agnew WS (1999) Structure and alternative splicing of the gene encoding alpha1G, a human brain T calcium channel alpha1 subunit. Neurosci Lett 274:143-146.

Mori MX, Erickson MG, Yue DT (2004) Functional stoichiometry and local enrichment of calmodulin interacting with Ca2+ channels. Science 304:432-435.

Morrill JA, Cannon SC (2000) COOH-terminal truncated alpha(1S) subunits conduct current better than full-length dihydropyridine receptors. J Gen Physiol 116:341-348.

Namkung Y, Skrypnyk N, Jeong MJ, Lee T, Lee MS, Kim HL, Chin H, Suh PG, Kim SS, Shin HS (2001) Requirement for the L-type Ca(2+) channel alpha(1D) subunit in postnatal pancreatic beta cell generation. J Clin Invest 108:1015-1022.

Nishikura K (2010) Functions and regulation of RNA editing by ADAR deaminases. Annu Rev Biochem 79:321-349.

Niswender CM, Herrick-Davis K, Dilley GE, Meltzer HY, Overholser JC, Stockmeier CA, Emeson RB, Sanders-Bush E (2001) RNA editing of the human serotonin 5-HT2C receptor. alterations in suicide and implications for serotonergic pharmacotherapy. Neuropsychopharmacology 24:478-491.

O'Connell MA, Krause S, Higuchi M, Hsuan JJ, Totty NF, Jenny A, Keller W (1995) Cloning of cDNAs encoding mammalian double-stranded RNA-specific adenosine deaminase. Mol Cell Biol 15:1389-1397.

Obermair GJ, Szabo Z, Bourinet E, Flucher BE (2004) Differential targeting of the L-type Ca2+ channel alpha 1C (CaV1.2) to synaptic and extrasynaptic compartments in hippocampal neurons. Eur J Neurosci 19:2109-2122.

Olson PA, Tkatch T, Hernandez-Lopez S, Ulrich S, Ilijic E, Mugnaini E, Zhang H, Bezprozvanny I, Surmeier DJ (2005) G-protein-coupled receptor modulation of striatal CaV1.3 L-type Ca2+ channels is dependent on a Shank-binding domain. J Neurosci 25:1050-1062.

Patil PG, Brody DL, Yue DT (1998) Preferential closed-state inactivation of neuronal calcium channels. Neuron 20:1027-1038.

Paupard MC, O'Connell MA, Gerber AP, Zukin RS (2000) Patterns of developmental expression of the RNA editing enzyme rADAR2. Neuroscience 95:869-879.

Paz N, Levanon EY, Amariglio N, Heimberger AB, Ram Z, Constantini S, Barbash ZS, Adamsky K, Safran M, Hirschberg A, Krupsky M, Ben-Dov I, Cazacu S, Mikkelsen T, Brodie C, Eisenberg E, Rechavi G (2007) Altered adenosine-to-inosine RNA editing in human cancer. Genome Res 17:1586-1595.

Pennartz CM, de Jeu MT, Bos NP, Schaap J, Geurtsen AM (2002) Diurnal modulation of pacemaker potentials and calcium current in the mammalian circadian clock. Nature 416:286-290.

Peterson BZ, DeMaria CD, Adelman JP, Yue DT (1999) Calmodulin is the Ca2+ sensor for Ca2+ -dependent inactivation of L-type calcium channels. Neuron 22:549-558.

Platzer J, Engel J, Schrott-Fischer A, Stephan K, Bova S, Chen H, Zheng H, Striessnig J (2000) Congenital deafness and sinoatrial node dysfunction in mice lacking class D L-type Ca2+ channels. Cell 102:89-97.

Raitskin O, Cho DS, Sperling J, Nishikura K, Sperling R (2001) RNA editing activity is associated with splicing factors in lnRNP particles: The nuclear pre-mRNA processing machinery. Proc Natl Acad Sci U S A 98:6571-6576.

Reyes JG (1996) Zinc transport in mammalian cells. Am J Physiol 270:C401-410.

Rueter SM, Dawson TR, Emeson RB (1999) Regulation of alternative splicing by RNA editing. Nature 399:75-80.

Rula EY, Lagrange AH, Jacobs MM, Hu N, Macdonald RL, Emeson RB (2008) Developmental modulation of GABA(A) receptor function by RNA editing. J Neurosci 28:6196-6201.

Safa P, Boulter J, Hales TG (2001) Functional properties of Cav1.3 (alpha1D) L-type Ca2+ channel splice variants expressed by rat brain and neuroendocrine GH3 cells. J Biol Chem 276:38727-38737.

Sansam CL, Wells KS, Emeson RB (2003) Modulation of RNA editing by functional nucleolar sequestration of ADAR2. Proc Natl Acad Sci U S A 100:14018-14023.

Schmauss C (2003) Serotonin 2C receptors: suicide, serotonin, and runaway RNA editing. Neuroscientist 9:237-242.

Seeburg PH, Hartner J (2003) Regulation of ion channel/neurotransmitter receptor function by RNA editing. Curr Opin Neurobiol 13:279-283.

Seeburg PH, Single F, Kuner T, Higuchi M, Sprengel R (2001) Genetic manipulation of key determinants of ion flow in glutamate receptor channels in the mouse. Brain Res 907:233-243.

Sharp PA, Burge CB (1997) Classification of introns: U2-type or U12-type. Cell 91:875-879.

Shen Y (2006) Investigation and Characterization of Splice Variation of L-type Ca^{2+} Channel, $Ca_V1.3$, in Chick Basilar Papilla and Rat Cochlear Hair Cells: Implications in Hearing. In: Department of Physiology, p 132. Singapore: National University of Singapore.

Shen Y, Yu D, Hiel H, Liao P, Yue DT, Fuchs PA, Soong TW (2006) Alternative splicing of the Ca(v)1.3 channel IQ domain, a molecular switch for Ca2+-dependent inactivation within auditory hair cells. J Neurosci 26:10690-10699.

Singh A, Hamedinger D, Hoda JC, Gebhart M, Koschak A, Romanin C, Striessnig J (2006) C-terminal modulator controls Ca2+-dependent gating of Ca(v)1.4 L-type Ca2+ channels. Nat Neurosci 9:1108-1116.

Singh A, Gebhart M, Fritsch R, Sinnegger-Brauns MJ, Poggiani C, Hoda JC, Engel J, Romanin C, Striessnig J, Koschak A (2008) Modulation of voltage- and Ca2+-dependent gating of CaV1.3 L-type calcium channels by alternative splicing of a C-terminal regulatory domain. J Biol Chem 283:20733-20744.

Sinnegger-Brauns MJ, Hetzenauer A, Huber IG, Renstrom E, Wietzorrek G, Berjukov S, Cavalli M, Walter D, Koschak A, Waldschutz R, Hering S, Bova S, Rorsman P, Pongs O, Singewald N, Striessnig JJ (2004) Isoform-specific regulation of mood behavior and pancreatic beta cell and cardiovascular function by L-type Ca 2+ channels. J Clin Invest 113:1430-1439.

Slavov D, Gardiner K (2002) Phylogenetic comparison of the pre-mRNA adenosine deaminase ADAR2 genes and transcripts: conservation and diversity in editing site sequence and alternative splicing patterns. Gene 299:83-94.

Slavov D, Clark M, Gardiner K (2000a) Comparative analysis of the RED1 and RED2 A-to-I RNA editing genes from mammals, pufferfish and zebrafish. Gene 250:41-51.

Slavov D, Crnogorac-Jurcevic T, Clark M, Gardiner K (2000b) Comparative analysis of the DRADA A-to-I RNA editing gene from mammals, pufferfish and zebrafish. Gene 250:53-60.

Sokolov S, Weiss RG, Timin EN, Hering S (2000) Modulation of slow inactivation in class A Ca2+ channels by beta-subunits. J Physiol 527 Pt 3:445-454.

Sommer B, Kohler M, Sprengel R, Seeburg PH (1991) RNA editing in brain controls a determinant of ion flow in glutamate-gated channels. Cell 67:11-19.

Song W, Liu Z, Tan J, Nomura Y, Dong K (2004) RNA editing generates tissue-specific sodium channels with distinct gating properties. J Biol Chem 279:32554-32561.

Soong TW, DeMaria CD, Alvania RS, Zweifel LS, Liang MC, Mittman S, Agnew WS, Yue DT (2002) Systematic identification of splice variants in human P/Q-type channel alpha1(2.1) subunits: implications for current density and Ca2+-dependent inactivation. J Neurosci 22:10142-10152.

Stefl R, Xu M, Skrisovska L, Emeson RB, Allain FH (2006) Structure and specific RNA binding of ADAR2 double-stranded RNA binding motifs. Structure 14:345-355.

Striessnig J (2007) C-terminal tailoring of L-type calcium channel function. J Physiol 585:643-644.

Tan G (2010) Characterization of Alternative Splicing of the Ca_V1.4 Calcium Channel Gene. In: Yong Loo Lin School of Medicine, Department of Physiology. Singapore: National University of Singapore.

Tang ZZ, Liang MC, Lu S, Yu D, Yu CY, Yue DT, Soong TW (2004) Transcript scanning reveals novel and extensive splice variations in human l-type voltage-gated calcium channel, Cav1.2 alpha1 subunit. J Biol Chem 279:44335-44343.

Tang ZZ, Liao P, Li G, Jiang FL, Yu D, Hong X, Yong TF, Tan G, Lu S, Wang J, Soong TW (2008) Differential splicing patterns of L-type calcium channel Cav1.2 subunit in hearts of Spontaneously Hypertensive Rats and Wistar Kyoto Rats. Biochim Biophys Acta 1783:118-130.

Taylor JT, Huang L, Keyser BM, Zhuang H, Clarkson CW, Li M (2005) Role of high-voltage-activated calcium channels in glucose-regulated beta-cell calcium homeostasis and insulin release. Am J Physiol Endocrinol Metab 289:E900-908.

Tsunemi T, Saegusa H, Ishikawa K, Nagayama S, Murakoshi T, Mizusawa H, Tanabe T (2002) Novel Cav2.1 splice variants isolated from Purkinje cells do not generate P-type Ca2+ current. J Biol Chem 277:7214-7221.

Valente L, Nishikura K (2007) RNA binding-independent dimerization of adenosine deaminases acting on RNA and dominant negative effects of nonfunctional subunits on dimer functions. J Biol Chem 282:16054-16061.

Vitali P, Basyuk E, Le Meur E, Bertrand E, Muscatelli F, Cavaille J, Huttenhofer A (2005) ADAR2-mediated editing of RNA substrates in the nucleolus is inhibited by C/D small nucleolar RNAs. J Cell Biol 169:745-753.

Wagner RW, Yoo C, Wrabetz L, Kamholz J, Buchhalter J, Hassan NF, Khalili K, Kim SU, Perussia B, McMorris FA, et al. (1990) Double-stranded RNA unwinding and modifying activity is detected ubiquitously in primary tissues and cell lines. Mol Cell Biol 10:5586-5590.

Wang Y, Deng X, Mancarella S, Hendron E, Eguchi S, Soboloff J, Tang XD, Gill DL (2010) The calcium store sensor, STIM1, reciprocally controls Orai and CaV1.2 channels. Science 330:105-109.

Wei X, Neely A, Lacerda AE, Olcese R, Stefani E, Perez-Reyes E, Birnbaumer L (1994) Modification of Ca2+ channel activity by deletions at the carboxyl terminus of the cardiac alpha 1 subunit. J Biol Chem 269:1635-1640.

Weick JP, Groth RD, Isaksen AL, Mermelstein PG (2003) Interactions with PDZ proteins are required for L-type calcium channels to activate cAMP response element-binding protein-dependent gene expression. J Neurosci 23:3446-3456.

Weisskopf MG, Bauer EP, LeDoux JE (1999) L-type voltage-gated calcium channels mediate NMDA-independent associative long-term potentiation at thalamic input synapses to the amygdala. J Neurosci 19:10512-10519.

Werry TD, Loiacono R, Sexton PM, Christopoulos A (2008) RNA editing of the serotonin 5HT2C receptor and its effects on cell signalling, pharmacology and brain function. Pharmacol Ther 119:7-23.

Westenbroek RE, Hoskins L, Catterall WA (1998) Localization of Ca2+ channel subtypes on rat spinal motor neurons, interneurons, and nerve terminals. J Neurosci 18:6319-6330.

Whitney NP, Peng H, Erdmann NB, Tian C, Monaghan DT, Zheng JC (2008) Calcium-permeable AMPA receptors containing Q/R-unedited GluR2 direct human neural progenitor cell differentiation to neurons. FASEB J 22:2888-2900.

Wiser O, Trus M, Hernandez A, Renstrom E, Barg S, Rorsman P, Atlas D (1999) The voltage sensitive Lc-type Ca2+ channel is functionally coupled to the exocytotic machinery. Proc Natl Acad Sci U S A 96:248-253.

Wong SK, Sato S, Lazinski DW (2001) Substrate recognition by ADAR1 and ADAR2. RNA 7:846-858.

Xu M, Welling A, Paparisto S, Hofmann F, Klugbauer N (2003) Enhanced expression of L-type Cav1.3 calcium channels in murine embryonic hearts from Cav1.2-deficient mice. J Biol Chem 278:40837-40841.

Xu W, Lipscombe D (2001) Neuronal Ca(V)1.3alpha(1) L-type channels activate at relatively hyperpolarized membrane potentials and are incompletely inhibited by dihydropyridines. J Neurosci 21:5944-5951.

Yang PS, Alseikhan BA, Hiel H, Grant L, Mori MX, Yang W, Fuchs PA, Yue DT (2006) Switching of Ca2+-dependent inactivation of Ca(v)1.3 channels by calcium binding proteins of auditory hair cells. J Neurosci 26:10677-10689.

Zhang H, Fu Y, Altier C, Platzer J, Surmeier DJ, Bezprozvanny I (2006) Ca1.2 and CaV1.3 neuronal L-type calcium channels: differential targeting and signaling to pCREB. Eur J Neurosci 23:2297-2310.

Zhang H, Maximov A, Fu Y, Xu F, Tang TS, Tkatch T, Surmeier DJ, Bezprozvanny I (2005) Association of CaV1.3 L-type calcium channels with Shank. J Neurosci 25:1037-1049.

Zhang Z, Xu Y, Song H, Rodriguez J, Tuteja D, Namkung Y, Shin HS, Chiamvimonvat N (2002) Functional Roles of Ca(v)1.3 (alpha(1D)) calcium channel in sinoatrial nodes: insight gained using gene-targeted null mutant mice. Circ Res 90:981-987.